This is to certify that the

thesis entitled

The Characterization of Thermal Fatigue Effects by the Observation of Growth of Indentation Cracks in Unreinforced Polycrystalline Al_2O_3

presented by

Won-Sik Kim

has been accepted towards fulfillment of the requirements for

Master's degree in Materials Science

Eldon D. Case

Major professor

Date 9/11/95

THE CHARACTERIZATION OF THERMAL FATIGUE EFFECTS BY THE OBSERVATION OF GROWTH OF INDENTATION CRACKS IN UNREINFORCED POLYCRYSTALLINE Al_2O_3

By

Won-Sik Kim

A THESIS

Submitted to
Michigan State University
in partial fulfillment of the requirements
for the degree of

MASTER OF SCIENCE

Department of Materials Science and Mechanics

August 1995

ABSTRACT

THE CHARACTERIZATION OF THERMAL FATIGUE EFFECTS BY THE OBSERVATION OF GROWTH OF INDENTATION CRACKS IN UNREINFORCED POLYCRYSTALLINE Al_2O_3

By

Won-Sik Kim

In this study, we characterized the thermal fatigue damage for unreinforced polycrystalline alumina specimens by measuring the cyclic thermal shock induced growth of Vickers indentation cracks placed in the specimens prior to thermal shock. The severity of thermal shock damage increased with increasing quench temperature difference.

A minor amount of crack growth occurred after the introduction of the Vickers indentation cracks prior to commencing the thermal fatigue testing. The crack initially grew an average of 4.3 percent but crack growth saturated within 30 minutes.

Grain bridging during thermal fatigue was investigated using a scanning electron microscope (SEM). Although grain bridging is an often-cited mechanism for energy dissipation for cracks growing in unreinforced alumina, grain bridging was infrequent in the specimens included in this study. Thus grain bridging may not account for the saturation in the thermal fatigue crack length observation in this study.

Acknowledgment

I would like to thank my adviser, Dr. Eldon case for his advice and editing this thesis throughout my study. I also thank my fellow researchers Brett Wilson, Kiyong Lee, and Changlin Liu for their help during the my research.

I would also thank my parents for their support during my study. I would like express my special thanks to my wife, Jeongjoo Moon for her help and patience.

Table of Contents

List of Tables

List of Figures

1. Introduction

When brittle materials are heated or cooled rapidly, they are subjected to thermal shock which can lead to microcracking or catastrophic failure [1-6]. In addition, many engineering applications should be considered thermal shock effect if they are under the condition that the ambient temperature differences are large. Thermal shock tests as be classified as either single quench thermal shock tests [7-9] or cyclic thermal shock tests [10-13]. The single quench thermal shock tests involve heating the specimen and quenching the specimen into water [5,6], oil [14], or air [3,15]. The retained strength is measured typically by a 3 or 4 point bend test. The other is cyclic thermal shock test.

Single quench tests are unsatisfactory for applications such as ceramic turbine, computer main frame memory [16], or solar system collector where the materials are periodically heated and cooled.

Thermal shock damages can be monitored in variety of methods. Retained strength measurements are often used [6-7], but the retained strengths fluctuate depending on the geometry of specimen. Non-destructive measurements, such as elastic modulus and internal friction, can be used to monitor the evolution of thermal shock damage in a given specimen [10-13].

In this study, Vickers indentation cracks were induced in unreinforced polycrystalline alumina specimens. The crack length was measured during thermal fatigue (cyclic thermal shock).

1.1. Thermal shock resistance parameter

Thermal shock resistance parameters indicate properties critical to thermal shock damage. These parameters are approximately quantitative measurements of thermal shock resistance.

1.1.1. Thermal shock resistance without crack initiation

When ceramic materials are heated or cooled rapidly, a temperature gradient appears through the specimen thickness (Figure 1.1.1)

In general, the thermal stress, σ_{th} caused by the difference of the ambient temperature is given as follows for an infinite slab [17,18].

$$\sigma_{th} = \frac{E\alpha}{1-\nu}\Delta T \tag{1.1.1}$$

where σ_{th} = thermal stress

ν = Poisson's ratio

α = thermal expansion coefficient

ΔT = temperature difference between furnace and water bath.

When fracture occurs, $\Delta T = \Delta T_{crit}$ and $\sigma_{th} = \sigma_{crit}$ such that [17,18]

$$\Delta T_{crit} = \frac{\sigma_{crit}(1-\nu)}{E\alpha} \tag{1.1.2}$$

where ΔT_{crit} = critical temperature difference

σ_{crit} = fracture strength.

From Equation 1.1.1, thermal shock resistance parameter, R, is defined as [17,18]

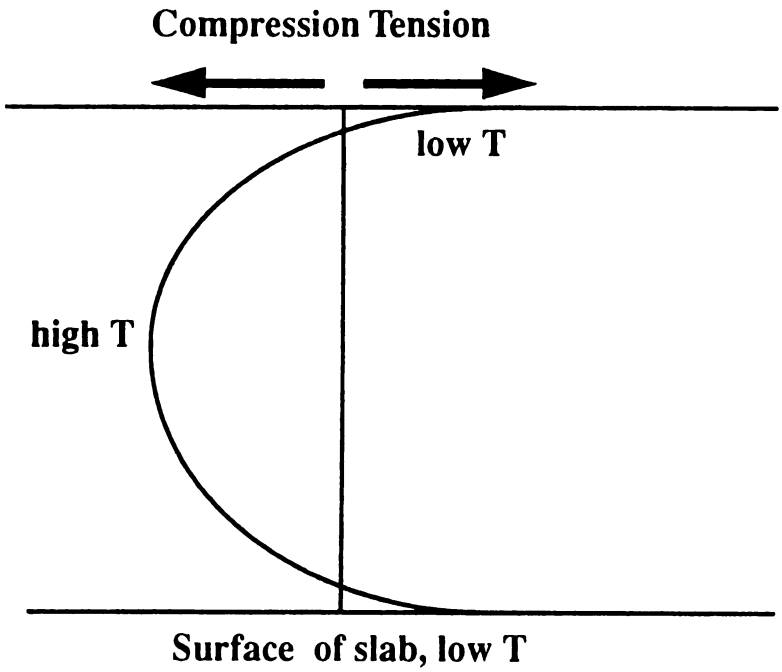

Figure 1.1.1. Temperature and stress distribution for a plate cooled from the surface when specimen is heated and quenched [18,19].

$$R = \frac{\sigma_{crit}(1-\nu)}{E\alpha} \quad \text{or} \quad R' = \frac{k\sigma_{crit}(1-\nu)}{E\alpha} \tag{1.1.3}$$

where k = thermal conductivity.

High R and R' values favor avoidance of crack initiation. Therefore, for high R and R' values, the strength and thermal conductivity of materials should be high while thermal expansion coefficient, Poisson's ratio and Young's modulus should be low.

1.1.2. Thermal shock resistance related to surface flaws

Compressibility, β, is the fractional volume change per unit of pressure and is defined as

$$\beta = \frac{3(1-2\nu)}{E}. \tag{1.2.1}$$

where ν = Poisson's ratio

E = Young's modulus

The volume changes can be expressed in terms of compressibility [19]

$$d(V_0 - V_p) = \beta V_0 dp \tag{1.2.2}$$

where V_0 = volume of body

V_p = volume of porosity

p = external pressure.

Equation 1.2.2 can be rearranged to yield

$$\beta = \frac{d(V_0 - V_p)}{V_0 dp} \tag{1.2.3}$$

and

$$\frac{1}{V_0}\frac{dV_0}{dp} = \beta + \frac{1}{V_0}\frac{dV_p}{dp} . \tag{1.2.4}$$

If the left side of equation 1.2.4 is the actual compressibility, β_a for a porous elastic material, then equation 1.2.4 is

$$\beta_a = \beta + \frac{pdV_p}{V_0 pdp} . \tag{1.2.5}$$

Walsh gave the strain energy for N small penny shaped cracks with half length, c [19] as

$$dW = \beta \sum_N \frac{16(1-\nu^2)}{9(1-2\nu)} c^3 pdp . \tag{1.2.6}$$

From equation 1.2.6, equation 1.2.7 can be obtained.

$$pdV_p = dw = \beta \frac{16(1-\nu^2)Nc^3}{9(1-2\nu)} pdp \tag{1.2.7}$$

where N = number of crack.

If equation 1.2.1 and 1.2.7 are inserted into equation 1.2.5, we can obtain equation 1.2.8 since pdV_p is work related to crack formation which is identical to an increase in the strain energy [19].

$$\beta_a = \beta\{1 + \frac{16(1-\nu^2)Nc^3}{9(1-2\nu)V_0}\} = \frac{3(1-2\nu)}{E_0}\{1 + \frac{16(1-\nu^2)Nc^3}{9(1-2\nu)V_0}\} \tag{1.2.8}.$$

where E_0 is Young's modulus of the crack-free material and β_a is as defined for equation 1.2.4. The total energy per unit volume is the sum of elastic energy, $\frac{1}{2}E(\alpha\Delta T)^2$, and the fracture energy of the cracks, $2N\pi c^2\Gamma$ (the factor of 2 indicates two fracture surface) where Γ is defined surface energy if the crack shapes are circular [19]

$$W_t = \frac{1}{2}E(\alpha\Delta T)^2 + 2\pi Nc^2\Gamma = \frac{3(\alpha\Delta T)^2 E_0}{2(1-2\nu)}[1+\frac{16(1-\nu^2)Nc^3}{9(1-2\nu)}]^{-1} + 2\pi Nc^2\Gamma \quad (1.2.9)$$

where Γ is fracture surface energy and N is the number of cracks. If we set $\frac{dW_t}{dc} = 0$, then using equation 1.2.9 we can obtain

$$-\frac{3(\alpha\Delta T)^2 E_0}{2(1-2\nu)}[1+\frac{16(1-\nu^2)Nc^3}{9(1-2\nu)}]^{-2}[\frac{16(1-\nu^2)Nc^2}{3(1-2\nu)}] + 4\pi Nc\Gamma = 0$$

$$\frac{3(\alpha\Delta T)^2 E_0}{2(1-2\nu)}[1+\frac{16(1-\nu^2)Nc^3}{9(1-2\nu)}]^{-2}[\frac{16(1-\nu^2)Nc^2}{3(1-2\nu)}] = 4\pi Nc\Gamma. \quad (1.2.10)$$

Rearranging equation 1.2.10 gives

$$(\alpha\Delta T)^2 = 4\pi Nc\Gamma\frac{2(1-2\nu)}{3E_0}[1+\frac{16(1-\nu^2)Nc^3}{9(1-2\nu)}]^2[\frac{16(1-\nu^2)Nc^2}{3(1-2\nu)}]^{-1}. \quad (1.2.11)$$

Equation 1.2.11 can be expressed by ΔT as following

$$\Delta T = [\frac{\pi\Gamma(1-2\nu)^2}{2E_0\alpha^2(1-\nu)^2}]^{\frac{1}{2}}[1+\frac{16(1-\nu^2)Nc^3}{9(1-2\nu)}]c^{-\frac{1}{2}}. \quad (1.2.12)$$

Equation 1.2.12 suggests a critical temperature when $\frac{dW_t}{dc} = 0$, thus critical temperature above which crack instability occurs is [7]

$$\Delta T_c = [\frac{\pi\Gamma(1-2\nu)^2}{2E_0\alpha^2(1-\nu)^2}]^{\frac{1}{2}}[1+\frac{16(1-\nu^2)Nc^3}{9(1-2\nu)}]c^{-\frac{1}{2}}. \quad (1.2.13.a)$$

The excess energy from the difference between the elastic energy release and surface the fracture energy is transferred into kinetic energy of crack growth such that the released energy equals to the surface fracture then the crack propagation terminated when energy is balanced;

release of elastic energy = increase in surface fracture energy

thus

initial elastic energy - final elastic energy = final surface energy - initial surface energy.

From equation 1.2.9, we can obtain the following equation 1.2.14 [7] for final (critical) crack length

$$\frac{3(\alpha\Delta T)^2 E_0}{2(1-\nu)}[\{1+\frac{16(1-\nu^2)Nc_0{}^3}{9(1-2\nu)}\}^{-1}-\{1+\frac{16(1-\nu^2)Nc_f{}^3}{9(1-2\nu)}\}^{-1}]=2\pi N\Gamma(c_f{}^2-c_0{}^2) \quad (1.2.14)$$

where c_0 = initial crack length

c_f = final crack length or critical crack length.

If the initial crack length(c_0) is much smaller than final crack length(c_f), then the terms $\frac{16(1-\nu^2)Nc_0{}^3}{9(1-2\nu)}$ and $\{1+\frac{16(1-\nu^2)Nc_f{}^3}{9(1-2\nu)}\}^{-1}$(since $c_f{}^3$ is very large) in equation 1.2.14 are very small, thus equation 1.2.14 can be simplified such that

$$\frac{3(\alpha\Delta T)^2 E_0}{2(1-\nu)} = 2\pi N\Gamma\, c_f{}^2. \quad (1.2.15)$$

If crack length is short in equation 1.2.13, second term of $[\,1+\frac{16(1-\nu^2)Nc^3}{9(1-2\nu)}]$ can be ignored, then ΔT becomes

$$\Delta T=[\frac{\pi\Gamma(1-2\nu)^2}{2E_0\alpha^2(1-\nu^2)}]^{\frac{1}{2}}[c]^{-\frac{1}{2}}. \quad (1.2.13.b)$$

If ΔT from equation 1.2.13.b is inserted into equation 1.2.15, the critical crack length c_f becomes [7]

$$c_f=\{\frac{3(1-2\nu)^2}{8\pi(1-\nu^2)c_0N}\}^{\frac{1}{2}}. \quad (1.2.16)$$

Equation 1.2.16 suggests that the critical crack length is a function of initial crack length and a weak function of Poisson's ratio. Other material properties rarely affect critical crack length. Sack [20] assumed that circular cracks were introduced into a crack-free material and calculated the change of free energy. When a uniform stress is applied normal to a brittle material containing circular cracks and if the cracks are much smaller than the whole body of brittle materials, Sack [20] gave elastic energy of the brittle body as

$$G_e = -\frac{8(1-\nu^2)}{3E}\sigma^2 c^3. \tag{1.2.17}$$

In addition, the crack surface energy is $2\pi c^2\Gamma$ thus the total energy change induced by the crack is given as

$$G = 2\pi c^2\Gamma - \frac{8(1-\nu^2)}{3E}\sigma^2 c^3. \tag{1.2.18}$$

From equation 1.2.18, a critical (maximum) crack length can be obtained when dG/dc = 0

$$4\pi c\Gamma - \frac{8(1-\nu^2)}{E}\sigma^2 c^2 = 0. \tag{1.2.19}$$

Equation 1.2.19 can be expressed in terms of crack length, c

$$c = \frac{\pi E\Gamma}{2\sigma^2(1-\nu^2)}. \tag{1.2.20.a}$$

If $\sigma = \sigma_f$, where σ_f is fracture stress, then equation 1.2.20 becomes

$$c = \frac{\pi E\Gamma}{2\sigma_f{}^2(1-\nu^2)}. \tag{1.2.20.b}$$

Equation 1.2.20 can be expressed in terms of fracture stress,

$$\sigma_f = \{\frac{\Gamma E}{2c(1-\nu^2)}\}^{\frac{1}{2}}. \tag{1.2.21.a}$$

If we apply equation 1.2.21 to the initial flaw population, then E = E_0 and c = c_0, σ_f [7,20] is given by

$$\sigma_f = \{\frac{\Gamma E_0}{2c_0(1-\nu^2)}\}^{\frac{1}{2}}. \qquad (1.2.21.b)$$

When equation 1.2.16 is divided by equation 1.2.21.b, the initial crack length, c_0 can be removed, then the relationship between critical crack length and fracture strength is [7]

$$c_f = \{\frac{3(1-\nu)\sigma_f^{\,2}}{4\pi N\Gamma E_0}\}^{\frac{1}{2}}. \qquad (1.2.22)$$

If the cracks are circular as was assumed by equation 1.2.22, then the crack growth resistance, R"" is expressed as equation 1.2.21 [7,16] since crack length is proportional to the inverse of $\frac{\sigma_f^{\,2}(1-\nu)}{\Gamma E}$.

$$R'''' = \frac{\Gamma E}{\sigma_f^{\,2}(1-\nu)}. \qquad (1.2.21)$$

To avoid catastrophic crack propagation, R"" should be large. Thus the surface energy and the Young's modulus should be high and the fracture strength should be low.

1.2 Comparing the strength degradation behavior as temperature difference increases: Hassleman plot and statistical method

1.2.1. Strength degradation behavior: the Hasselman plot

Many researchers have evaluated thermal shock damage in terms of retained strength as a function of quenching temperature difference. The typical retained strength analysis is represented by the Hasselman plot which is a schematic diagram of retained strength and temperature difference that shows there are 3 temperature regions (Figure 1.2.1).

At low quenching temperature differences, there is no change in retained strength. No crack propagation occurs since the thermal stress is not high enough for cracks to grow. To initiate cracks a specific quenching temperature difference is required. The second region is related to the initiation of crack propagation. If cracks propagate, there are two kinds of behavior : (a) a catastrophic decrease in retained strength and (b) a steady decrease of retained strength. Hassleman explained the catastrophic decrease in retained strength in terms of kinetic crack propagation [7]. The steady decrease of retained strength is caused by quasi-static propagation [7]. The catastrophic decrease of retained strength tends to occur in high strength ceramic materials which have the high elastic strain energy and the low resistance to crack growth.

Gupta [21] investigated strength degradation through thermal quenching. Water was used as a quenching medium. Gupta [21] observed kinetic crack propagation behavior for both single crystal alumina and polycrystalline alumina specimens with mean grain size of 10, 34, and 40 μm while a gradual decrease in strength also was observed for the

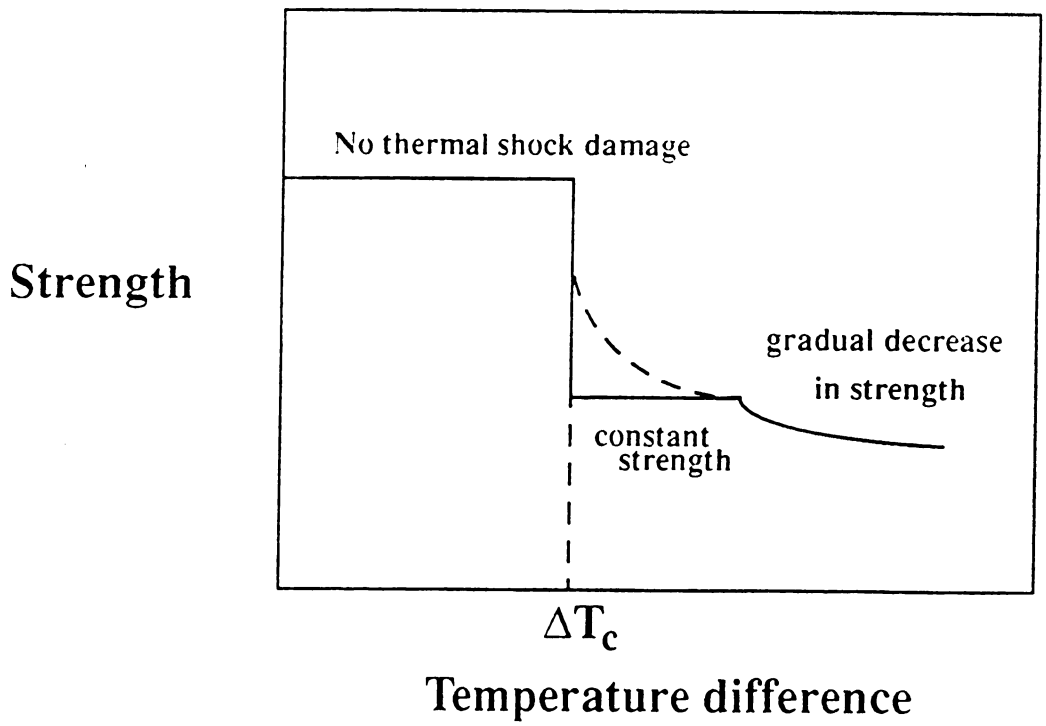

Figure 1.2.1. The Hassleman plot which is a schematic of temperature difference behavior for a ceramic materials [7,21].

larger grain sized (84 μm) alumina specimen. In catastrophic decrease of strength (for 10, 34, and 40 μm grain sized specimens), the critical temperature differences (ΔT_c) were about 190 °C. No change in strength was observed at the interval from ΔT = 190 °C to ΔT = 280 °C, then a gradual decrease in strength was followed. Hasselman found that the strength decreased gradually as the quench temperature differences increased (without a sudden drop of strength) for low strength materials such as insulating firebrick [7].

The third region corresponds to quasi-static crack propagation. The retained strength decreases monotonically as temperature difference increases. Bradt *et al.* [9] contended that an increase of strength following quenching or thermal tempering follows the second region. Bradt *et al.* observed an increase of strength following an interval of quench temperature difference in which strength is constant. For example, a commercial aluminosilicate quenched into silicone oil [8] showed an interval of constant strength followed by a drop of in strength (Figure 1.2.2). However, for quench temperature differences between 1100 °C and 1400 °C, the residual strength of the aluminosilicate increased (Figure 1.2.2).

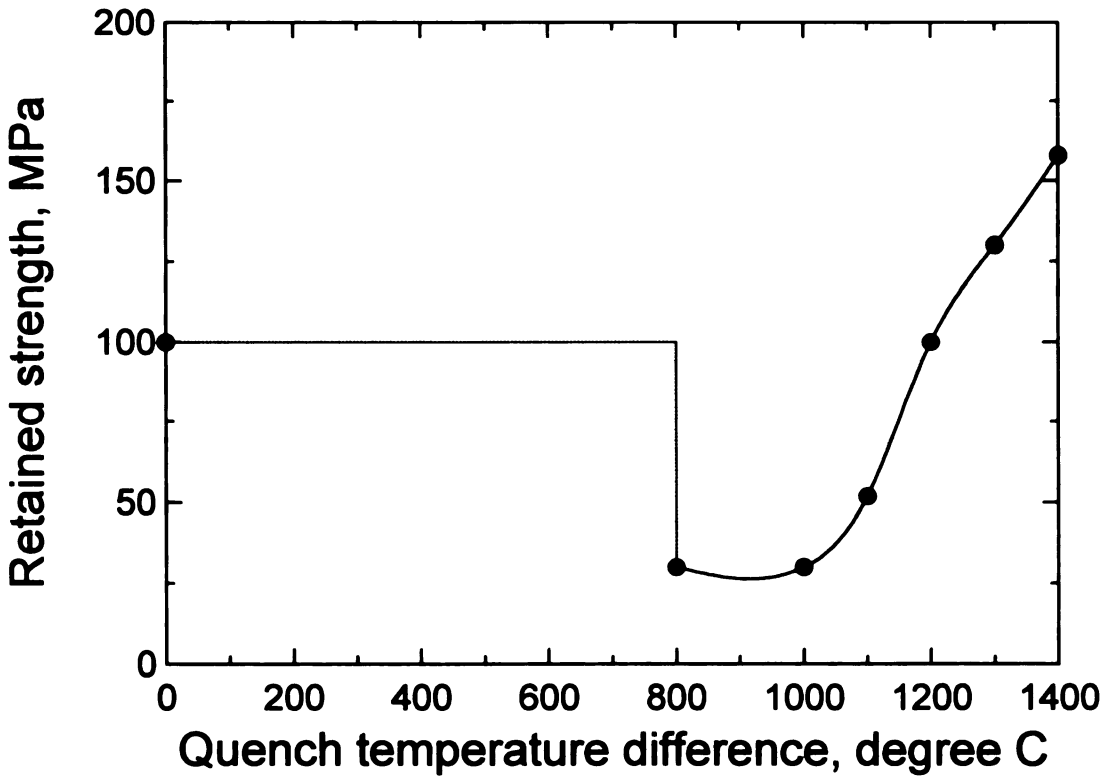

Figure 1.2.2. A plot of the mean retained strength versus quench temperature difference for aluminosilicate after thermal shock [8].

1.2.2. Strength degradation behavior as temperature difference increases : statistical method

The statistical approach to thermal shock damage investigates the retained strength of an entire population of thermally shocked specimens. As an example, Bradt *et al.* studied a set of 50 alumina specimens [22], a set of 25 aluminosilicate specimens [8] and a set of 50 borosilicates glass specimens [22,23]. All specimen strengths before and after thermal shock were measured and the strength distribution was investigated.

Ashizuka *et al.* [23] measured the strength of borosilicate glass after a thermal shock into room temperature water or into 77 K liquid nitrogen. The strengths ranged from 3 to 115 MPa at a temperature difference of 500 °C, 10 to 112 MPa at a temperature difference of 400 °C, and 15 to 110 MPa at a temperature difference of 300 °C in the water bath while the average strength before thermal shock was about 115 MPa. Strength distribution indicated that initially low strength specimens tend to fracture at low stresses. A rapid decrease in strength after thermal shock did not occur at a specific quench temperature difference. In addition, high strength specimens were not damaged while low strength specimen were severely affected by thermal shock. The average strengths are indicative of a quasi-static crack propagation or steady decrease in retained strength rather than a kinetic crack propagation which can result in a rapid dramatic decrease in retained strength (Figure 1.2.3-4).

Brat *et al.*[9] suggest that a specific quench temperature difference may occur for small specimens size. The specimens' strength distribution indicated that a specific thermal stress initiated thermal shock damage for each specimen. Bradt *et al.* [9,23] explained there are two types of flaws after thermal shocking for each specimen. One

flaw type is the pre-existent flaw population which existed prior to thermal shock. The other flaw type is induced by the thermal quenching. Thermal shock damage changes the flaw population and the crack arrest behavior occurs.

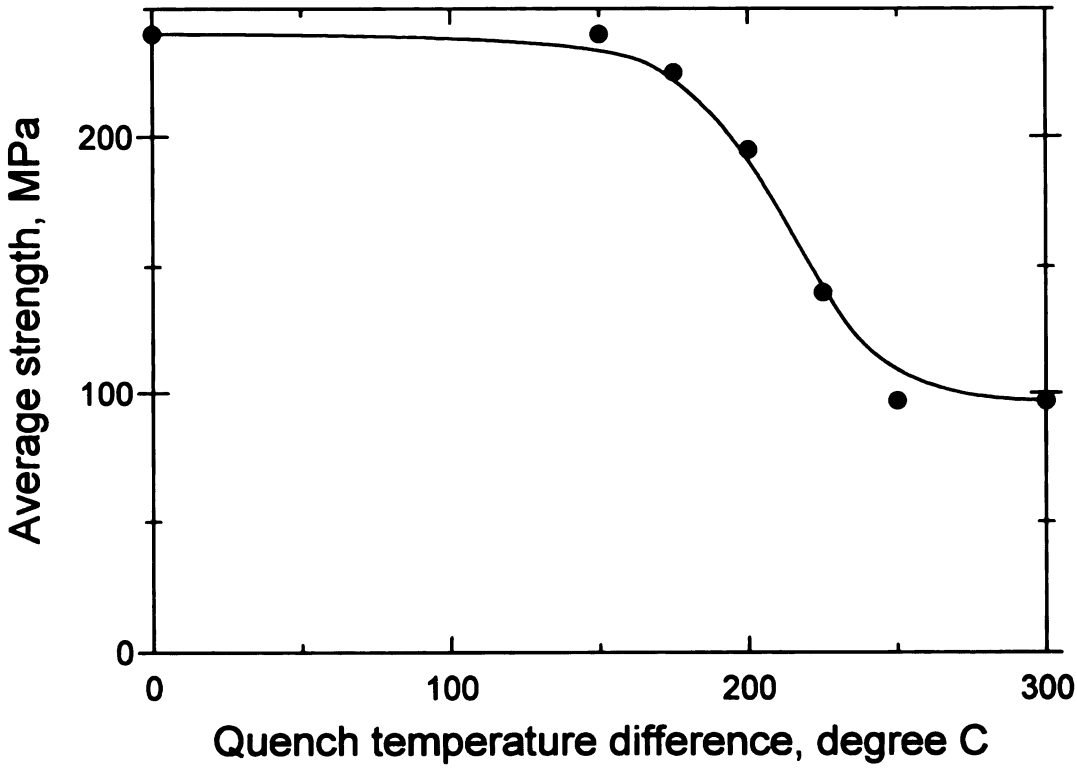

Figure 1.2.3. The average retained strength after thermal shock for cylindrical polycrystalline 86% alumina specimen. The quenching medium is room temperature water [22].

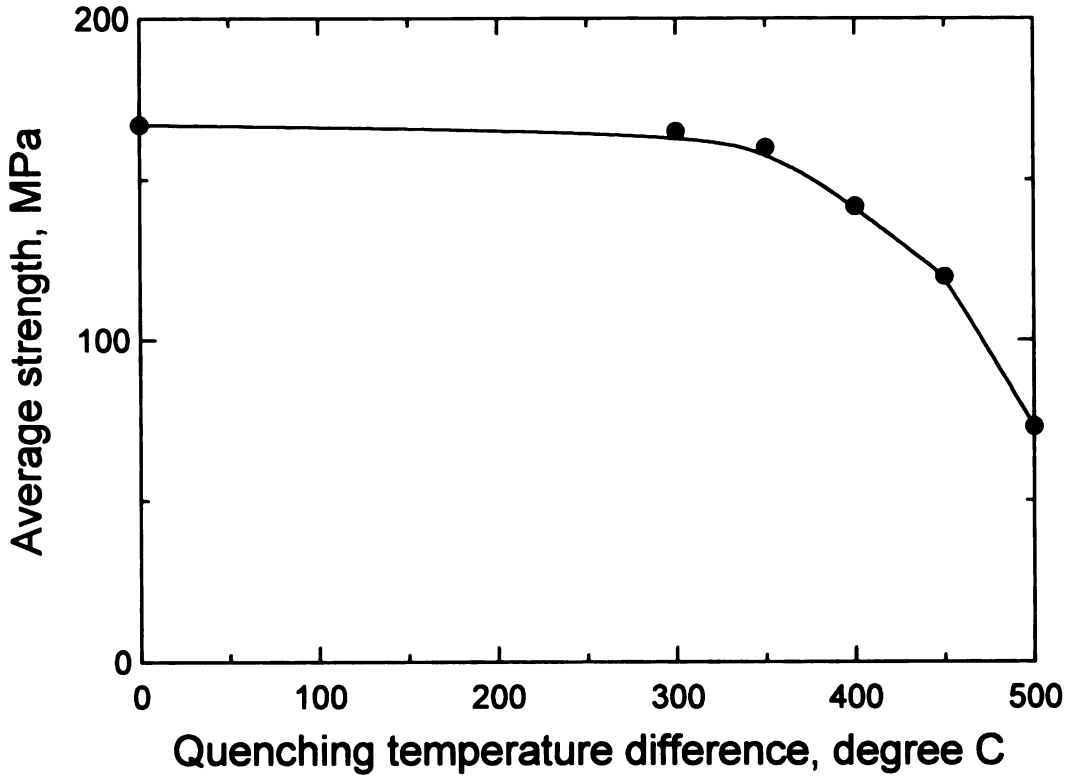

Figure 1.2.4. The average retained strength after thermal shock for borosilicate glass specimen. The quenching medium is liquid nitrogen [23].

1.3. Cyclic thermal shock effects

Most experiments involving thermal-stress-induced damage utilize single quench-thermal shock testing [21-25]. However, many ceramic applications are actually involved in repeated cycling in the ambient temperature difference (thermal fatigue) as is the case for mainframe computer memories and solar cells. Thermal fatigue damage is caused by the accumulation of repeated temperature difference (thermal loading). Thus one should consider thermal fatigue damage in designing ceramics for a variety of applications.

Cyclic thermal shock tests have been performed with various materials with differing properties. Herakovich [26] observed the cyclic thermal shock damage in the air for graphite epoxy by measuring crack number density (number of cracks/length). Herakovich [26] thermally fatigued the graphite epoxy specimens using a temperature difference about 278 °C in an environmental chamber. Figure 1.3.1 shows crack density increases as the thermal cycling increases indicating thermal shock damage (crack number density) is a function of cumulative number of thermal cycles.

Ainsworth *et al.* [27] performed cyclic thermal shock testing on MgO, Al_2O_3, and MgO-Cr_2O_3 refractories with air as the quenching medium. Specimens were placed in a 1204 °C preheated furnace for 10 minutes and then the specimens were cooled in air. Ainsworth *et al.* [27] evaluated the thermal shock damage by measuring modulus of rupture. The strengths decreased as quenching temperature increased (Figure 1.3.2). Thermal shock damage saturation behavior also is observed in Figure 1.3.2 that is, the

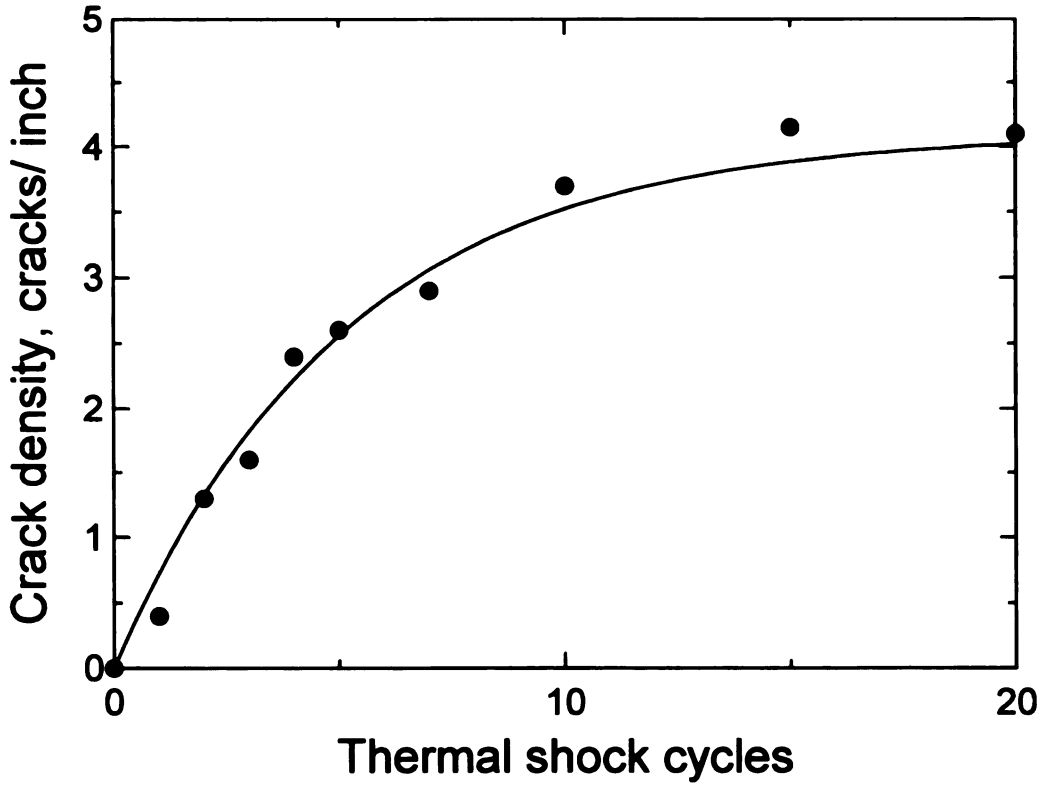

Figure 1.3.1. The crack number density as the function of cumulative thermal fatigue cycles for graphite epoxy specimens[10,25]. The solid line was obtained by least-squares fit to equation 1.3.1 [10].

property (strength in Figure 1.3.2) reaches a steady state value, which indicates a saturation of microcrack damage.

Semler *et al.* [28] observed thermal fatigue in high alumina refractories by measuring strength (modulus of rupture) and Young's modulus. Specimens were heated in air to 1000 °C (as measured by a thermocouple) by burner flame and then the specimens were cooled in air to 150-200 °C. After 5 thermal shock cycles, a strength decrease of 30-35 percent of strength decrease was observed. Semler *et al.* also evaluated degradation of Young's modulus for high alumina refractory, in which thermal shock damage increased as the cumulative number of thermal cycles increased (Figure 1.3.3). A saturation of modulus also was observed for the refractories [28].

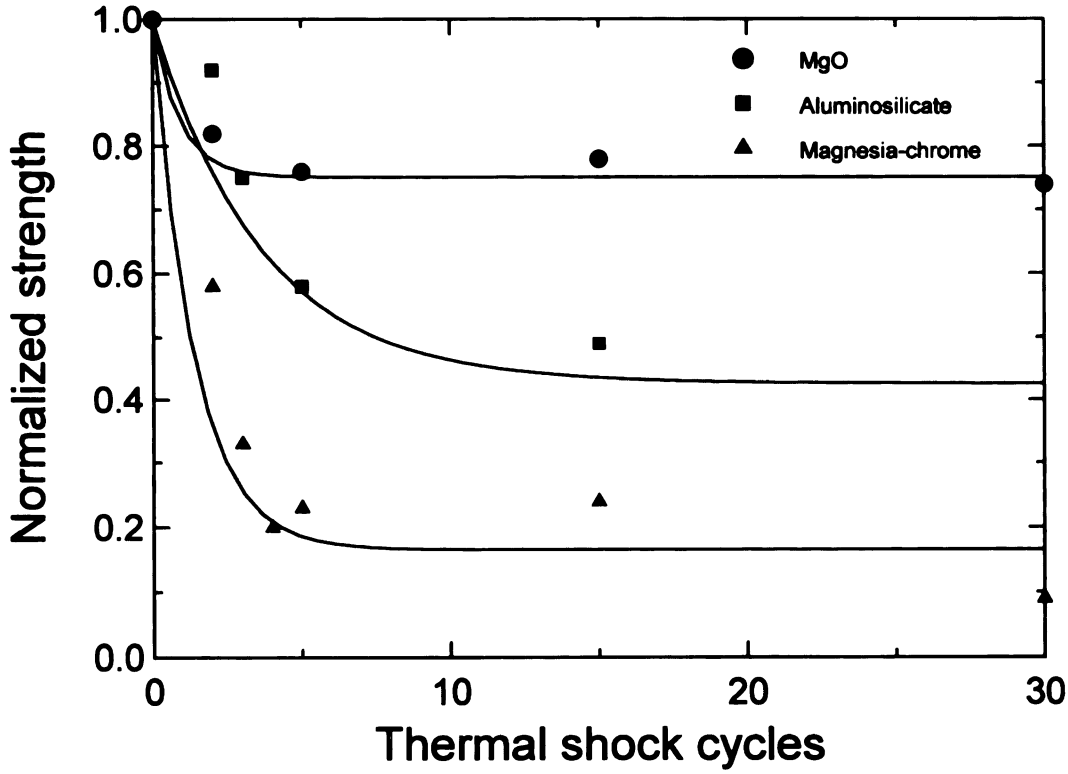

Figure 1.3.2. Thermal shock damage in terms of modulus of rupture versus the cumulative number of thermal fatigue cycles for MgO, Al_2O_3, and MgO-Cr_2O_3 refractory [10,27] at temperature difference 1180 °C in the air. The solid line was obtained by least-squares fit to equation 1.3.1 [10].

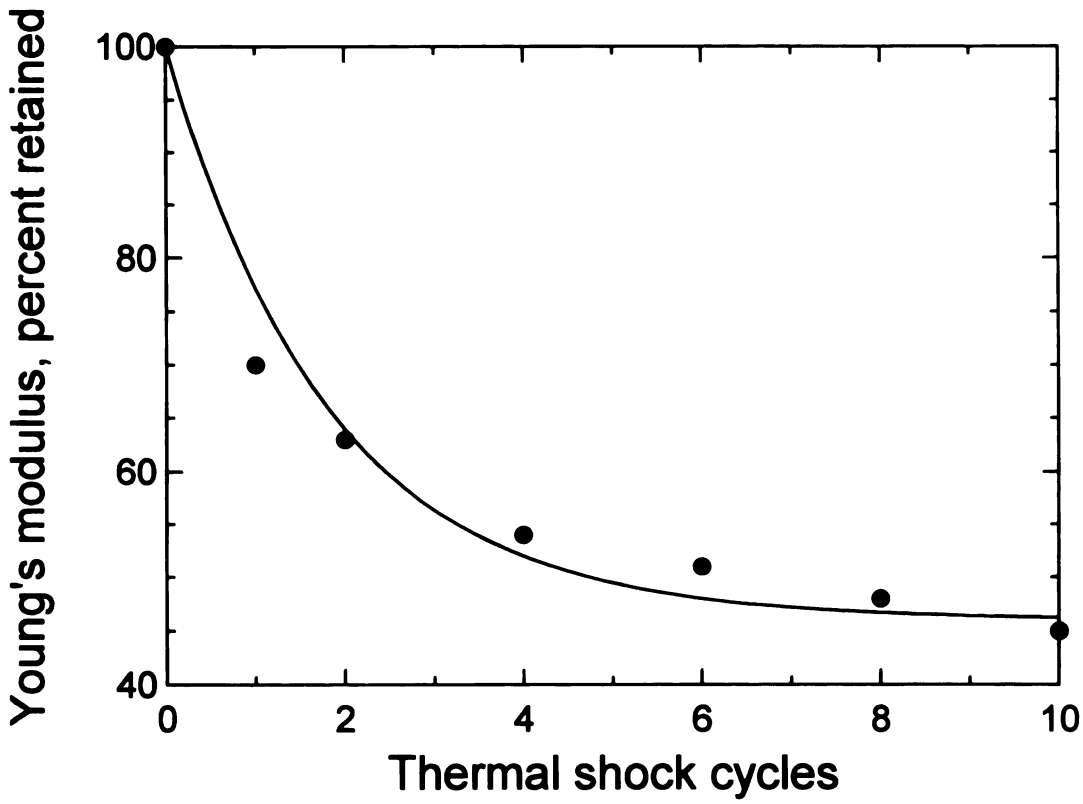

Figure 1.3.3. The Young's modulus observed for 60% alumina refractory by quenched in air [10,28]. The solid line was obtained by least-squares fit to equation 1.3.1 [10].

Case *et al.* [10-12, 29-31] investigated thermal fatigue effects for ceramics and ceramic composites. Thermal shock damage was evaluated nondestructively by measuring elastic modulus and internal friction. In Case *et al.*'s study of thermal fatigue, water [11-12, 29-30], silicon oil [13,30] and liquid nitrogen [13,30] were used as quenching media. In this thesis, we shall compare the crack length measurements done for a water quenching medium (this study) to elastic modulus and internal friction measurements done by Case *et al.* [10-12, 29-30]. Case *et al.* also observed that as the quenching temperature difference increases, the severity of the thermal shock damage also increases (Figure 1.3.4). In addition, thermal shock damage tended to saturate after a few cumulative cycles [10-12, 29-30]. Figure 1.3.4 shows the Young modulus saturation during thermal fatigue testing as the thermal shock cycles increases. Case *et al.* obtained empirical equation 1.3.1 [10-12, 29-30] from the thermal fatigue data.

$$E = E_0 - a\{1 - \exp(-bN)\} \tag{1.3.1}$$

where E= Young's modulus

E_0 = Young's modulus of undamaged specimen

a = the thermal shock damage constant

b = rate constant

N = the number of thermal shock cycles

The solid curves in Figure 1.3.4 represent a least-squares fit of the thermal fatigue data to equation 1.3.1 for unreinforced polycrystalline alumina specimens quenched into a room temperature deionized water bath [12].

The typical schematic diagram of thermal shock damage saturation (Figure 1.3.5) may be described in terms of a generalized form of equation 1.3.1, namely

$$\Omega = \Omega_0 - A\{1 - \exp(-\alpha N)\} \tag{1.3.2}$$

where Ω = a material property of specimen

Ω_0 = a material property of specimen of undamaged specimen

A = the thermal shock damage constant

α = rate constant

N = the number of thermal shock cycles.

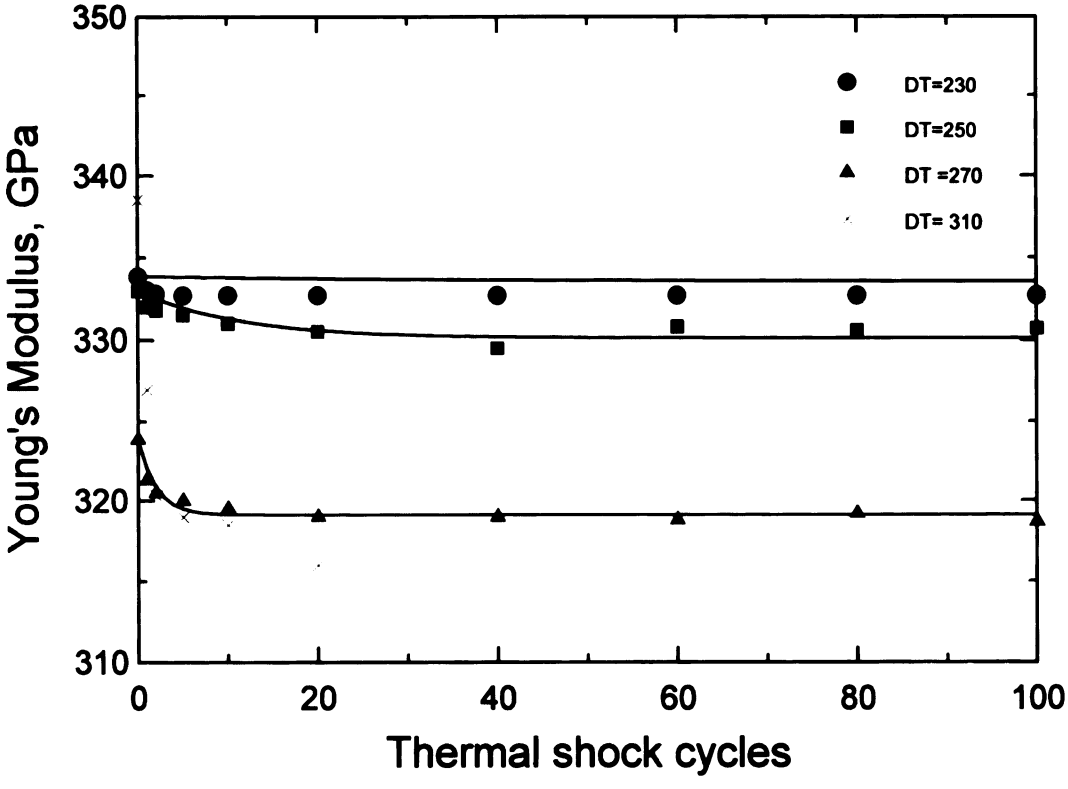

Figure 1.3.4. Young's modulus versus the cumulative number of thermal fatigue cycles for unreinforced polycrystalline quenched into a room temperature deionized water bath. The solid curves represent a least-squares fit of the data to equation 1.3.1. [12].

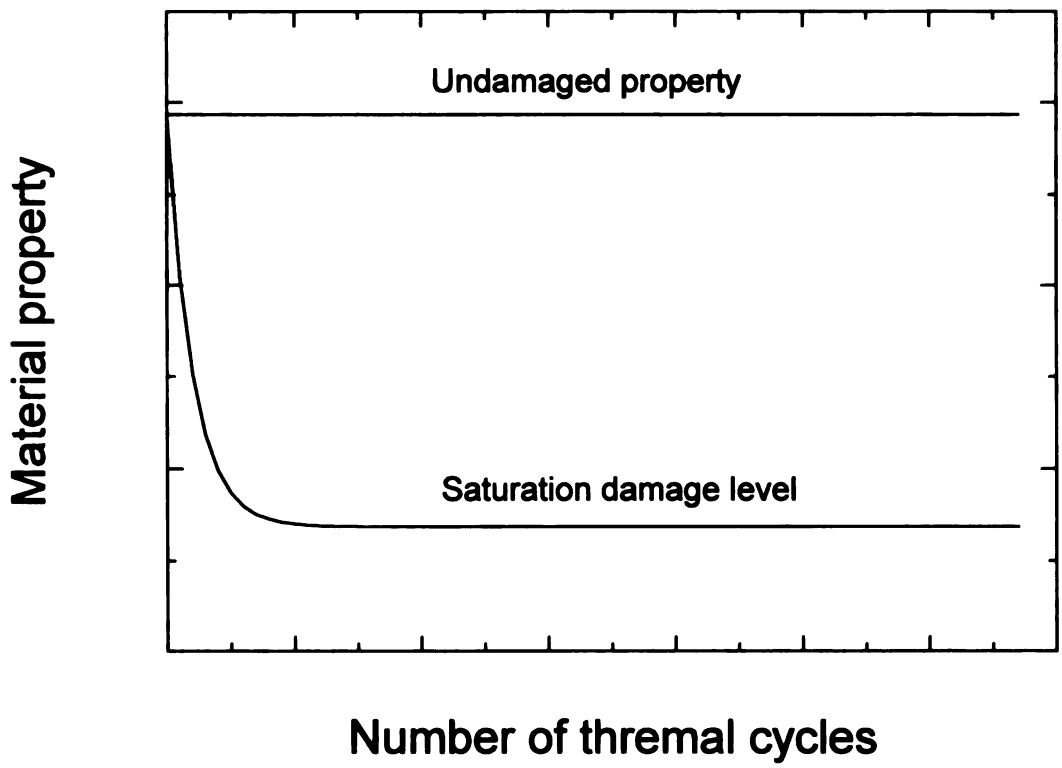

Figure 1.3.5. Schematic diagram of damage saturation behavior subject to thermal fatigue damage for ceramic materials [10-11, 29-30].

2. Experimental Procedure

2.1. Materials

Commercial polycrystalline alumina (Coors ADS 995) was cut into 10 mm × 10 mm × 1 mm specimens from 45 mm × 45 mm × 1 mm billets using K.O. Lee cutting machine. The alumina plates were sawed at a depth of 1.27 μm per pass (one forward or backward recursion) and the saw speed (left/right) was less than 0.25 cm/minute. The nominal average grain size was 4.0 μm. All specimen dimensions were measured using vernier caliper (Mitutoyo) (Appendix A).

2.2. Polishing

Before polishing, sets of 8-12 specimens were mounted on an aluminum plate (Figure 2.2.1) with super glue (Super Glue Corp.). Specimens were polished through 3 steps using a VARI/POL VP- 50 (Leco Co) polishing system. During polishing, the wheel speed was 125 rpm and the applied normal load was about 5-7 lbs. The specimens were polished with 15 μm diamond paste (Part No. 810- 914 Leco Corp.) for about 4 hours. Then using 6 μm diamond paste (Part No. 810-873 Leco Corp.), the specimens were polished for about 4 hours. Finally, the specimens were polished with 0.3 μm alumina powder (Buehler micropolish No. 40-6305-080) for about four hours until the specimen surfaces were mirror-like in appearance. To demount the specimens from the aluminum plate, the super glue was burned off in an electrical resistance furnace (Lindberg type 51442) for 60 ±5 minutes at 350 °C. The time-temperature history of the furnace for specimen demounting is given in Figure 2.2.2. and Table 2.2.1

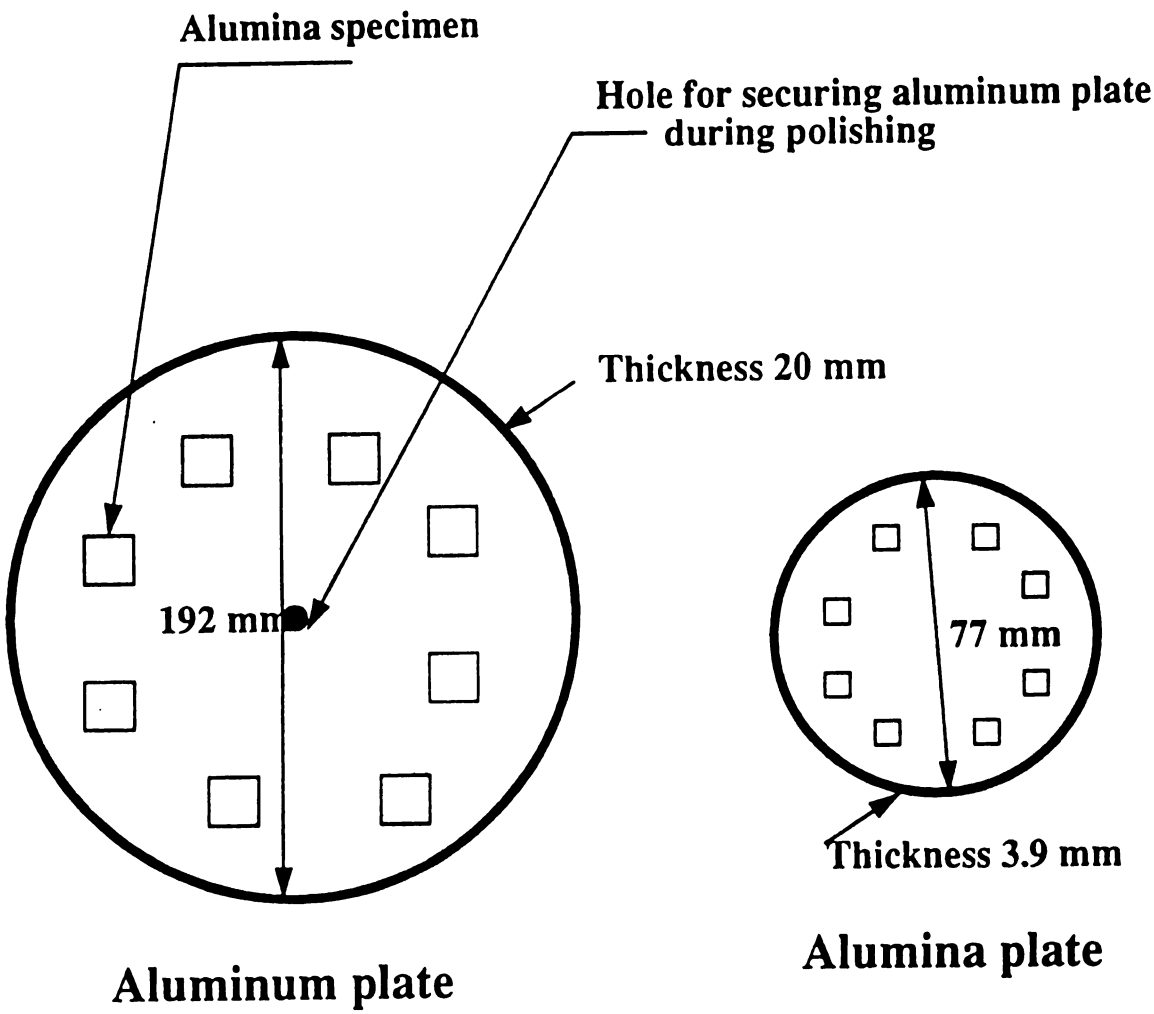

Figure 2.2.1. (a) Position of specimens on the aluminum plate for polishing specimens were superglued onto the plate. (b) Alumina plate used to place specimens on when burning off the superglue residue.

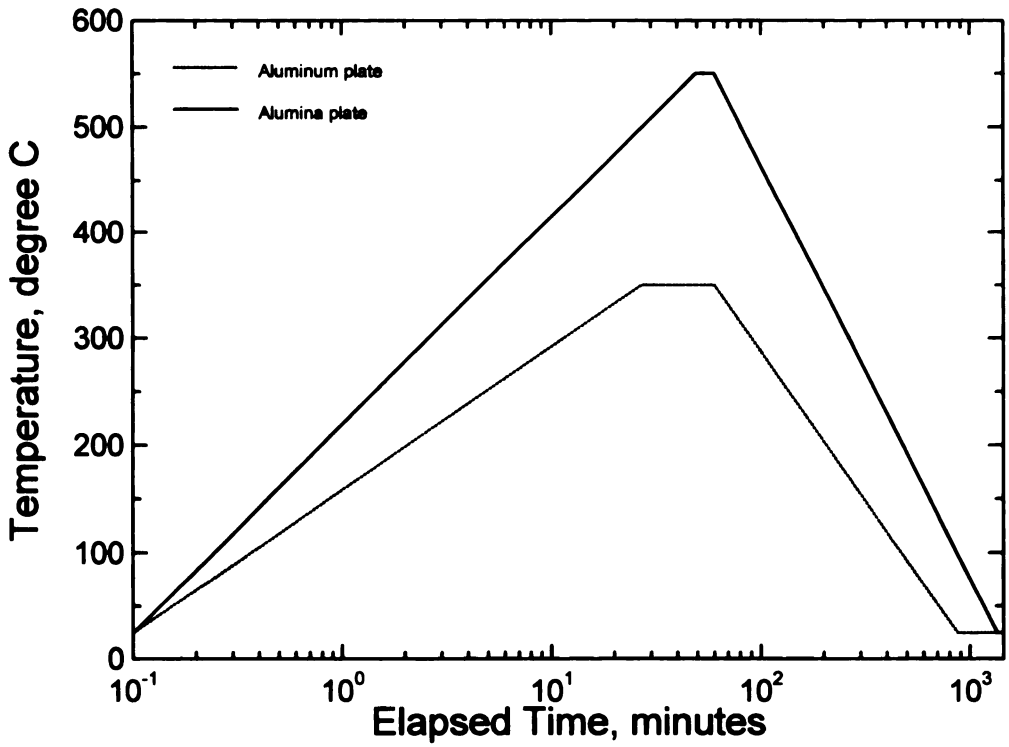

Figure 2.2.2. The heating history to demount alumina specimens from alumina plate by burning super glue using an electrical resistance furnace.

Table 2.2.1. Heating history for demounting polycrystalline alumina specimen from aluminum plate and alumina plate.

Demounting from aluminum plate		Removing residue superglue	
Temp. °C	Time, min.	Temp. °C	Time, min.
0	25	0	25
27	350	49	550
60	350	60	550
873	25	1351	25
1440	25	1440	25

After demounting, there was a super glue residue on alumina specimens. Therefore, the specimens were placed on an alumina plate (Figure 2.2.1) and the plate plus the specimens were then inserted into furnace and heated for 60 ± 5 minutes at 550 °C to remove super glue completely (Figure 2.2.2 and Table 2.2.1). To prevent the alumina specimens from "sticking" onto the alumina plate, the specimens were placed on a 1 mm thick coating of alumina powder (Buehler 0.3 micron alpha alumina) which covered the alumina plate. The thickness of the alumina powder bed was measured by a ruler with a 1 mm scale. The alumina plate contains a glassy phase that could cause sticking, but such sticking normally does not occur for temperature below 1200 °C, thus the alumina powder bed is a precaution.

2.3. Indentation

A Vickers semimacroindenter (Digital Semimacrohardness Tester, Buehler Ltd.) was used to introduce cracks in the specimens. A 49 N load was used with loading time of 17 seconds and loading speed of 80 μm/s. Indentation cracks were introduced at the center or edge of the 1 cm × 1 cm specimen surface (Figure 2.3.1). An optical microscope

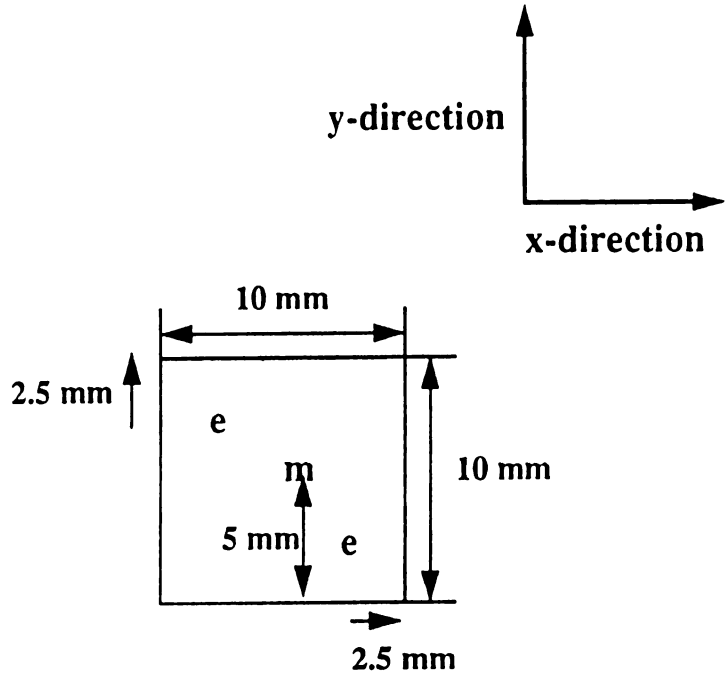

Figure 2.3.1. The position of indentations on the polycrystalline alumina specimen's surface for observation of indentation crack growth behavior.

(×200) mounted on the indenter was utilized to measure crack lengths. A digital readout gave crack lengths to the nearest 0.1 micron. The procedure for determining crack length was as follows: The marker of the optical microscope is positioned at two crack tips. The crack lengths were then measured in the longitudinal direction (x-direction) and transverse direction (y-direction).

2.4. The observation of slow crack growth after initial indentation but before commencing thermal shock

After introducing the indentation crack (see section 2.3) crack lengths were measured using an optical microscope for specimens A1-12 to 14 and A2-8 to 9. Crack growth behavior following the indentation but before commencing thermal shock was measured as a function of elapsed time (see Appendix B).

2.5. The observation of slow crack growth behavior in room temperature deionized water and in 80 °C deionized water in absence of thermal shock

To observe slow crack growth in water, the specimen (B1-3) was inserted into room temperature deionized water. The alumina specimens were positioned on the bottom of a glass beaker (400 mm Kimax) with a water depth of about 7 cm as measured by a ruler (1 mm scale). Crack lengths were measured after the specimens were removed from the water. The crack length versus elapsed time are given in Appendix B.

Crack length behavior in 80 °C also was investigated. Specimen (B1-4) was inserted into 7 cm deep deionized water in a glass beaker (400 ml Kimax). An alumina specimen

was positioned 5 cm from the bottom of beaker using the steel wire screen (0.7 × 0.7 mm grid with individual wires 0.03 mm in diameter). The alumina specimen was heated to about 80 °C on Model 4658 stirrer/hot hot plate (Cole-Parmer Instrument Co.). The average heating rate was 3.5 °C/minute. The temperature was measured by mercury in glass thermometer (VWR SCIENTIFIC INC 61016-208) with 1 °C scale. The specimen was kept at 80 °C for about 2 hours then cooled at an average rate of 0.35 °C/minute by turning off the hot plate. Within about 2 and 1/2 hours the water reached room temperature (23 °C). Specimen (B1-4) was removed from the water and the crack lengths were measured using an optical microscope. The 2.5 hour immersion in 80 °C water was repeated 9 times. The resulting crack lengths and temperatures are given in Appendix C.

2.6. Thermal shock testing

After the indentation cracks had aged for at least 24 hours, the specimens were placed in the furnace for thermal shock testing. The furnace, which was constructed for thermal shock testing, was heated by electrical resistance (Figure 2.6.1) at a rate of about 2.0 °C per minute to temperatures ranging from 272 °C to 352 °C. The temperature was measured by a digital readout attached to power controller (CN5001K, Omega Engineering Inc.) using a K-type thermocouple. The thermocouple was located about 10 cm from the lid of furnace. The temperature of deionized water bath was typically 22 °C as measured by mercury in glass thermometer (VWR SCIENTIFIC INC. 61016-208) which had a 1 °C scale. Quench bath temperature measurements were made before

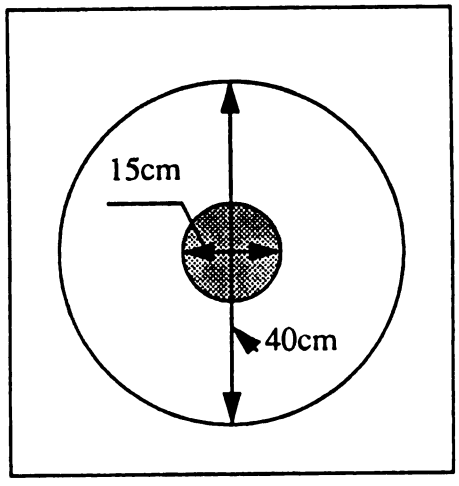

(a) Top view

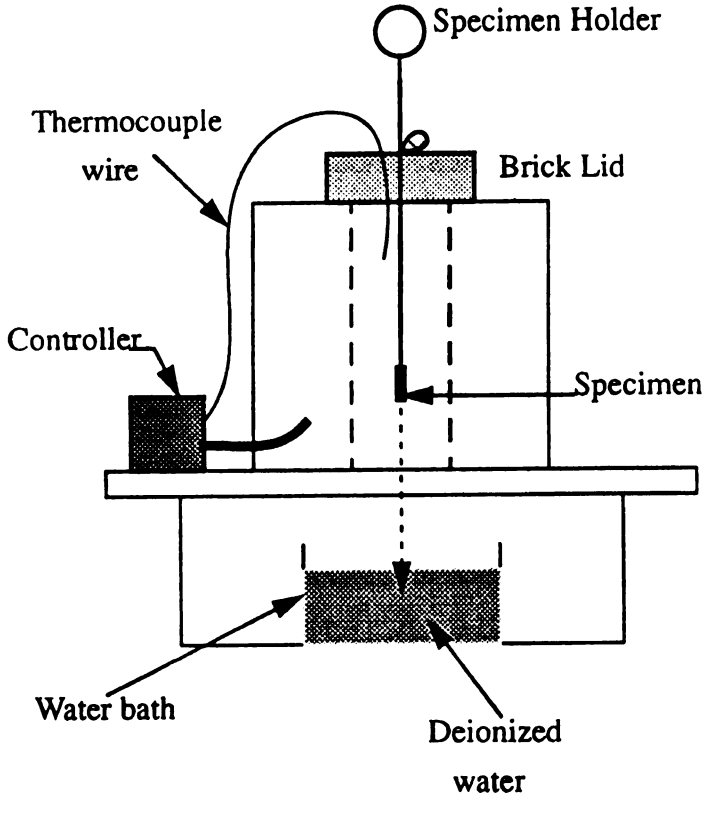

(b) side view

Figure 2.6.1. Schematic of the electrical resistance heated furnace used in the thermal fatigue experiments. The average heating rate was about 2 °C/min.

specimen was placed in an electrical furnace. The thermometer was located approximately 3.5 cm from the bottom of water bath and 9.5 cm from the specimen.

The specimen was introduced into the furnace using a specimen holder (Figure 2.6.2) which was made for this study. The specimen holder consisted of tongs, stainless steel wire screen, and a steel wire (Figures 2.6.2 and 2.6.3). The tongs were used to hold the specimen in a fixed position within the furnace. If the tongs were removed then the alumina specimen plunged into the deionized water bath. Using the tongs, the specimen was placed approximately 25 cm from the top of the furnace (as measured by a 1 mm scale ruler). A wire screen which has 0.7 × 0.7 mm grid made up of wires 0.03 mm diameter held the specimen. The wire screen was made into a bowl shape approximately 1.8 cm × 1.7 cm and 1.2 cm diameter, as measured by ruler with 1 mm scale. The deionized water flowed through the wire screen during quench thus steel wire screen likely did not significantly perturb the thermal shock test.

A steel wire with about 64 cm in length was made from 0.85 mm diameter wire (as measured by ruler with 1 mm scale) and formed the "backbone" of the specimen holder. The steel wire (0.85 mm in diameter) was flexible thus three strands of wire were twisted together (Figure 2.6.3).

The specimen remained in the furnace for about 10 to 15 minutes supported by the specimen holder. The specimen then was quenched into the water bath by removing the tongs to move the specimen from the furnace to the water bath. The specimen was located approximately 2.5 cm above (measured by ruler with 1 mm scale) the water bath.

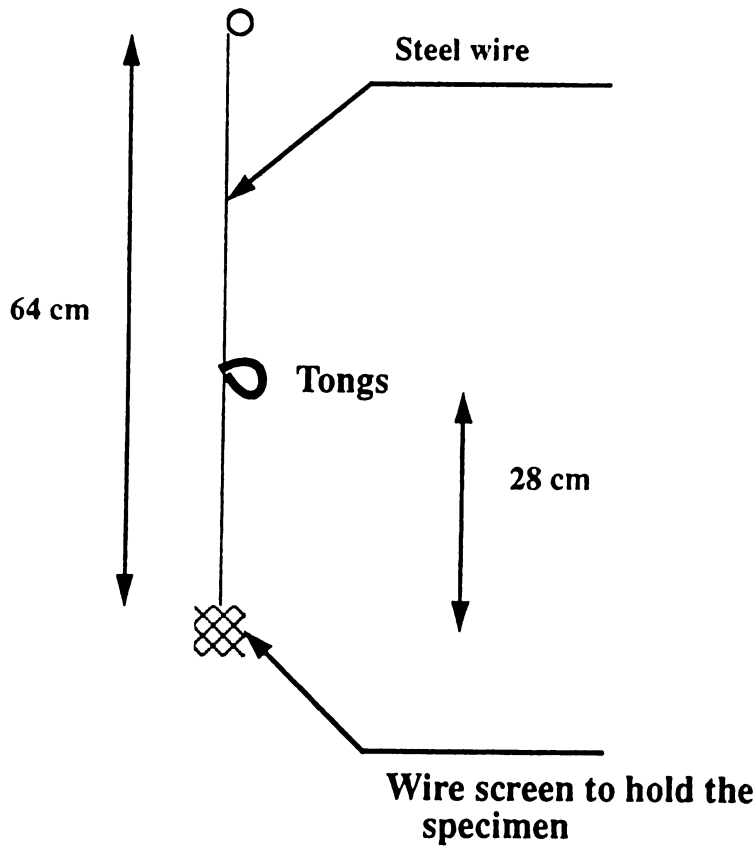

Figure 2.6.2. Schematic diagram of the thermal shock testing specimen holder which has three parts: steel wire, tongs, and wire screen.

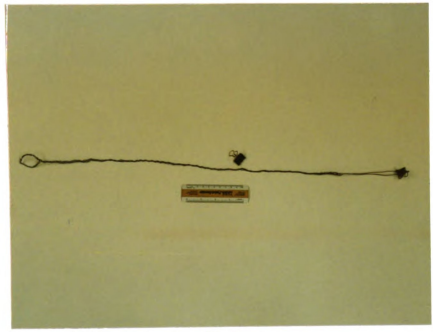

(a)

(b)

Figure 2.6.3. The photograph of (a) entire specimen holder which has three parts of steel wire, tongs, and wire net for thermal shock testing (b) body of steel wire which was twisted 3 times.

The time elapsed from the initial specimen movement until the specimen reached the water bath was about 1 second.

The water bath consisted of a 27.5 cm × 14.5 cm × 20.5 cm plastic container containing a volume of approximately 5 liters of deionized water. The depth of deionized water was about 14 cm (measured by ruler with 1 mm scale) for all of the thermal shock experiments. After 1 minute, the specimen was removed from the water bath. Water remaining on the specimen was removed with paper towels (Kimwipes 34155 Kimberly-Clark).

The specimen was then placed on movable stage of semimacroindenter. Crack lengths were measured using an optical microscope with a digital readout which is attached to semimacroindenter. The elapsed time between removing specimen from the water bath and measuring crack length was about 5 minutes.

The thermal shock testing was done in two groups. In the first group the specimens were individually thermally fatigued for total of ten thermal cycles. In the second group, the specimens were individually fatigued for a total of twenty shock cycles. Specimens thermally shocked for 10 cycles were at the following quench temperature differences: 250 (A4-13), 270 (A4-14), 290 (A4-15), 295 (A6-2), 300 (A5-3), 305 (A5-12), 310 (A5-4), 315 (A5-11), 320 (A5-5), 325 (A5-8), and 330 °C (A5-7). For the specimens quenched 20 times, the quench temperature differences were 250 (A6-3), 270 (A6-4), 295 (A6-5), 300 (A5-10), 305 (A5-14), and 310 °C (A6-1).

2.7. Comparison of transverse and longitudinal crack length for a set of Vickers cracks subjected to thermal fatigue

Vickers indentation cracks were introduced on the surface of 56.1 mm × 9.4 mm × 0.93 mm bar specimen (Figure 2.7.1). The dimension , the orientation of the x-y axes of the bar and the position of indentations L_1, L_2, and L_3 are given in Figure 2.7.1. After 24 hours in air, the specimen was placed in the quench furnace at 282 °C for 10 to 15 minutes (see section 2.6.). The specimen was quenched into a 22 °C deionized water which was about 14 cm deep. The temperature of water bath was measured by a mercury in glass thermometer (VWR SCIENTIFIC INC. 61016-208) at nearly the same position as that used to measure the water bath temperature for the square alumina specimens (see section 2.6). The same water container as that used for thermal fatigue testing (see section 2.6) was used. The specimen holder screen (see Figure 2.6.2) was 4.5 cm long to prevent the bar-shaped specimen from falling from the specimen holder. The specimen was located about 20 cm from the top of electrical resistance furnace. The bar-shaped specimen was plunged into a deionized water bath within less than 1 second. The specimen in the water bath was held at 2.5 cm from the bottom of the water bath. After 1 minute, the specimen was removed from the water bath. Water remaining on the specimen was removed with paper towels (Kimwipes 34155 Kimberly-Clark). After the residual water was blotted of the specimen, the specimen placed on the semimacroindenter stage for crack length measurements. Crack lengths were measured by optical microscope of semimacroindenter which has digital readout (see section 2.6).

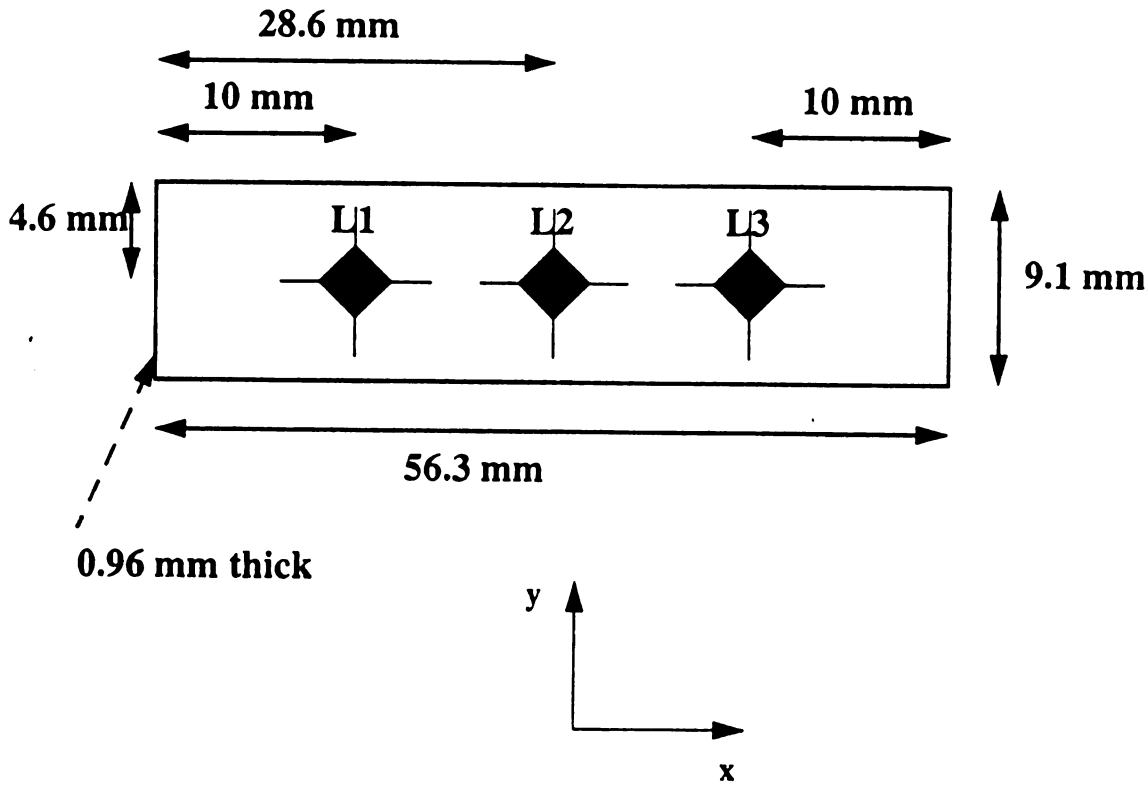

Figure 2.7.1. The dimension of bar-shaped polycrystalline alumina specimen and the position of indentation cracks. This part of the study investigated possible asymmetry in the group in the x and y directions during thermal fatigue.

2.8 The observation of grain bridging in for specimens thermally shocked during this study

Three thermally shocked specimens (A4-14 at 270 °C, A5-3 at 300 °C, and A5-5 at 320 °C) were gold coated in sputter coater (Model SC 500, EMSCOPE) for 3 minutes. Specimens were mounted on JEOL 9.5 × 9.5 mm aluminum specimen mounts (TED PELLA, Inc.) After gold coating for 3 minutes, the thickness of gold coating was approximately 21 nm, for a deposition rate of 7 nm/min [32]. Specimens were inserted into a scanning electron microscope (SEM, JEOL, JSM 6400V) chamber using specimen holder. The accelerating voltage was 20 kV. Micrographs of the crack shapes were taken at a magnification of 150 and bridging area micrographs were taken at a magnification of 2500.

3. Results and Discussions

3.1. Slow crack growth after initial indentation but before commencing thermal shock

To evaluate the initial slow crack growth for the indentation cracks prior to thermal shock testing, the initial indentation crack lengths were measured using an optical microscope. The crack lengths and time were given by tables in Appendix B.

Plots of crack length versus time are shown in Figures 3.1.1-3.1.7. Following each of the Vickers indentations, the cracks grew slowly after introducing the indentation crack. The crack length typically saturated within about 30 minutes following the indentation. In Figures 3.1.1 to 3.1.7, the open circles represent crack length of transverse direction, while the open squares indicate the longitudinal direction. Closed circles represent the crack length for the average of the transverse direction and the longitudinal direction. For the 7 specimens included in the slow crack growth study, the relative change in the crack length is defined by

$$\Delta C = \frac{C_{max}}{C_0} \tag{3.1.1}$$

where C_0 = mean of initial crack lengths for the two radial cracks that make up the Vickers crack system.

C_{max} = mean of the saturated crack lengths for a given Vickers crack system.

In this study, ΔC varied from 1.024 to 1.130. The ΔC's and the time at which last measurement was done are given in Table 3.1.1.

Table 3.1.1. Slow crack growth (in air) after initial indentation for unreinforced polycrystalline alumina specimens.

Specimen label	ΔC	T_{max}* (minutes)
A1-11	1.024	1474
A1-13	1.077	1386
A1-14	1.130	1495
A2-8e**	1.031	1424
A2-8m***	1.034	1482
A2-9e**	1.056	1436
A2-9m***	1.035	1435

* T_{max} is the time at which last measurement was done.
** e means the edge of specimen.
*** m means the middle of specimen.

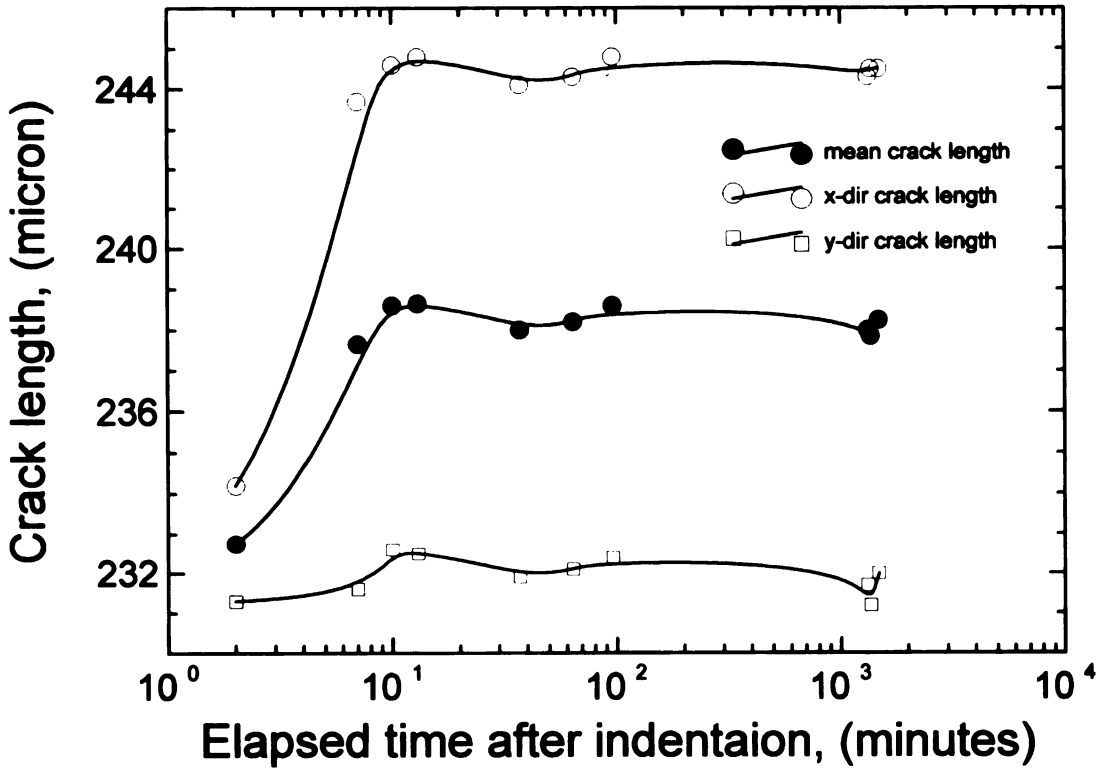

Figure 3.1.1. Indentation crack lengths (x- and y-direction, see Figure 2.3.1) as a function of elapsed time following indentation for polycrystalline alumina (specimen A1-11).

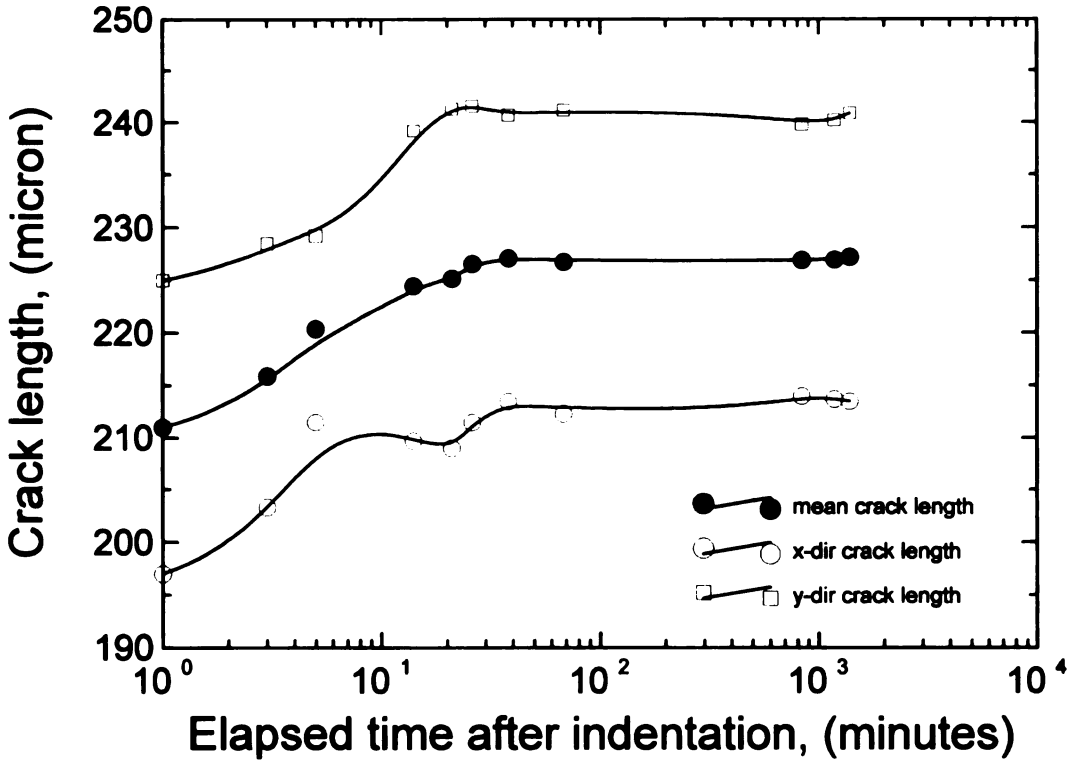

Figure 3.1.2. Indentation crack lengths (x- and y-direction, see Figure 2.3.1) as a function of elapsed time following indentation for polycrystalline alumina (specimen A1-13).

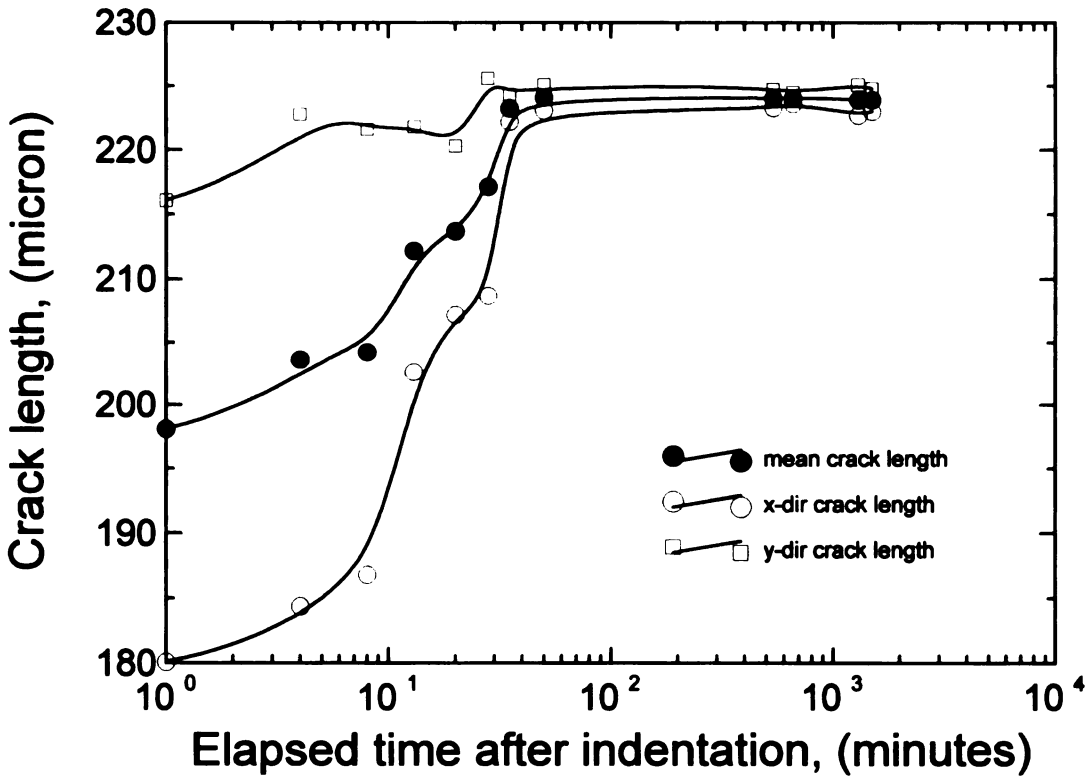

Figure 3.1.3. Indentation crack lengths (x- and y-direction, see Figure 2.3.1) as a function of elapsed time following indentation for polycrystalline alumina (specimen A1-14).

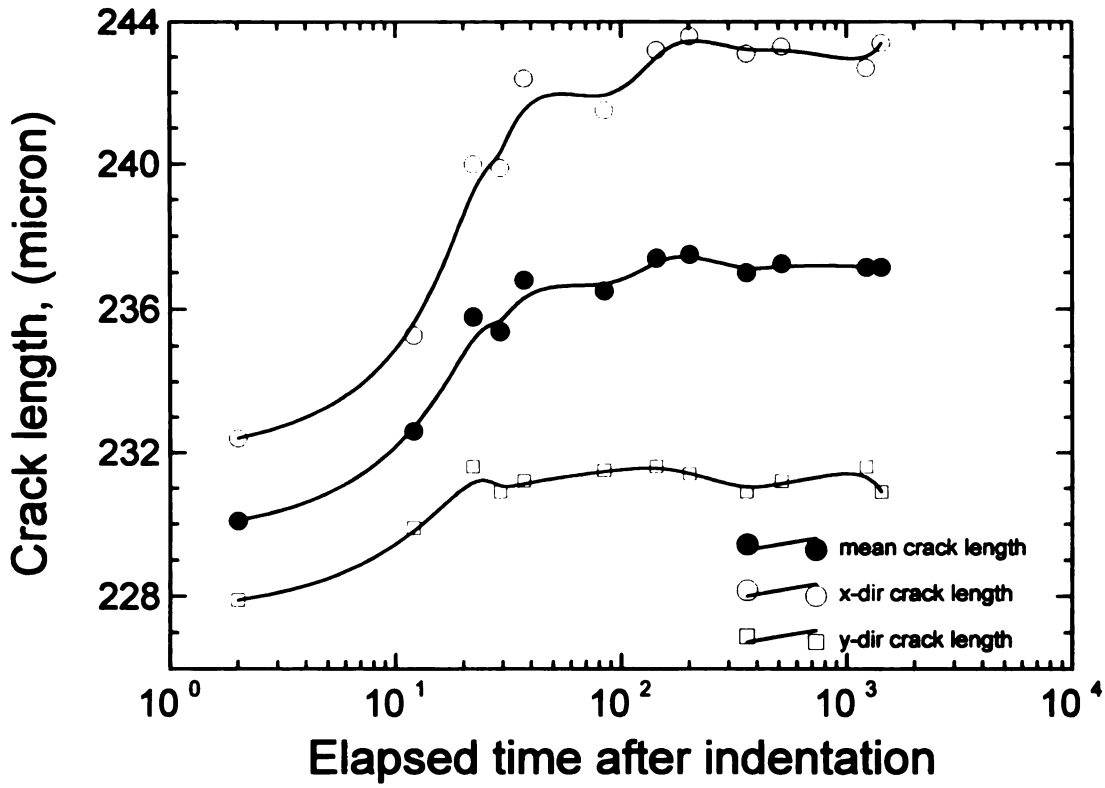

Figure 3.1.4. Indentation crack lengths (x- and y-direction, see Figure 2.3.1) as a function of elapsed time following indentation for polycrystalline alumina (specimen A2-8e where "e" means the indentation was placed near the edge of the specimen).

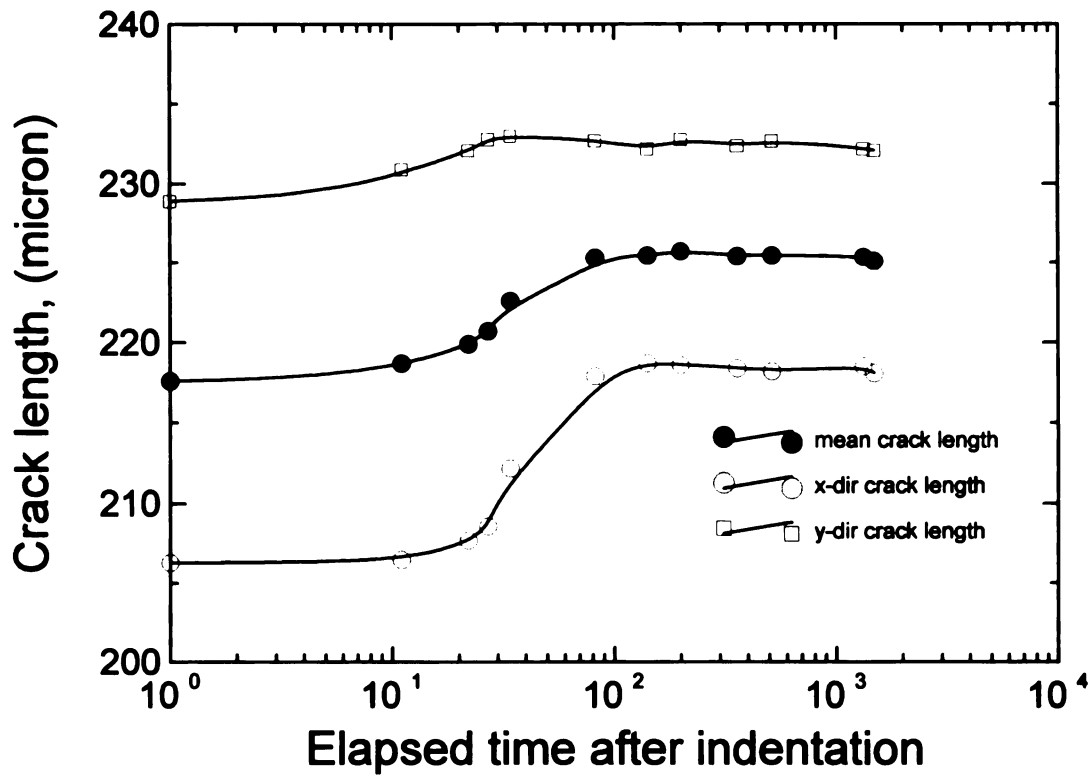

Figure 3.1.5. Indentation crack lengths (x- and y-direction, see Figure 2.3.1) as a function of elapsed time following indentation for polycrystalline alumina (specimen A2-8m where "m" means the indentation was placed near the middle of the specimen).

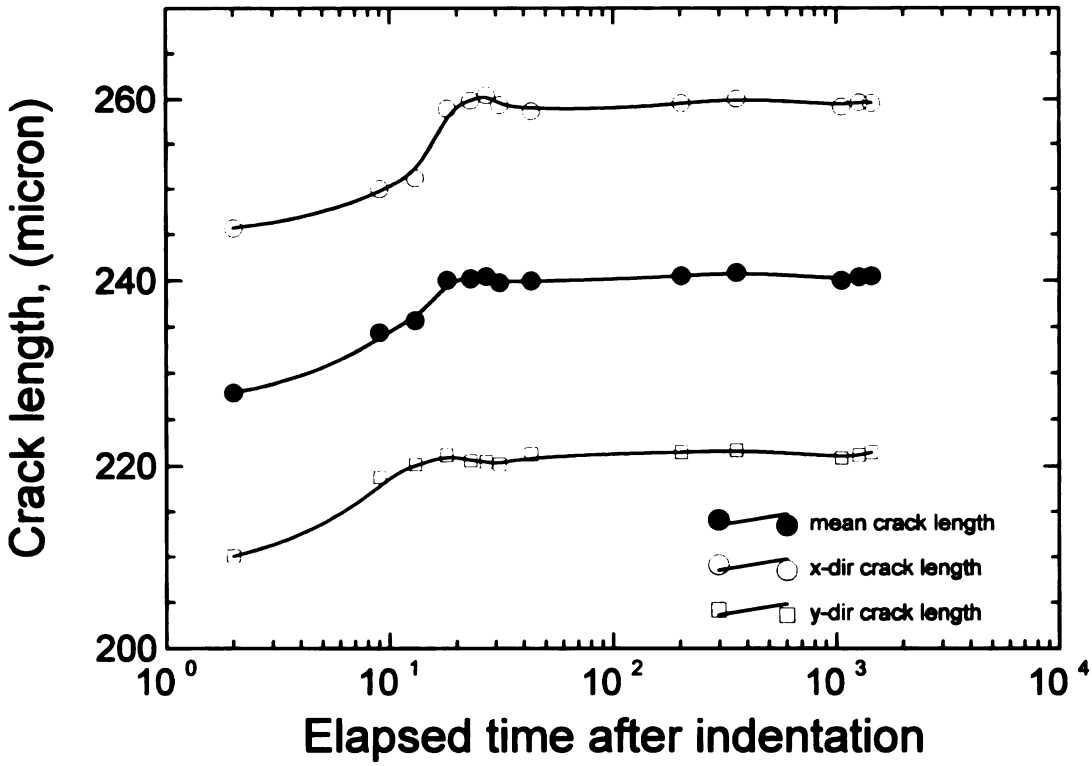

Figure 3.1.6. Indentation crack lengths (x- and y-direction, see Figure 2.3.1) as a function of elapsed time following indentation for polycrystalline alumina (specimen A2-9e where "e" means the indentation was placed near the edge of the specimen).

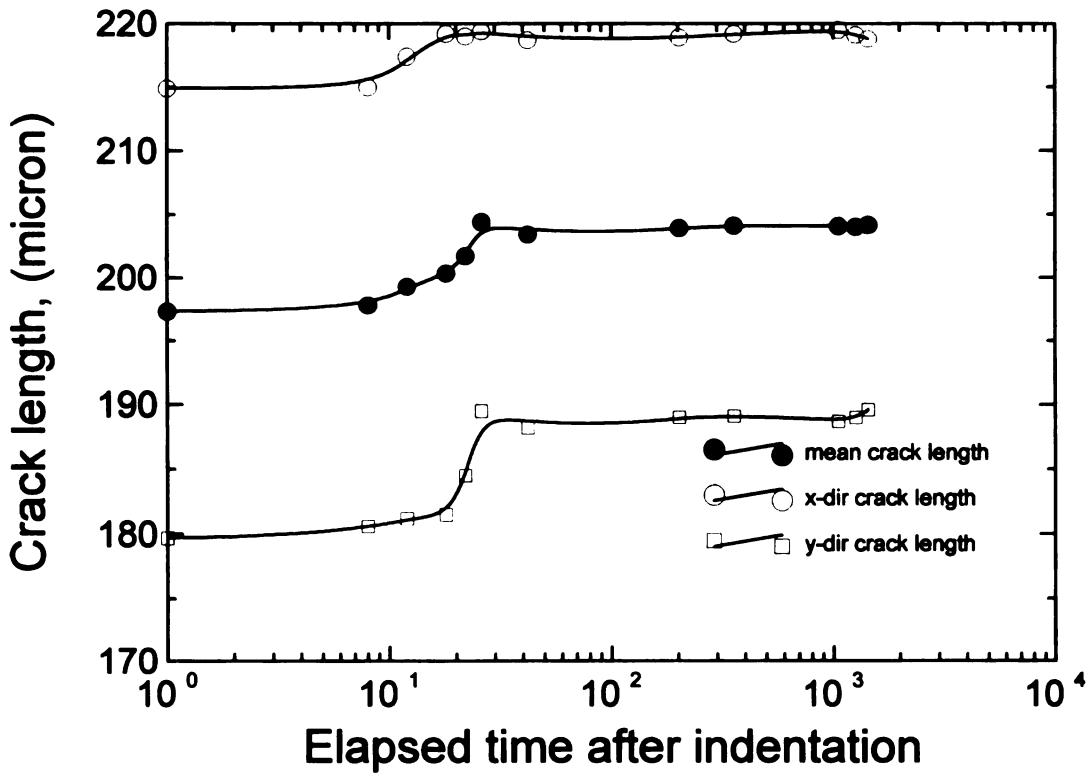

Figure 3.1.7. Indentation crack lengths (x- and y-direction, see Figure 2.3.1) as a function of elapsed time following indentation for polycrystalline alumina (specimen A2-9m where "m" means the indentation was placed near the middle of the specimen).

3.2. Crack growth behavior in room temperature and 80 °C deionized water in the absence of thermal shock

Water can cause crack extension via an environmentally-assisted slow crack growth process. Water may affect crack growth during thermal shock testing when the specimens were in the water bath. Therefore, the effect of water on crack extension was investigated.

A specimen (B1-3) was inserted into deionized water at room temperature after being indented and aged for 24 hours in air. The crack lengths were measured as a function of time (Figure 3.2.1). The circles represent mean crack length, the diamonds indicate the transverse direction crack length and squares indicate the crack length in the longitudinal direction. The indentation crack length did not change significantly (less than 1 percent, see Appendix C) during up to 92 hours of immersion in the deionized water. The crack length data as a function of immersion time in the deionized water are given in Appendix C.

To observe the effect of hot water (~ 80 °C) on a Vickers indentation crack system, a specimen (B1-4) was first immersed in room temperature deionized water after being indented and aged for 24 hours in air. Then the water and specimen were slowly heated together to about 80 °C in deionized water. The specimen and water were cooled to room temperature (about 23 °C) in the air. The crack length change (Figure 3.2.2) was less than 1 percent (see Appendix C). Thus the hot water (~ 80 °C) apparently does not cause the cracks to extend. The crack lengths for each measurement during the test are given in Appendix C.

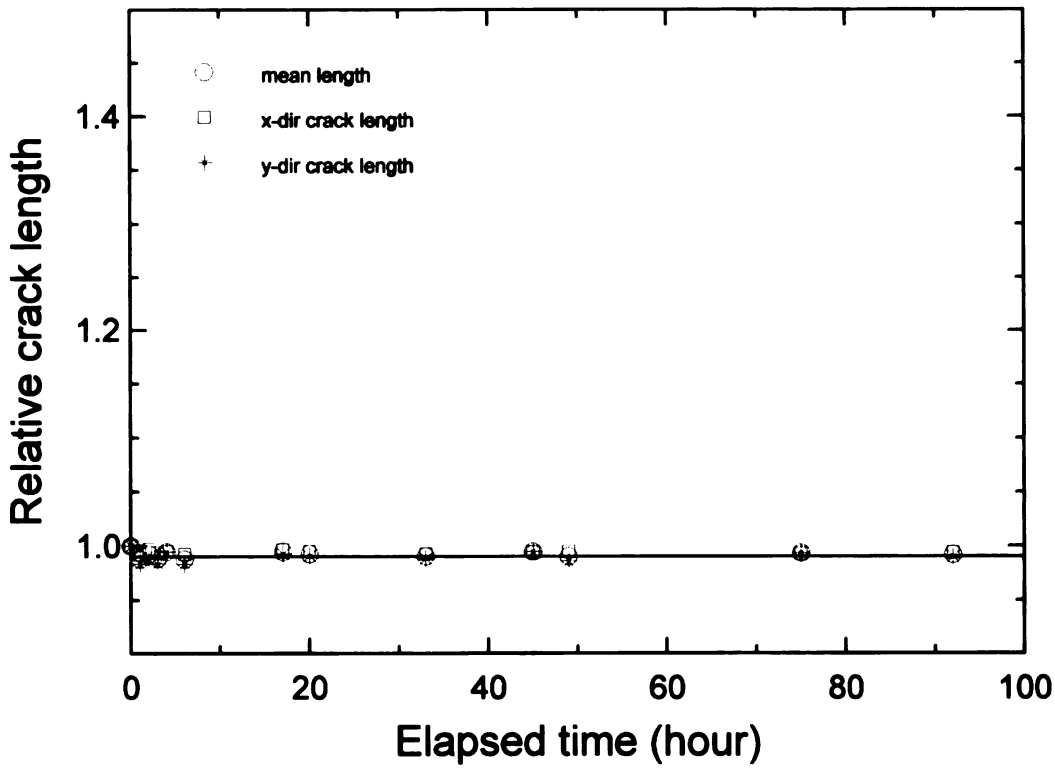

Figure 3.2.1. Crack growth behavior versus elapsed time in room temperature deionized water for unreinforced alumina specimen (specimen B1-3).

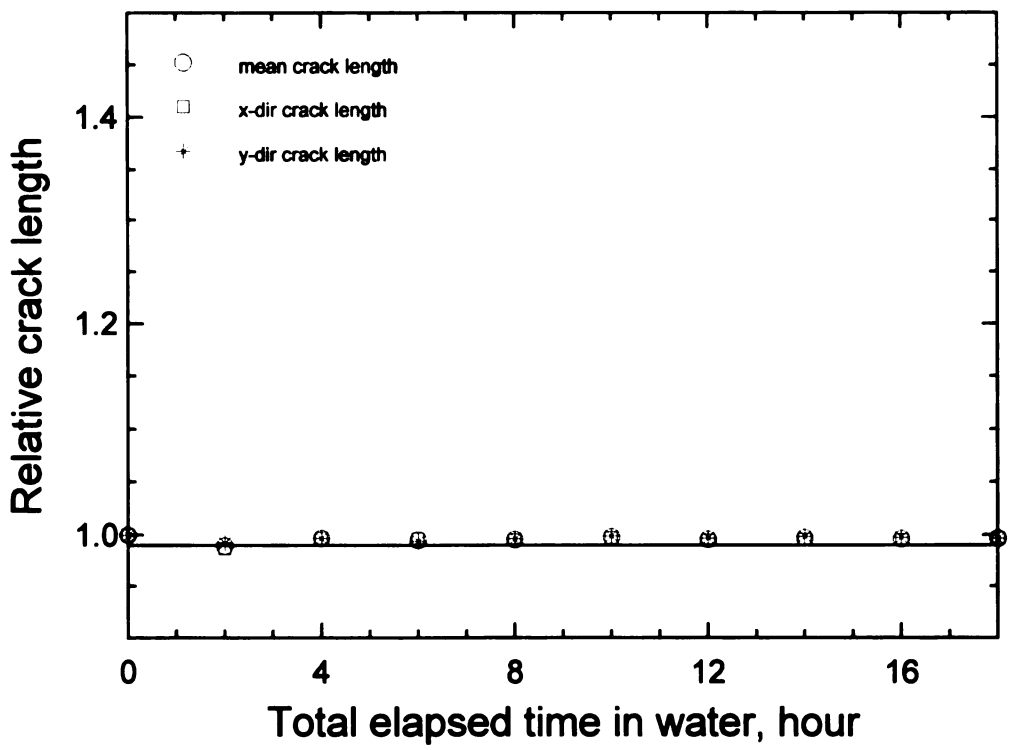

Figure 3.2.2. The crack growth behavior in deionized water at 80 °C held for 2 hours for specimen B1-4. Crack length measurements were made after the specimen had been at 80 °C (see section 2.5)

3. 3. Thermal fatigue behavior for unreinforced alumina

3. 3. 1. Thermal cycling to a maximum of ten thermal shock cycles

Thermal shock tests were done for quench temperature differences ranging from 250 to 330 °C (Figure 3.3.1-3.3.11). The crack length data for specimens that underwent a total of ten thermal shock cycles are given in appendix D.

From equation 1.3.2 (section 1.3), the crack length as a function of cumulative number of thermal shock cycles can be expressed as

$$c(N) = c_1 - (c_1 - c_0)\exp(-c_2 N) \tag{3.3.1}$$

where c = the crack length which is a function of the cumulative number of thermal shock cycles

c_0 = the initial crack length from data

c_1 = a free parameter which corresponds to saturated crack length

c_2 = free parameter corresponds to rate constant.

The relative crack increments, $\frac{c(N) - c_0}{c_0}$ at temperature differences ranging from 250 °C to 330 °C are plotted in Figures 3.3.1-3.3.11. The solid curves in figures were obtained by least-squares fit to equation 3.3.1. For quench temperature differences ranging from 250 °C to 325 °C, the saturated crack length ranged 273.54 μm to 638.52 μm (Table 3.3.1). The correlation coefficients of least-squares fit were higher than 0.94 except for quench temperature differences of 300, and 310 °C (Table 3.3.1). The cracks increased with an increasing number of thermal shock cycles. Eventually, the thermal

fatigue damage saturated. Figure 3.3.12 gives the results of crack propagation behavior due to the temperature difference at (a) 250-300 °C and at (b) 305-330 °C.

At a quench temperature difference 330 °C, the crack growth behavior is different from the crack growth behavior for lower temperature differences. After the fourth quench at 330 °C, the crack grew abruptly to the edge of the specimen. Thus the crack length was not measured because it was out of range of the scale on microscope. Figure 3.3.11 shows the crack growth behavior at the quench temperature difference of 330 °C.

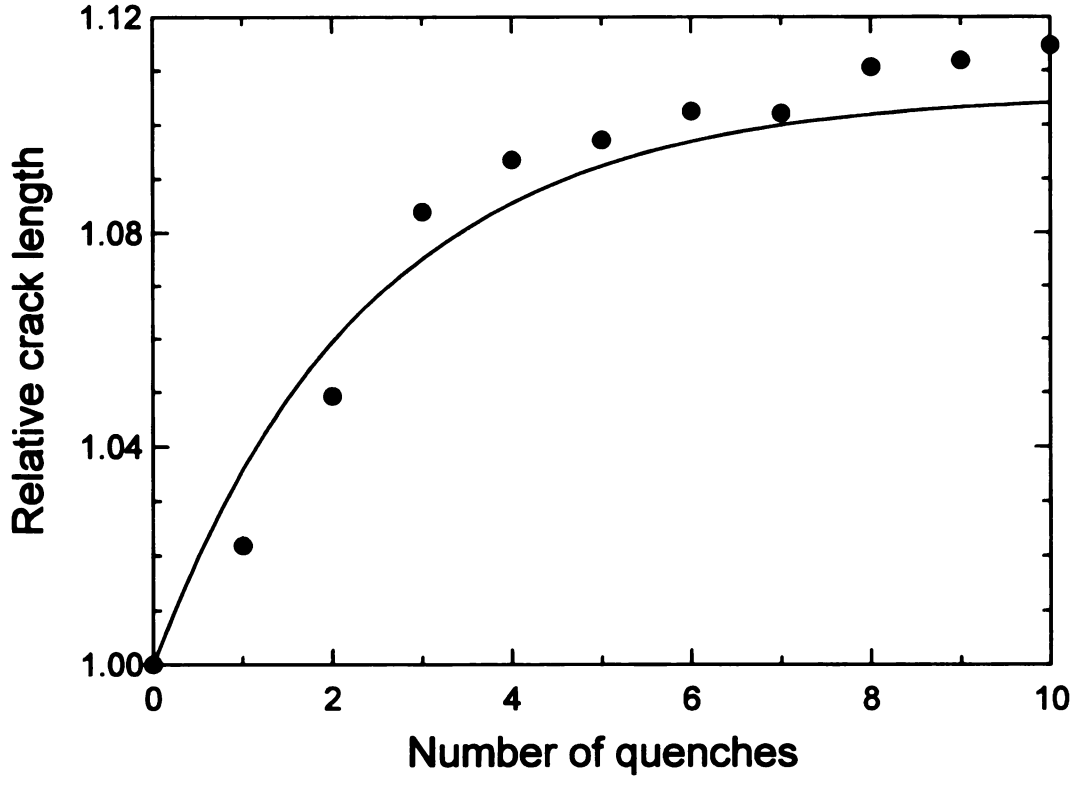

Figure 3.3.1. The crack growth behavior versus the cumulative number of thermal shock cycles a total of 10 thermal shock cycles, $\Delta T = 250\ ^{\circ}C$ (specimen A4-13). The solid line represents the least-squares fit to equation 3.3.1.

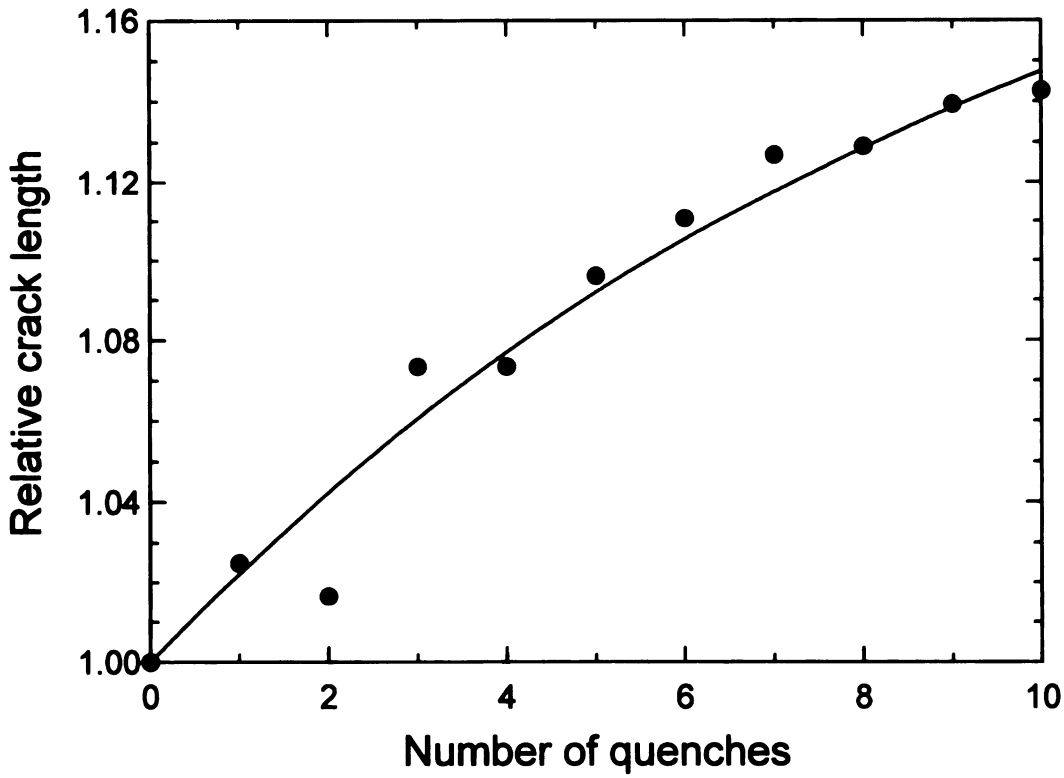

Figure 3.3.2. The crack growth behavior versus the cumulative number of thermal shock cycles a total of 10 thermal shock cycles, $\Delta T = 270\ ^{\circ}C$ (specimen A4-14). The solid line represents the least-squares fit to equation 3.3.1.

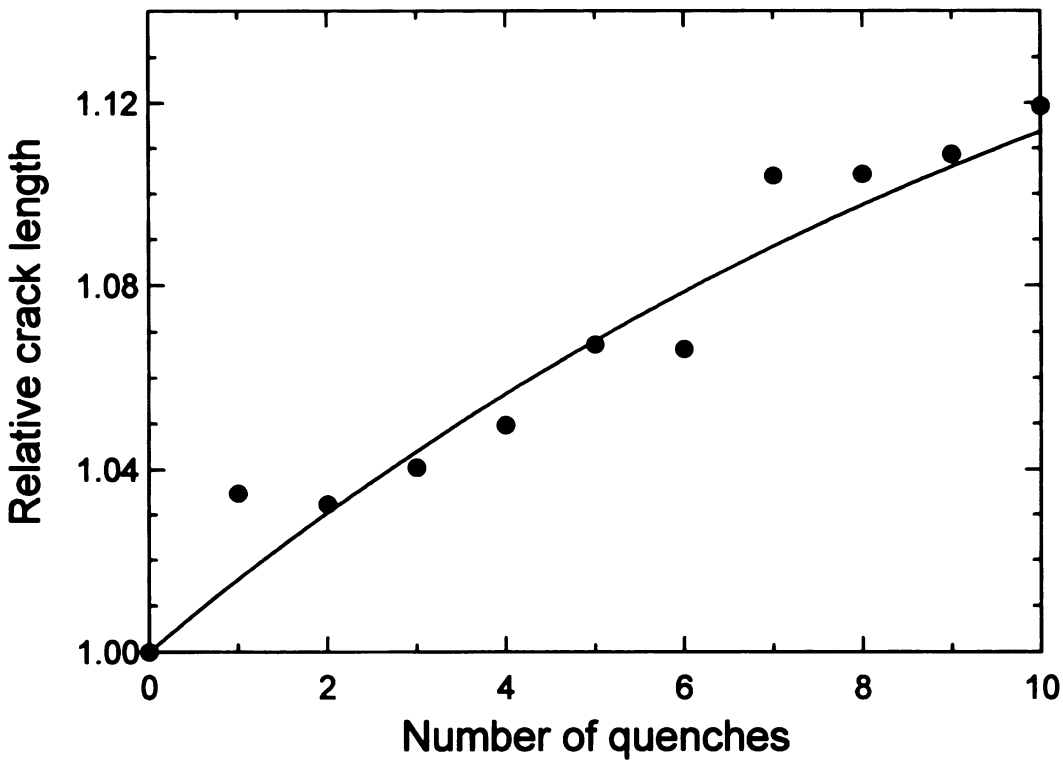

Figure 3.3.3. The crack growth behavior versus the cumulative number of thermal shock cycles a total of 10 thermal shock cycles, $\Delta T = 290\ ^{\circ}C$ (specimen A4-15). The solid line represents the least-squares fit to equation 3.3.1.

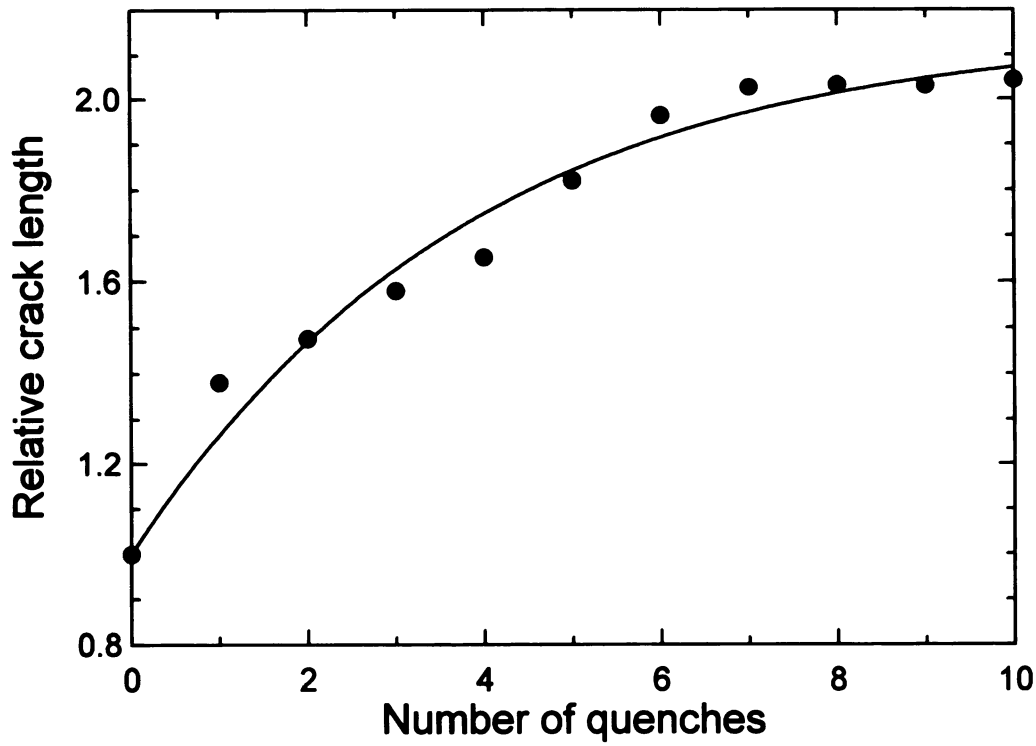

Figure 3.3.4. The crack growth behavior versus the cumulative number of thermal shock cycles a total of 10 thermal shock cycles, $\Delta T = 295\ ^{o}C$ (specimen A6-2). The solid line represents the least-squares fit to equation 3.3.1.

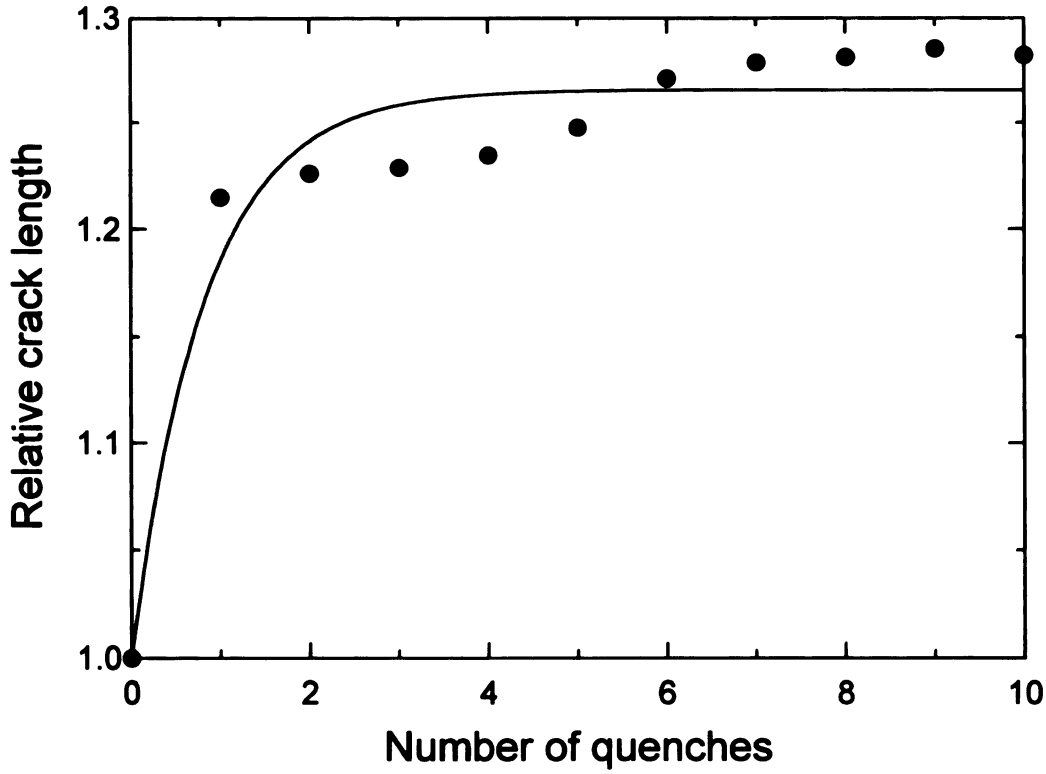

Figure 3.3.5. The crack growth behavior versus the cumulative number of thermal shock cycles a total of 10 thermal shock cycles, $\Delta T = 300\ ^{o}C$ (specimen A5-3). The solid line represents the least-squares fit to equation 3.3.1.

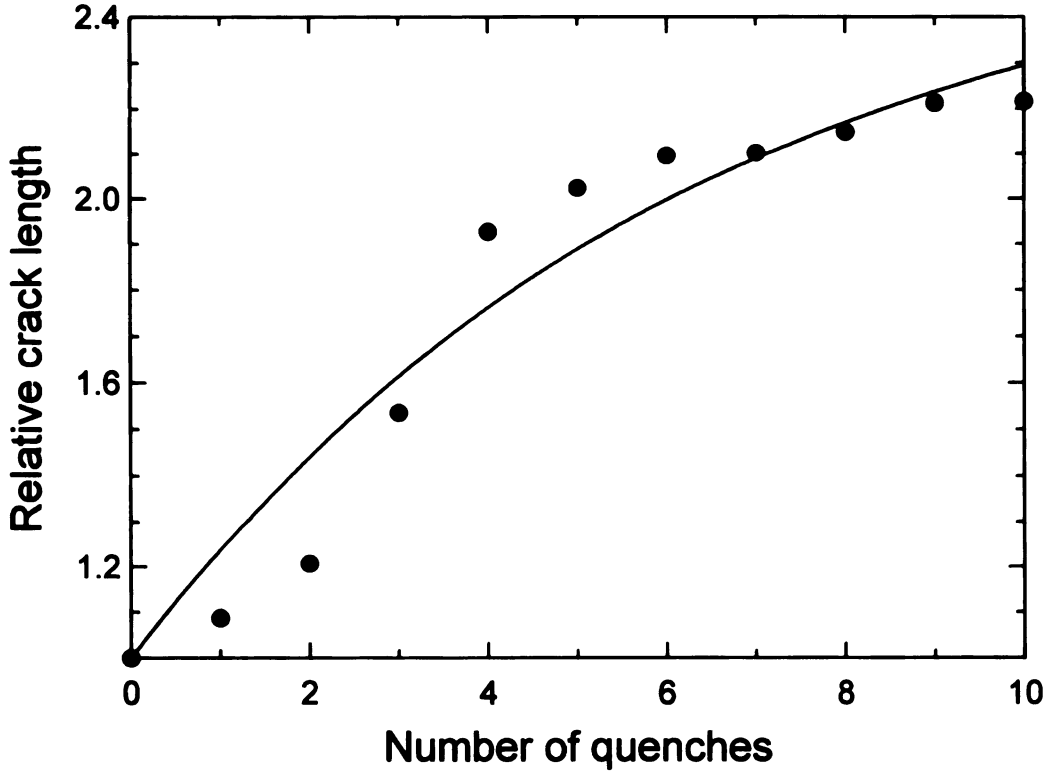

Figure 3.3.6. The crack growth behavior versus the cumulative number of thermal shock cycles a total of 10 thermal shock cycles, $\Delta T = 305\ ^{o}C$ (specimen A5-12). The solid line represents the least-squares fit to equation 3.3.1.

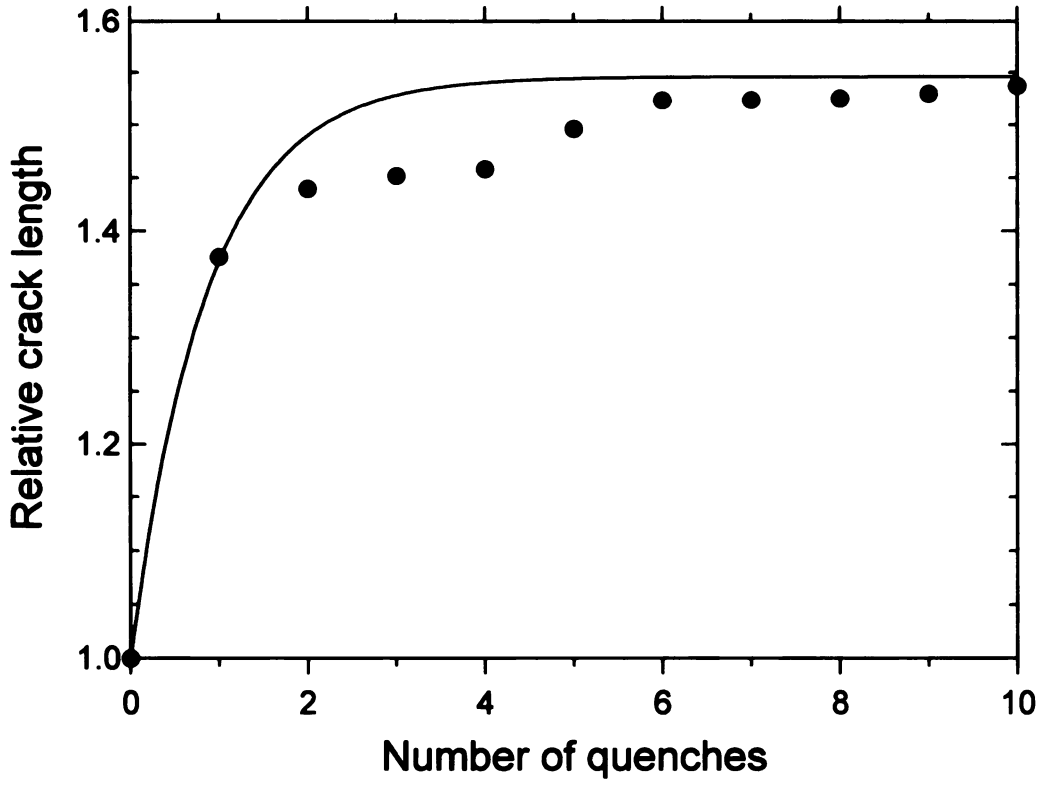

Figure 3.3.7. The crack growth behavior versus the cumulative number of thermal shock cycles a total of 10 thermal shock cycles, $\Delta T = 310\ ^{o}C$ (specimen A5-4). The solid line represents the least-squares fit to equation 3.3.1.

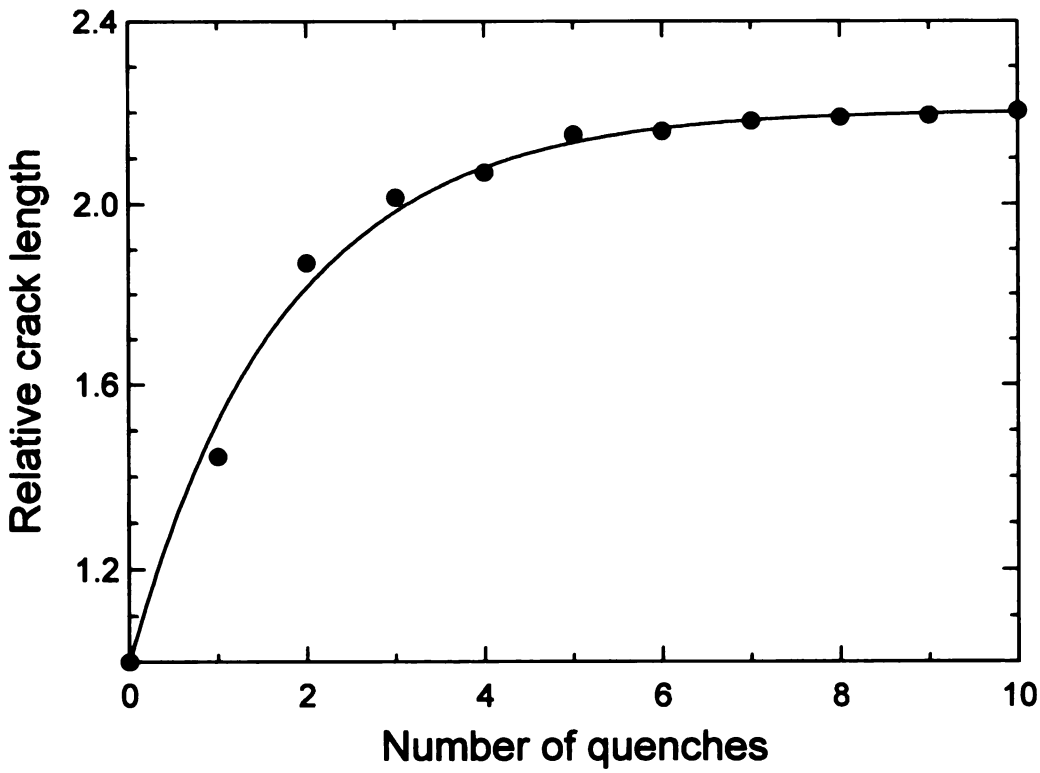

Figure 3.3.8. The crack growth behavior versus the cumulative number of thermal shock cycles a total of 10 thermal shock cycles, $\Delta T = 315\ ^{\circ}C$ (specimen A5-11). The solid line represents the least-squares fit to equation 3.3.1.

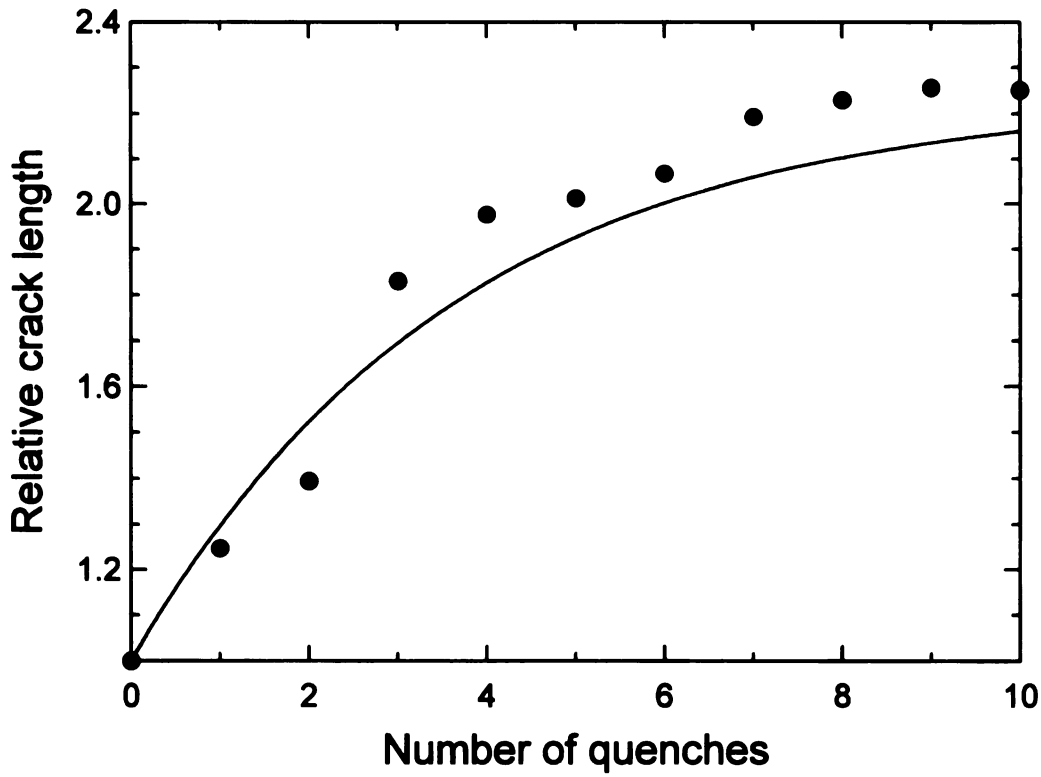

Figure 3.3.9. The crack growth behavior versus the cumulative number of thermal shock cycles a total of 10 thermal shock cycles, $\Delta T = 320\ ^{\circ}C$ (specimen A5-5). The solid line represents the least-squares fit to equation 3.3.1.

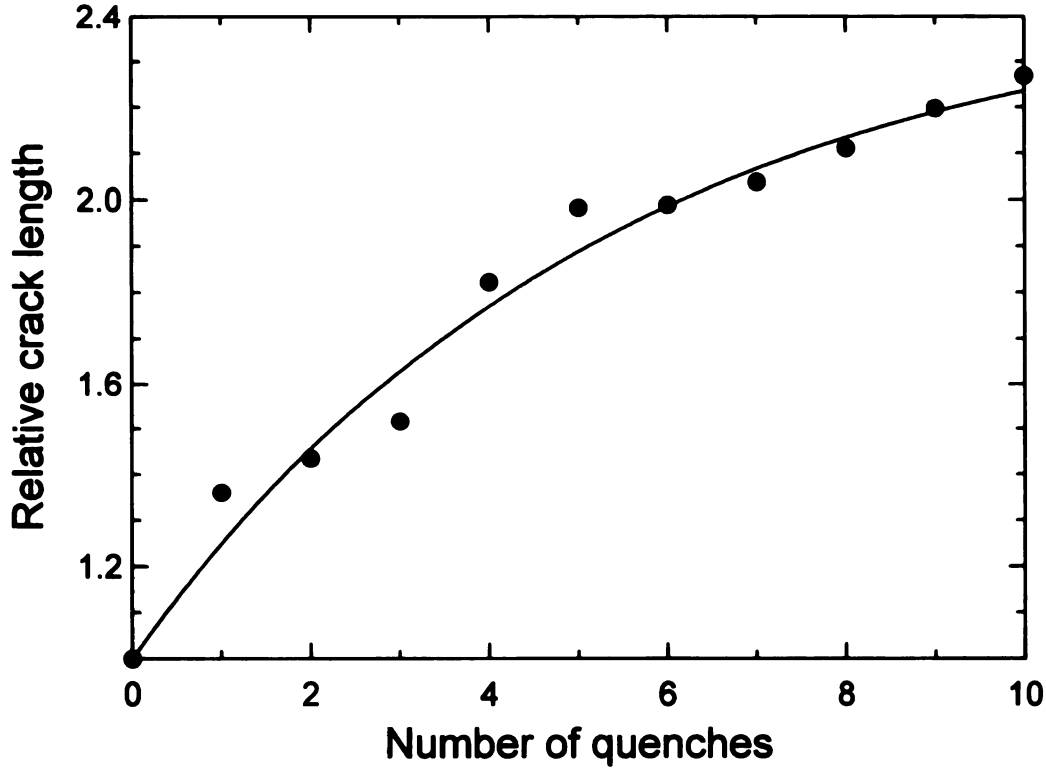

Figure 3.3.10. The crack growth behavior versus the cumulative number of thermal shock cycles a total of 10 thermal shock cycles, $\Delta T = 325\ ^{\circ}C$ (specimen A5-8). The solid line represents the least-squares fit to equation 3.3.1.

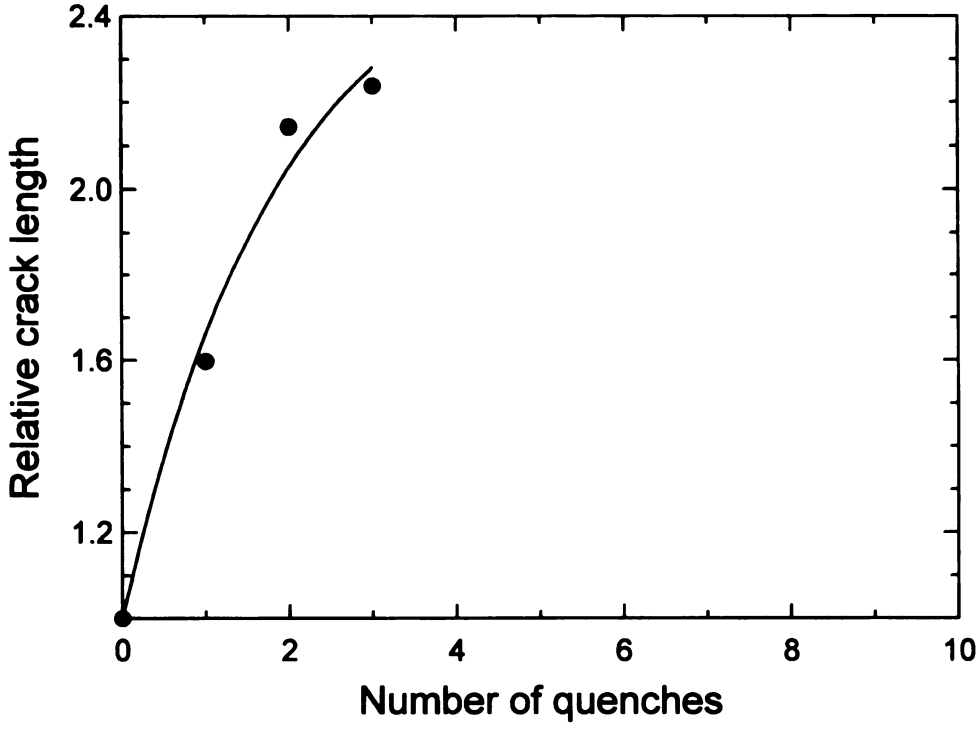

Figure 3.3.11 The crack growth behavior versus the cumulative number of thermal shock cycles a total of 3 thermal shock cycles, $\Delta T = 330\ ^{o}C$ (specimen A5-7). The solid line represents the least-squares fit to equation 3.3.1.

Table 3.3.1. The results of the least-squares fitting to equation 3.3.1 for the data of a total of 10 thermal cycles. (where c_0 = initial crack length, c_f = final crack length, N = data points).

Specimen	ΔT(°C)	c_0 (μm)	c_f (μm)	c_1(μm)	c_2(μm)	r*	N
A4-13	250	244.3	272.3	273.54	0.413	0.978	11
A4-14	270	256.6	293.1	316.12	0.101	0.946	11
A4-15	290	254.3	284.6	306.80	0.080	0.954	11
A6-2	295	251.4	513.7	542.54	0.260	0.973	11
A5-3	300	255.4	327.4	323.21	1.199	0.616	11
A5-12	305	242.3	537.1	638.52	0.157	0.954	11
A5-4	310	251.7	387.0	389.09	1.141	0.852	11
A5-11	315	244.3	538.3	538.69	0.566	0.989	11
A5-5	320	261.1	587.6	585.26	0.274	0.943	11
A5-8	325	247.3	561.2	607.73	0.188	0.979	11
A5-7	330	235.1	526.1	613.25	0.530	0.974	4

*** r = correlation coefficient**

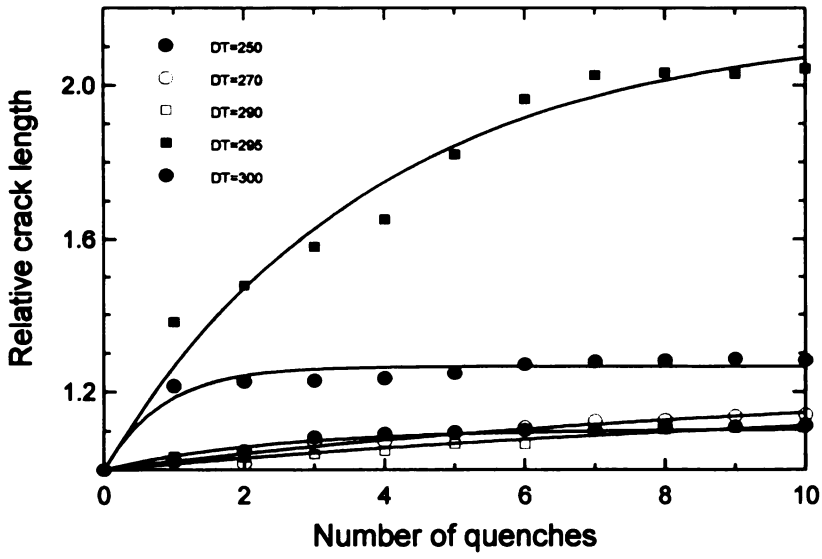

(a)

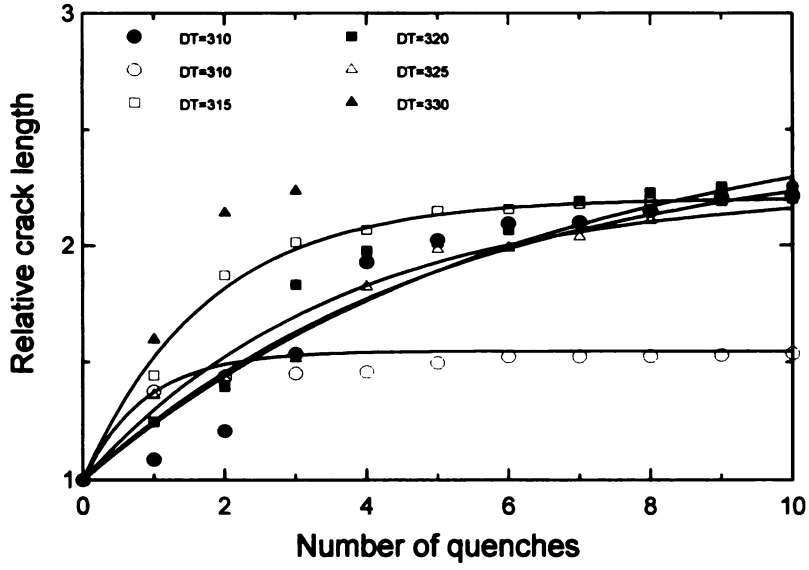

(b)

Figure 3.3.12 The crack growth behavior versus the cumulative number of thermal shock cycles for a total of 10 thermal shock cycles, The solid line represents the least-squares fit to equation 3.3.1. (a) 250 - 300 °C (b) 305-330 °C.

3. 3. 2. Thermal cycling to a maximum of twenty thermal shock cycles

To observe the crack growth and damage saturation behavior in more detail, the number of thermal shock cycles was increased to 20. Temperature differences were 250, 270 290, 295, 300, and 305 °C. The crack length data are given appendix D. The data of crack length also were least-squares fit to equation 3.3.1. The results are given in Table 3.3.2. Figures 3.3.13 - 3.3.18 show the results of the crack propagation behavior for each temperature difference. The solid lines in figures were obtained from the least-squares fit.

The crack growth behavior also showed crack length saturation. For specimens thermally shocked for 20 cycles, the saturated crack length ranged 264.35 μm to 546.7 μm. The correlation coefficient ranged from 0.804 up to 0.988. All specimens except A5-14 (ΔT =300) had a correlation coefficient greater than 0.931. Specimen A5-14 was different from the other specimens in that abrupt crack growth occurred on the 10th quench for this specimen.

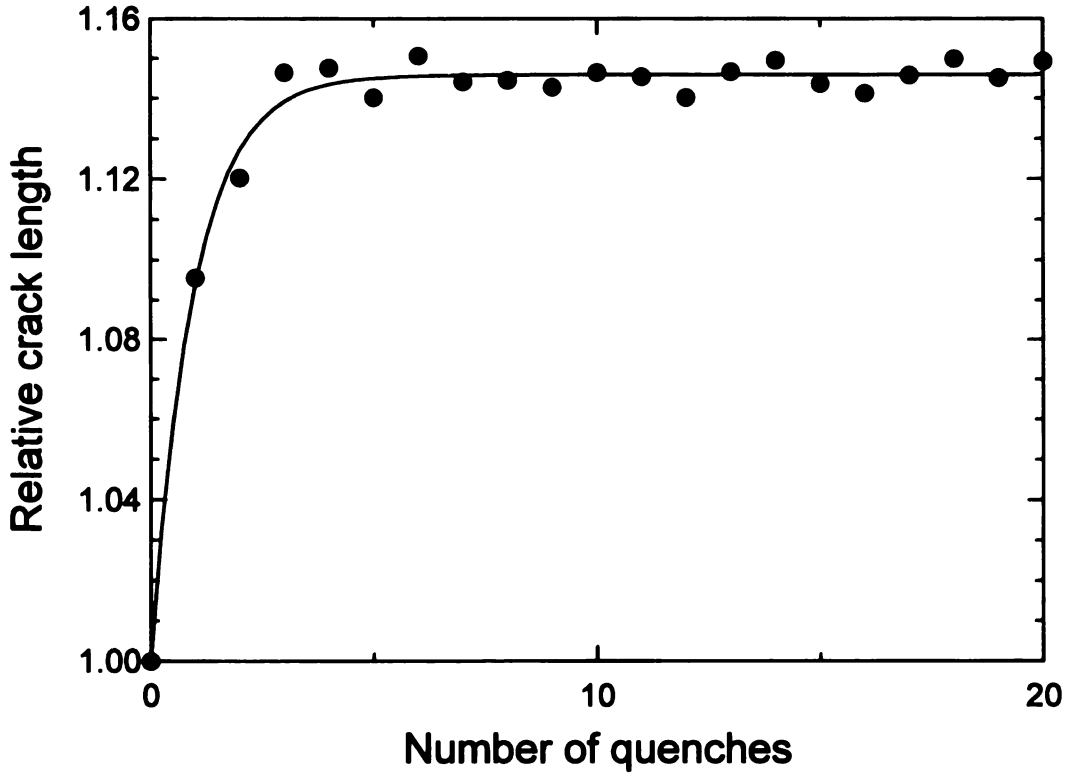

Figure 3.3.13. The crack propagation behavior versus the cumulative number for a total of thermal shock cycles, $\Delta T = 250\ ^{o}C$ (specimen A6-3). The solid line represents the least-squares fit to equation 3.3.1.

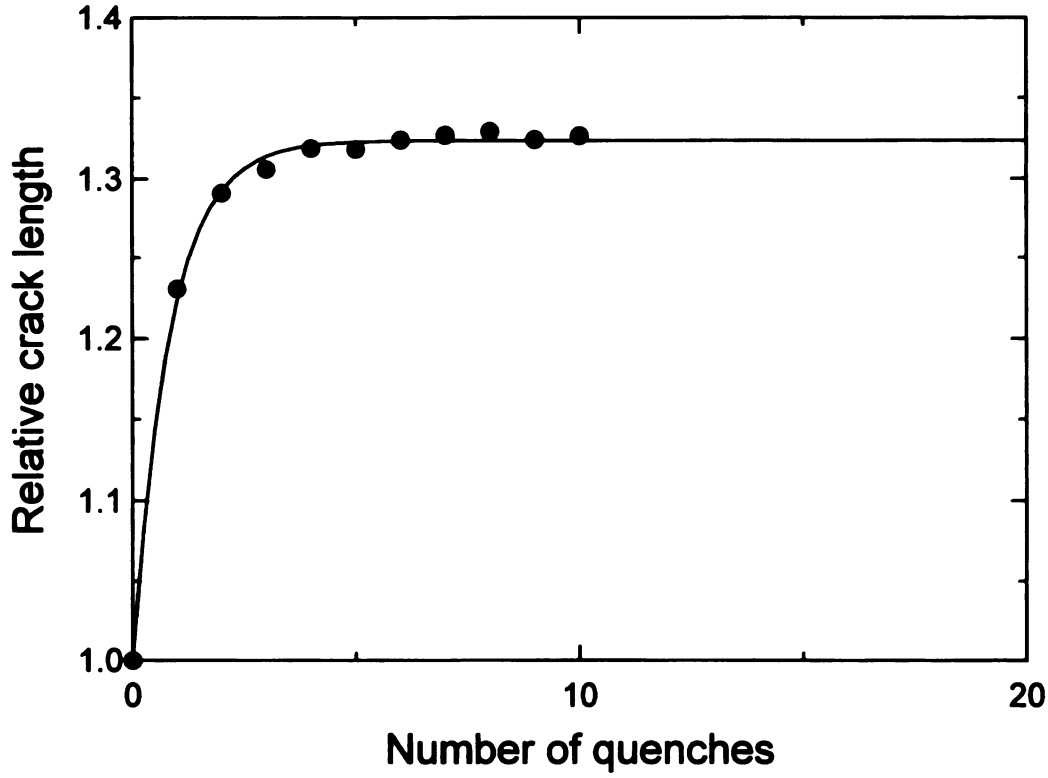

Figure 3.3.14. The crack propagation behavior versus the cumulative number for a total of thermal shock cycles, $\Delta T = 270\ ^{o}C$ (specimen A6-4). The solid line represents the least-squares fit to equation 3.3.1.

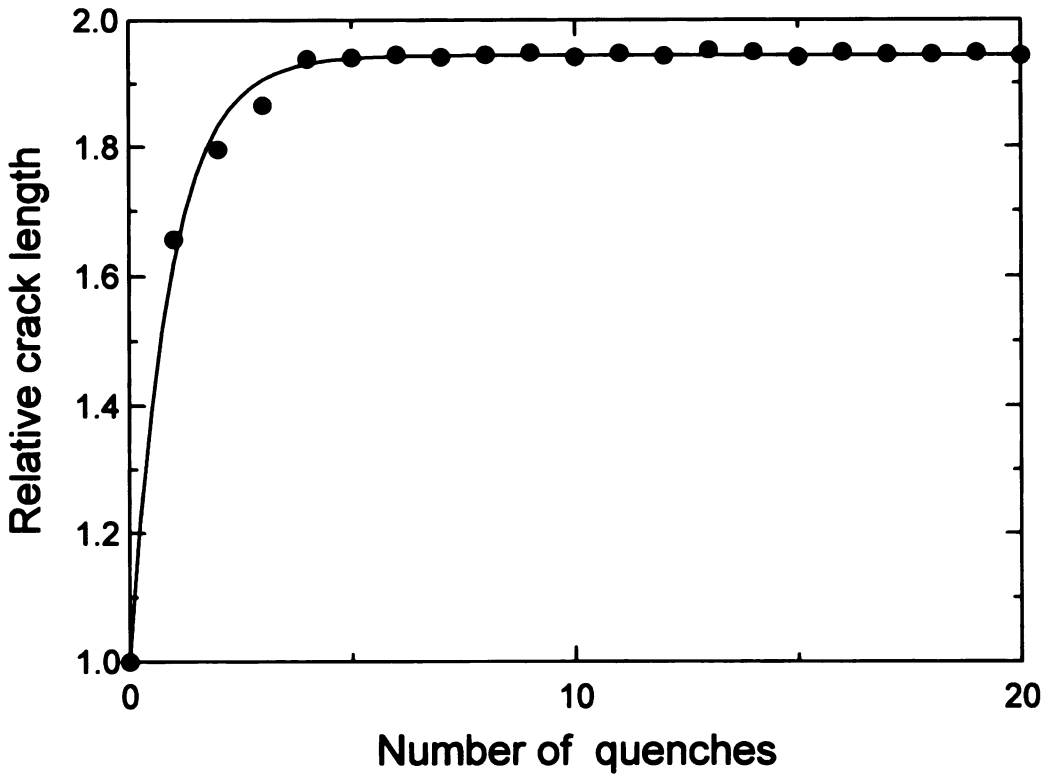

Figure 3.3.15. The crack propagation behavior versus the cumulative number for a total of thermal shock cycles, $\Delta T = 290\ ^{o}C$ (specimen B1-5). The solid line represents the least-squares fit to equation 3.3.1.

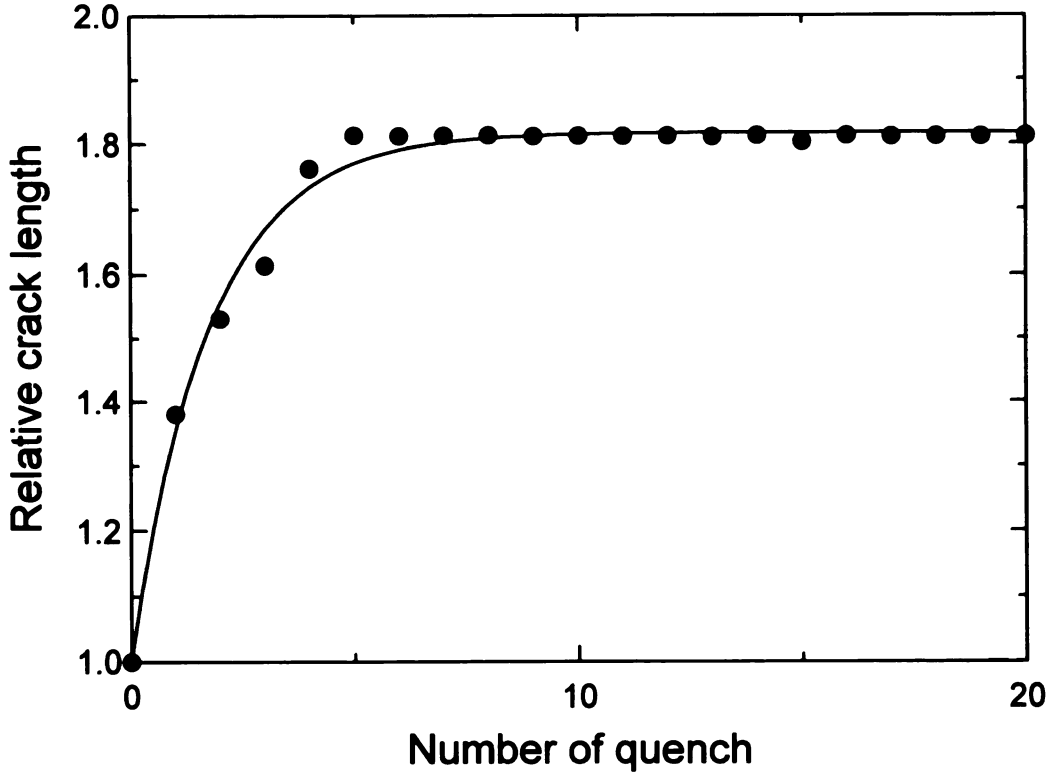

Figure 3.3.16. The crack propagation behavior versus the cumulative number for a total of thermal shock cycles, $\Delta T = 295\ ^{\circ}C$ (specimen A5-10). The solid line represents the least-squares fit to equation 3.3.1.

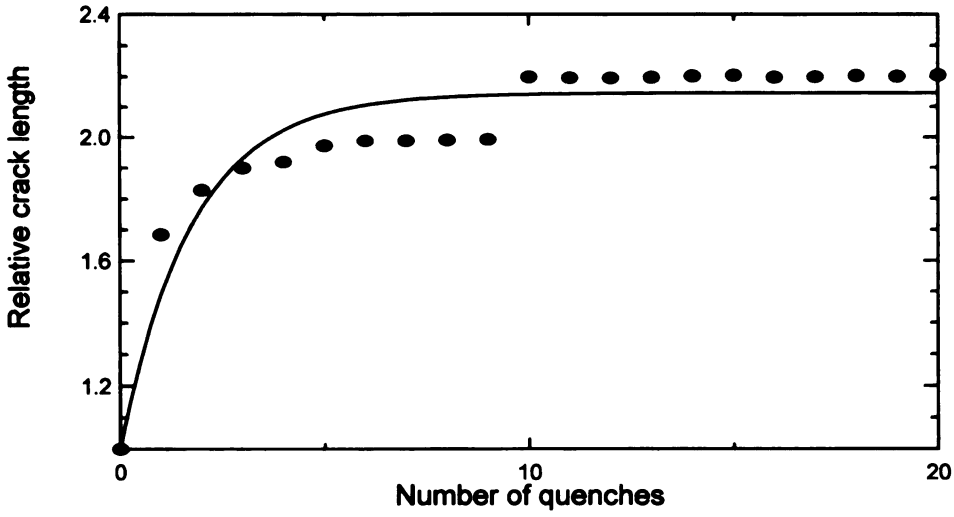

(a)

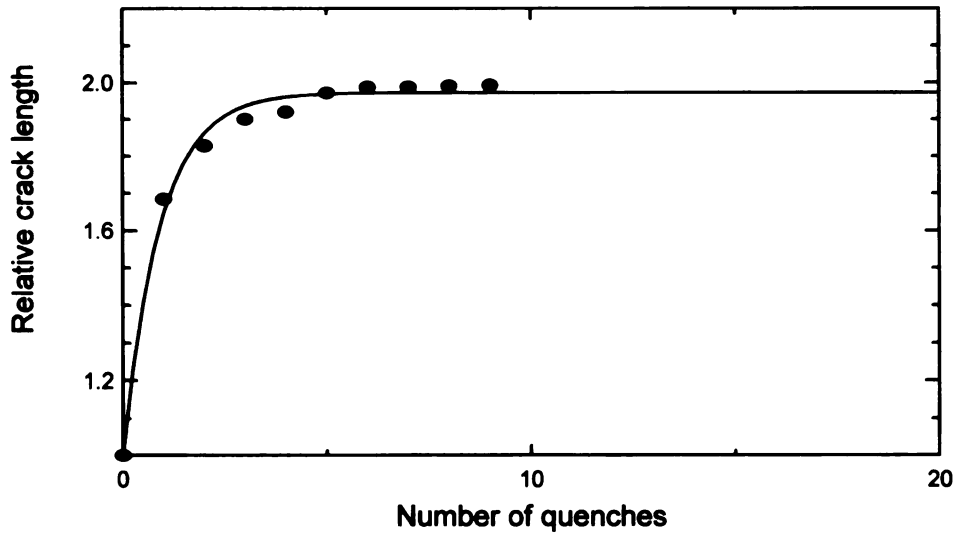

(b)

Figure 3.3.17. The crack propagation behavior versus the cumulative number for a total of thermal shock cycles, (a) $\Delta T = 300\ ^{\circ}C$ (specimen A5-10) (b) without abrupt increase in crack length at 10th thermal quenching. The solid line represents the least-squares fit to equation 3.3.1.

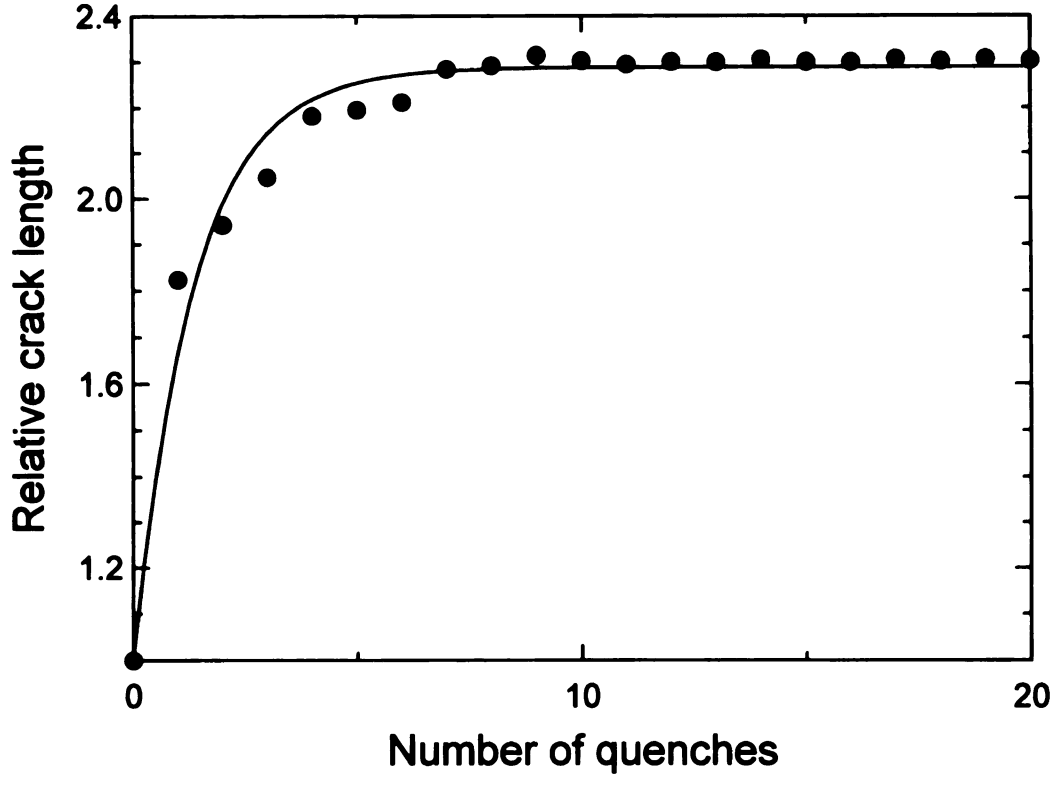

Figure 3.3.18. The crack propagation behavior versus the cumulative number for a total of thermal shock cycles, $\Delta T = 305\ ^{\circ}C$ (specimen A6-1). The solid line represents the least-squares fit to equation 3.3.1.

Table 3.3.2. The least-squares fitting of equation 3.3.1 for 20 quench specimens (where a_0 = initial crack length, a_f = final crack length, N = data points).

Specimen	ΔT(°C)	a_0 (μm)	a_f (μm)	c_1	c_2	r	N
A6-3	250	230.7	265.15	264.35	1.03	0.952	21
A6-4	270	249.7	331.3	330.56	1.17	0.988	11
B1-5	290	227.6	442.4	442.45	1.07	0.976	21
A5-10	295	230.8	418.4	419.42	0.57	0.984	21
A5-14	300	244.1	538.4	523.76	0.56	0.804	21
A6-1	305	237.3	546.7	543.06	0.73	0.931	21

r* correlation coefficient

N is the number of data points for the least-squares fit. N includes the measurement of the crack length 24 hours after indentation and the crack lengths measured following each of N-1 thermal cycles.

The crack propagation behavior for the thermal fatigue is given as a function of quench temperature difference in Figure 3.4.19. The crack lengths increase as the number of quenches, eventually the crack lengths saturate.

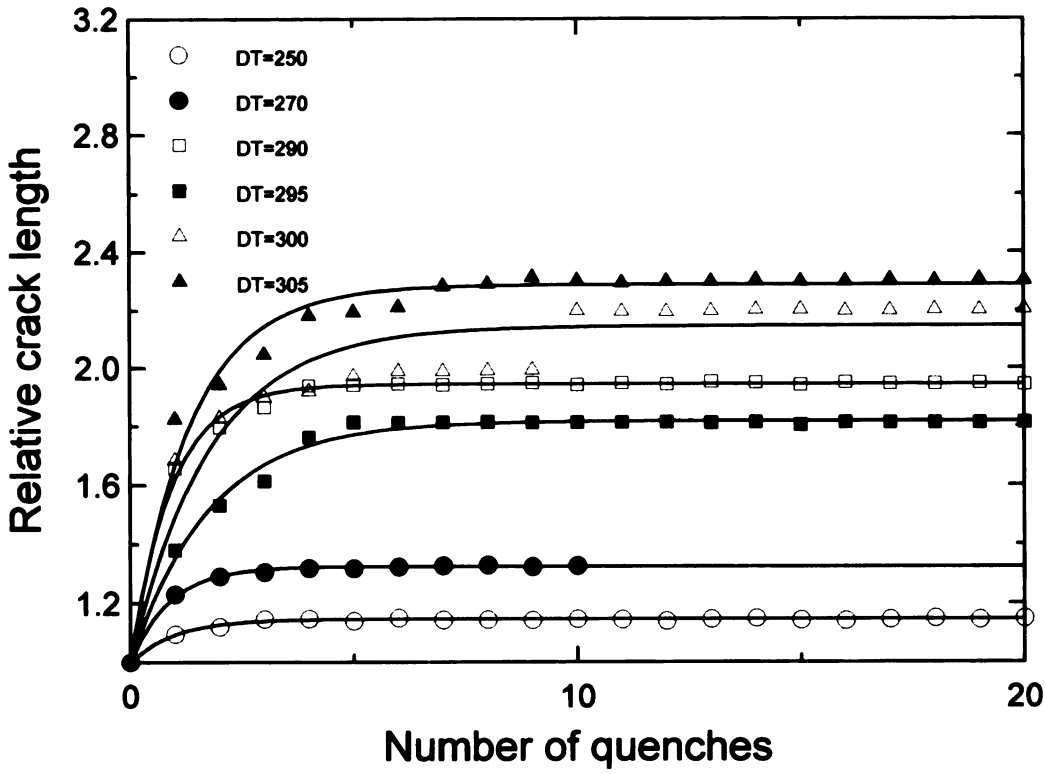

Figure 3.3.19. The crack propagation behavior versus the cumulative number for a total of thermal shock cycles with quenching temperature difference range of 250 °C to 305 °C. The solid line represents a least-squares fit to equation 3.3.1.

3.3.3. The comparison of rate constant with Lee's data [12] and Ash's data [32]

The rate constant (b for this study and Ash's work [32], and α for Lee's work [12]) in equation 3.3.1 is related to quenching temperature difference. The data were obtained by measuring crack lengths in this study and in Ash's work [32], while Young's modulus was measured for Lee's work [12]. The calculated values of rate constant from least-squares fit to equation 3.3.1 were plotted (Figure 3.3.20).

The rate constant increased as the quenching temperature difference increased. However, rate constants for 20 quenched specimens were very scattered (Figure 3.4.21). The solid curves in Figure 3.3.20 were obtained from linear regression using a PLOT-IT program (Scientific Programming Enterprise). The correlation coefficient for Young's modulus data was 0.975 but the Ash's and our coefficients were poor (Table 3.4.1). The difference in the scatter could stem from the fact that the Young's modulus measurements represent the effect of an ensemble average for an entire microcrack population in a thermally shocked (not indented) specimen. In contrast to the Young's modulus measurements by Lee [12], this study relied on a single Vickers indentation crack system to assess the state of thermal shock damage.

Table 3.3.3. The comparison of rate constants for data of Young's modulus (Lee's Work [12]) and data of crack length (this study and Ash's work [32]) for unreinforced alumina specimen.

	slope	intercept	correlation coefficient	data points
3b for this study (10 quenches)	0.017	-4.52	0.637	11
α for Lee's data	0.012	-2.90	0.975	5
3b for Ash's data	0.015	-2.78	0.578	6

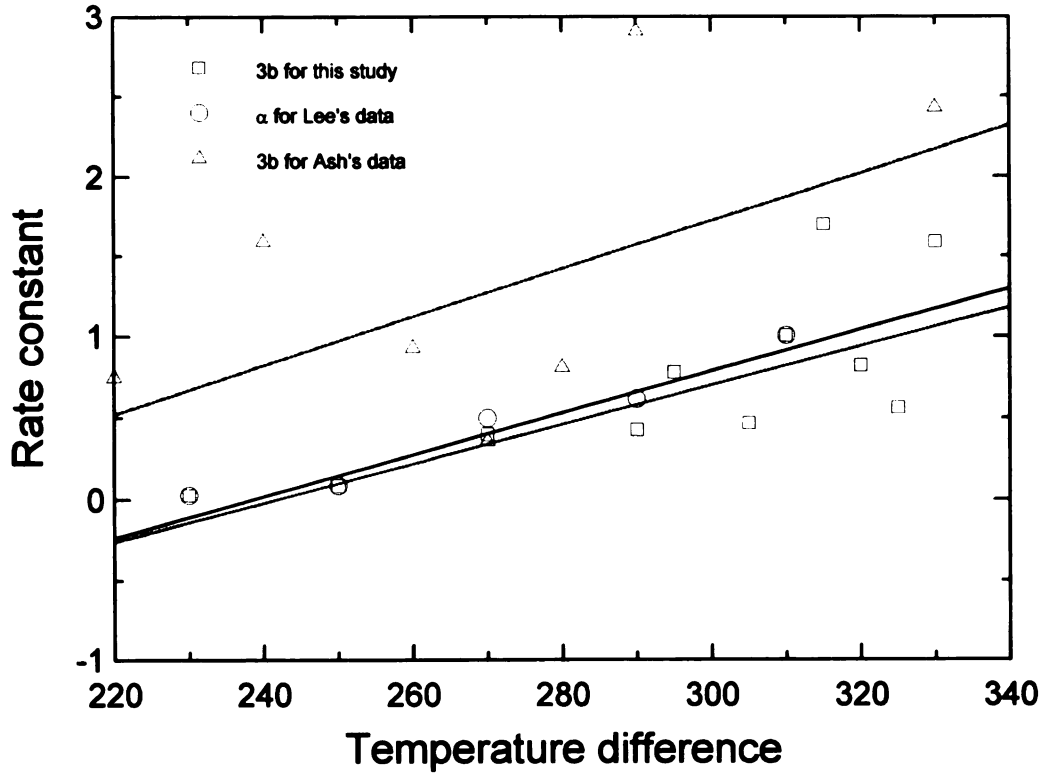

Figure 3.3.20. Comparison of rate constants as a function of quench temperature difference for three thermal fatigue studies: this study and Ash's work [32] and Young's modulus data (Lee's work [12]). Each of these three studies involved the thermal fatigue of unreinforced polycrystalline alumina into room temperature deionized water. The solid line was obtained from linear regression of data for this study, dotted line represents linear regression for Lee's data and double dotted line is a linear regression of Ash's data using PLOT IT program.

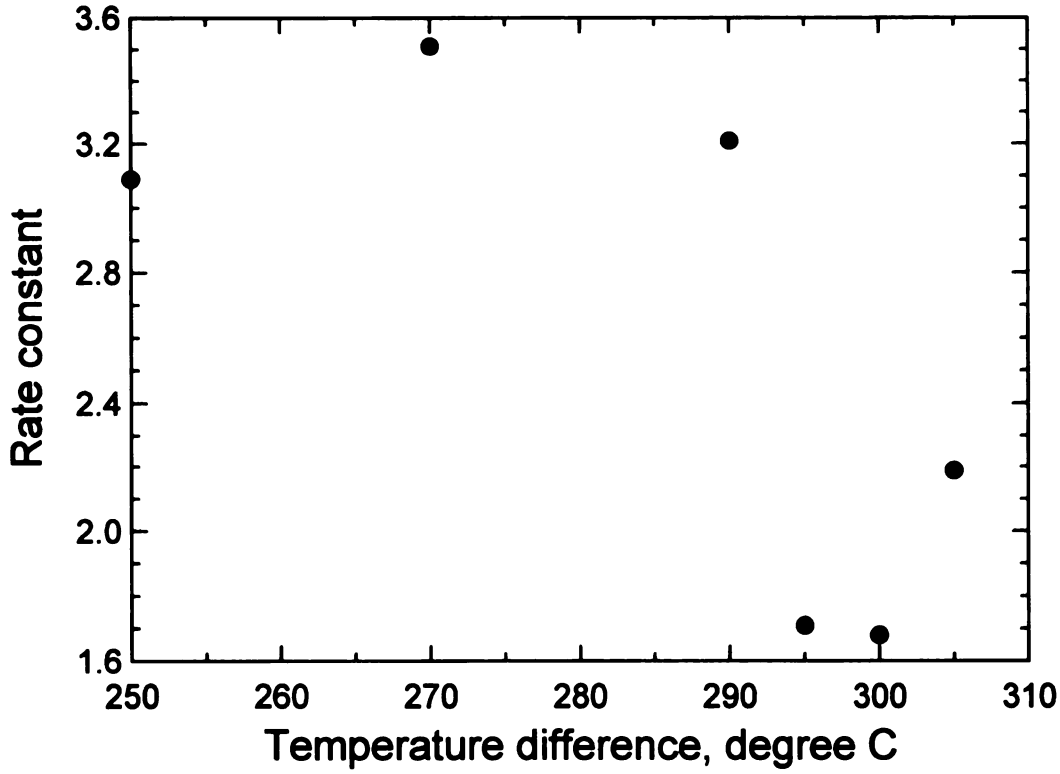

Figure 3.4.21 Rate constants (3b) behavior for 20 quenches as ΔT increases for unreinforced alumina specimen. The quenching medium is deionized water.

3.3.4. The severity of thermal fatigue damage as a function of the quench temperature difference

The severity of thermal shock damage due to an increase in the quench temperature difference was estimated by calculating a normalized saturation crack length for each quench temperature difference. The normalized saturation crack length was defined as saturation crack length/initial crack length.

The saturation crack length increased as the quench temperature difference increased (Figure 3.5.1). The solid lines in Figure 3.5.1 were obtained by linear regression using the PLOT-IT program (Scientific Programming Enterprise) and the results are given Table 3.5.1. The slopes of normalized saturation crack length versus quench temperature difference showed good agreement with all specimens. The correlation coefficients for the specimens quenched 20 times were very good. The scatter in the data may be related to the geometry of specimen, the initial flaw distribution, and the size of the flaws. Therefore, the thermal fatigue damage is more severe as the quench temperature difference increases.

Table 3.3.4. The results of linear regression of normalized saturation crack length for unreinforced polycrystalline alumina specimen using PLOT-IT program.

	Intercept	Slope	Correlation coefficient	Data points
for 10 quench	-4.92	0.019	0.76	11
for 20 quench	-5.03	0.020	0.96	5
for 5 quench*	-3.28	0.017	0.66	6

* Ash's data [32]

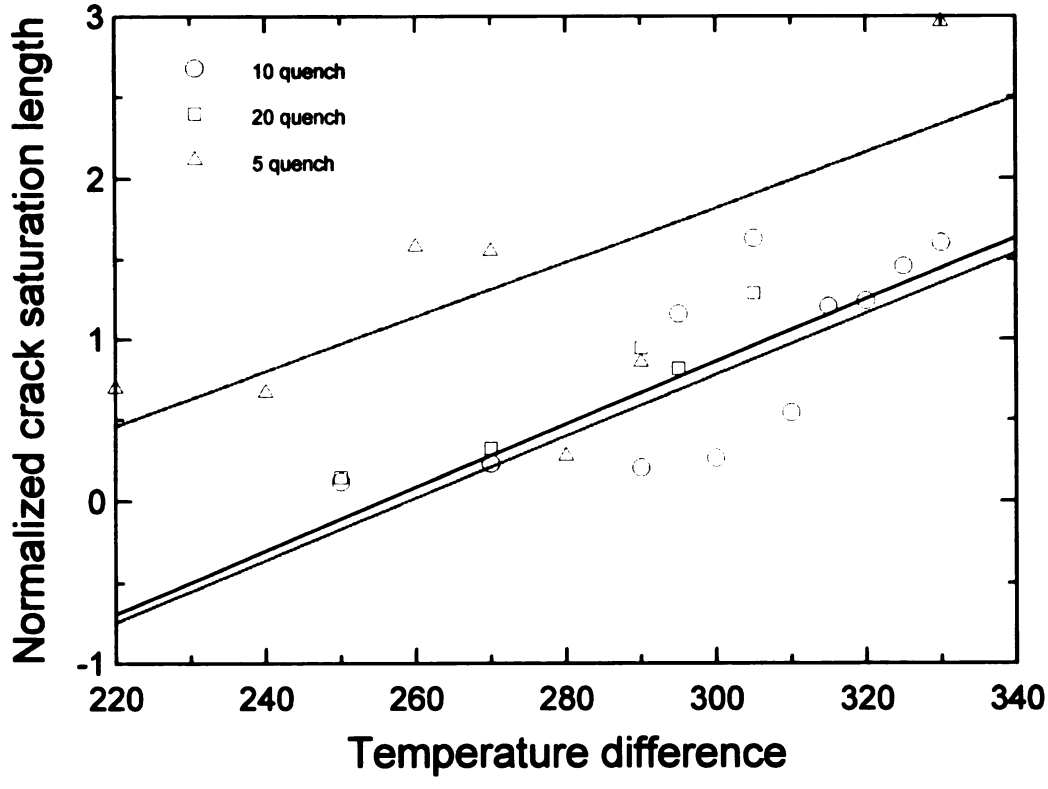

Figure 3.3.22 Normalized saturation crack length behavior versus quench temperature difference for polycrystalline alumina specimens. The solid line (10 quenches), dotted line (20 quenches), and double dotted line (5 quenches [32]) represent a linear regression of the data using PLOT IT program.

3.3.5. Comparison of crack lengths for a given Vickers crack subject to thermal fatigue

Using a 49 N load, three Vickers indentation crack systems were introduced into the long transverse face of a unreinforced alumina specimen (9.1 mm × 56.3 mm × 0.96 mm). The quench temperature difference was 260 °C (see section 2 for details of the experimental procedure.). The longitudinal (x-direction) crack length and vertical (y-direction) crack length show a slight directional difference in crack growth (Figure 3.3.20 and Appendix D) during thermal shock testing.

The crack grew more in the y-direction than in the x-direction thus the crack propagation was affected by the crack orientation. The ratio of the crack lengths in the x-direction and y-direction increased to 1.22 as the thermal shock cycles increased. After about 3 to 4 thermal shock cycles, the crack length seemed to saturate.

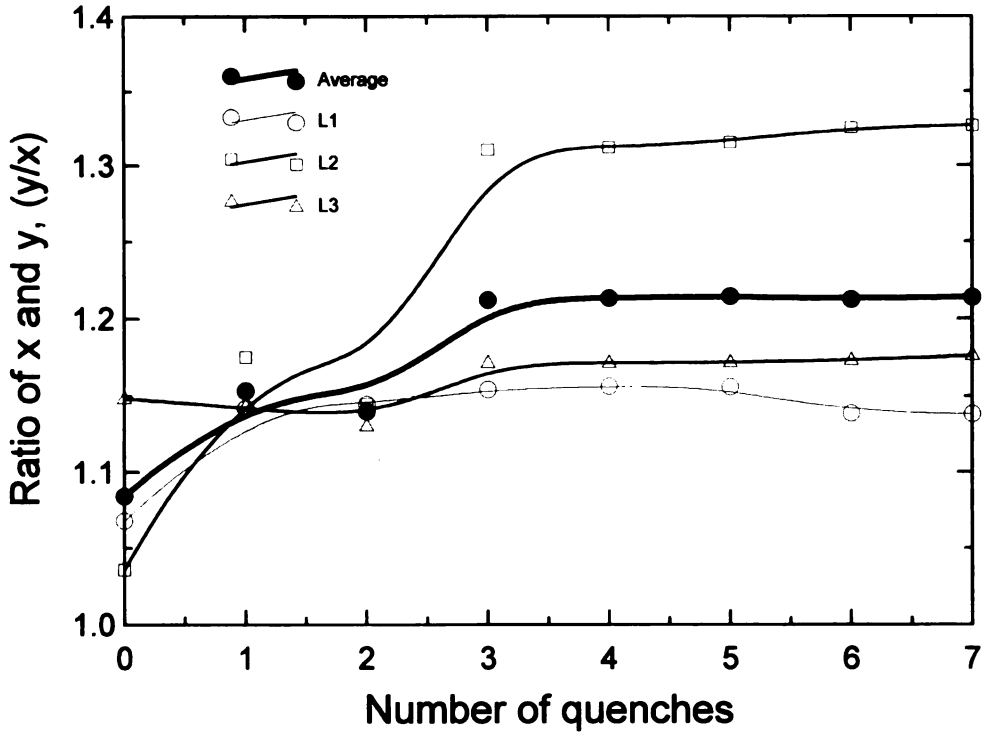

Figure 3.3.23. The crack propagation behavior of bar-shaped specimen of alumina under cyclic thermal shock testing. L1, L2, and L3 represent the position of indentation crack (see section 2.7).

3.4. Grain bridging in the brittle materials

3.4.1. An overview of grain bridging

Studies of toughening mechanisms in monophase ceramic materials such as alumina have shown that a major toughening mechanism is grain bridging [33-47] including crack deflection [33,41] and crack bowing [35]. Grain bridging is observed behind crack tips [33-38].

Grain bridging is affected by the grain size and crack opening displacement. More bridging sites exist in coarse grained specimens than in fine grain sized specimens [34,38]. In grain bridging, there is a critical crack opening displacement related to grain size. Steinbech *et al.* [43] observed bridging for crack opening displacements less than 1/4 of mean grain size and Hay *et al.* [35] observed bridging for crack opening displacements 1/3 of mean grain size. The crack closure stress tends to be a function of crack opening displacement rather than a function of crack length in a bridging toughened material [38-40]. In addition, the frictional coefficient affects the grain bridging toughening; the crack closure forces increase as the frictional coefficient increases [33].

Scanning electron microscope observations provide evidence of grain bridging behind crack tip [34,36,37,41]. Stress-induced microcracking in the wake zone also can impede crack propagation. Typically, for polycrystalline alumina specimens there is no evidence of dispersed microcracking near the crack tip by scanning electron microscope observation. Thus it has been conjectured that stress- induced microcracking near the tip of a macrocrack is not available in monophase polycrystalline alumina [36,41].

3.4.2. Grain bridging model

Chou *et al.* [41] suggested a model for the evolution of grain bridging as toughening mechanism in a SiC platelet alumina composite. Crack deflection occurs and crack bridging or sliding pullout follows. Chou *et al.* [41] observed the crack deflection and grain bridging with a scanning electron microscope (SEM).

Figure 3.4.1 is a schematic diagram of the toughening mechanism in SiC platelet reinforced alumina. Kawasawa [33] suggested a similar grain bridging model (crack deflection and crack bridging) as a toughening mechanism for polycrystalline alumina. Crack bridging as the toughening mechanism of monophase ceramic material is composed of crack deflection and grain bridging. Bridging sites in turn can be degraded by cyclic loading [34,37].

3.4.3.1. The effect and observation of grain bridging by Lathabai *et al.* [34]

Lathabai *et al.* [34] investigated the effect of grain bridging using commercial alumina specimens with an average grain size of 23 to 35 μm. Disc shaped specimens 22 mm in diameter and 2 mm thickness used for tension-tension cyclic testing. Plate specimens 100 mm ×100 mm × 6 mm were used for a long crack test. Vickers indentation cracks were introduced with a 30 N load (short crack test) and a 50 N load (long crack test).

In the short crack test, specimens were loaded sinusoidally with a maximum tensile stress of 100 to 130 MPa keeping the minimum tensile stress at 20 MPa with frequency of 1 Hz

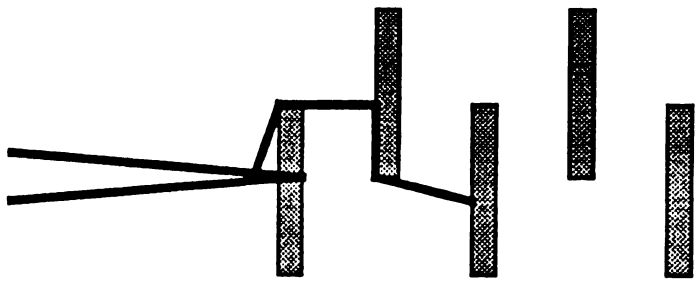

(a)

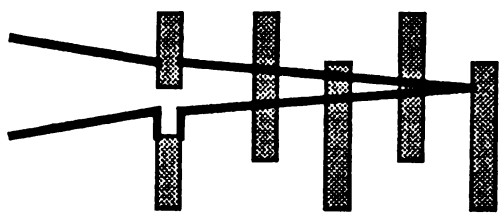

(b)

Figure 3.4.1. Schematic diagrams of a possible evolution of bridging (a) crack deflection (b) crack bridging for a SiC platelet composite specimen [41].

and 100 Hz using electro-servo-hydraulic machine. Lathabai *et al.* measured lifetime (time to failure) under cyclic tensile loading. Table 3.4.1 shows the maximum stress and lifetime.

Table 3.4.1. Lifetime under cyclic loading of alumina for 1 Hz and 100 Hz. A Vickers indentation crack was inserted with 30 N load [34].

Frequency, Hz	Largest of maximum cyclic stress, MPa	lowest of maximum cyclic stress, MPa	Largest lifetime, seconds	lowest lifetime, seconds	N (specimens)
1	130	110	*	10	16
100	130	100	10^5	2	28

* Fracture did not occur within 24 to 40 hours.

Long crack testing was done using electro-servo-hydraulic machine with stress ratio 0.1 with frequency 10 Hz for two alumina compact tension specimens. Toughness increased as crack propagated. The fracture toughness was 4.0 $MPam^{1/2}$ at a crack extension of 0.9 mm. The fracture toughness was 5.3 $MPam^{1/2}$ at a crack extension 7 mm. Toughness saturated at 5.3 $MPam^{1/2}$. Grain bridging sites were observed in-situ using a scanning electron microscope (SEM) during cyclic loading test. Scanning electron microscopy (SEM) indicated an evolution of grain bridging behind the crack tip during cyclic loading. Table 3.4.2 summaries the scanning electron microscope observation. The evidence of the degradation of the grain bridging was the "cumulation of wear debris" under cyclic loading conditions. Thus frictional traction at sliding grain bridging facets gradually was reduced by the contacting grains repeatedly sliding back and forth, resulting in a degradation of specimen toughness.

Table 3.4.2. Scanning electron microscope in situ observation of crack for alumina specimen under cyclic load [34].

Magnification	Position of observation	Observation
× 1000	behind crack tip	grain bridging
× 6500	near dislodgment of grain	grain bridging
× 5000	*	crack paths
× 7500	*	crack paths
× 5000	*	crack paths

* not available

3.4.3.2 The effect and observation of grain bridging by Hay *et al.* [35]

Hay *et al.* [35] used 99.7% alumina (fabricated by Johnson Matthey, Alpha Alumina A123) which were cut into 8.90 mm × 60 mm × 4 mm specimens to observe grain bridging effects in monophase ceramic materials. The mean grain size of alumina was about 16 μm.

Post fracture tensile (PSF) testing was performed on a modified four point bend test in which a second notch is inserted at rear of specimen (Figure 3.4.2). Post fracture tensile testing identified the critical stress and stress distribution in the wake region of the alumina specimen since there is no crack-resisting material in front of the crack tip when crack tip enters second notch at rear of specimen. The results of post fracture test, stress-displacement behavior, showed that the strength increased from 2.7 MPa to 5.6 MPa as

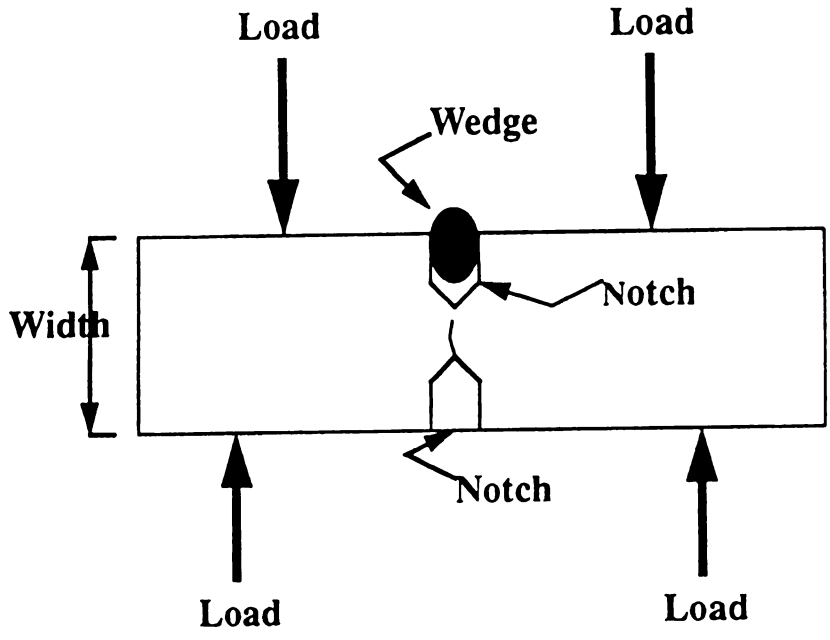

Figure 3.4.2. Schematic diagram of modified four point bend test specimen of polycrystalline alumina for postfracture tensile test [35].

the crack opening displacement increased from 5 μm to about 7.6 μm (Table 3.4.3). Strength monotonically decreased with increasing crack opening displacement up to about 50 μm. At greater CODs, there was a loss of grain bridging associated drop in strength (Table 3.4.3).

Table 3.4.3. The stress behavior versus displacement of polycrystalline alumina specimen by postfracture test [35].

	First measurement of stress and displacement	Maximum stress and displacement	Last measurement of stress and displacement
1	3.2 MPa at 3 μm	8.4 MPa at 5 μm	0.1 MPa at 47 μm
2	3.7 MPa at 3.5 μm	7.6 MPa at 6 μm	0.1 MPa at 28 μm
3	3.1 MPa at 5 μm	5.8 MPa at 7 μm	0.1 MPa at 37 μm
4	2.3 MPa at 6 μm	4 MPa at 9 μm	0.1 MPa at 48 μm
5	1.3 MPa at 7.6 μm	2.1 MPa at 11 μm	0.1 MPa at 35 μm
Average	2.7 MPa at 5 μm	5.6 MPa at 7.6 μm	0.1 MPa at 39 μm

The grain bridging stress is a function of crack opening displacement and is expressed as follow [35]

$$\frac{\sigma}{\sigma_m} = (1 + \frac{u}{u_m})^n . \qquad (3.4.1)$$

where σ_m = critical stress for bridge rupture

u_m = critical crack opening displacement for bridge rupture

n = constant

In Hay *et al.*'s experiments, bridging in alumina became insignificant at crack opening displacement of 1/3 of the grain size. Steinbresh *et al.* [43] observed significant grain bridging at COD of less than 1/4 of the grain size. The monotonic decrease in strength during the post fracture test is caused by the loss of bridging area.

Hay *et al.* [35] compared the COD criterion of polycrystalline alumina (COD's of about 1/3 of grain size) with monolithic $MgAl_2O_3$ spinel. Three specimens of monolithic $MgAl_2O_3$ spinel were used for postfracture testing. For the spinel, the average grain size for small grain size specimen was 35 μm, 75 μm for intermediate grain size specimen, and 180 μm for large grain size specimen. For spinel specimens, grain bridging effects were significant at COD of less than 1/9 of the grain size. Hay *et al.* suggested that "Application of the COD-grain size criteria fitted to the alumina, was found to yield poor agreement with PFT result (for spinel)...[35]." Further, Hay *et al.* stated that "...Changing the COD-grain size ratio from 1/3 to 1/9 implies that the load transfer mechanism are less effective in the spinel than in the alumina and that the geometric aspects of the microstructure, namely the size, size distribution, and spatial arrangement of grains, do not uniquely control the wake load character. Rather, there may exist a universal geometry factor which describes the effects from these geometric components but is independent of the material properties. The geometric description may require further modification to account for the various material-specific contributions, such as thermal expansion anisotropy. The much larger limiting COD (a critical COD for bridge rupture) at the wake extreme characteristic of alumina probably results primarily from the residual

thermoelastic stresses, which promote a more effective load transfer for an equivalent grain interlocking distance. [35]"

3.4.3.3 The effect and observation of grain bridging by Kagawa [33]

Kagawa [33] modeled grain bridging in a material for which the crack first deflects along a grain boundary. Grain bridging follows when the deflection angle (angle between the path of crack and crack deflection) is between arctangent of the inverse of the half grain size and 90°. The Kagawa model assumes the crack bridging does not occur if the angle is less than arctangent of the inverse of half grain size. To examine the grain bridging process, a finite element method was used. The Kagawa model [33] assumes a grain size between 50-100 μm, a Poisson's ratio of 0.15 and grains that are either square or hexagonal. The MENTAT-MARC computer program solved for grain bridging under mode I loading condition (opening mode). The applied load used was less than maximum load required for crack propagation. Figure 3.4.3 shows the effect of the crack deflection angles upon the crack closure stress. At a crack deflection angle of 70°, crack closure stress gradually increased as crack separation increased since relative sliding occurred between contacting grains as the applied loading increased. Normalized distance (Figure 3.4.3) is the ratio of crack separation and half the grain size.

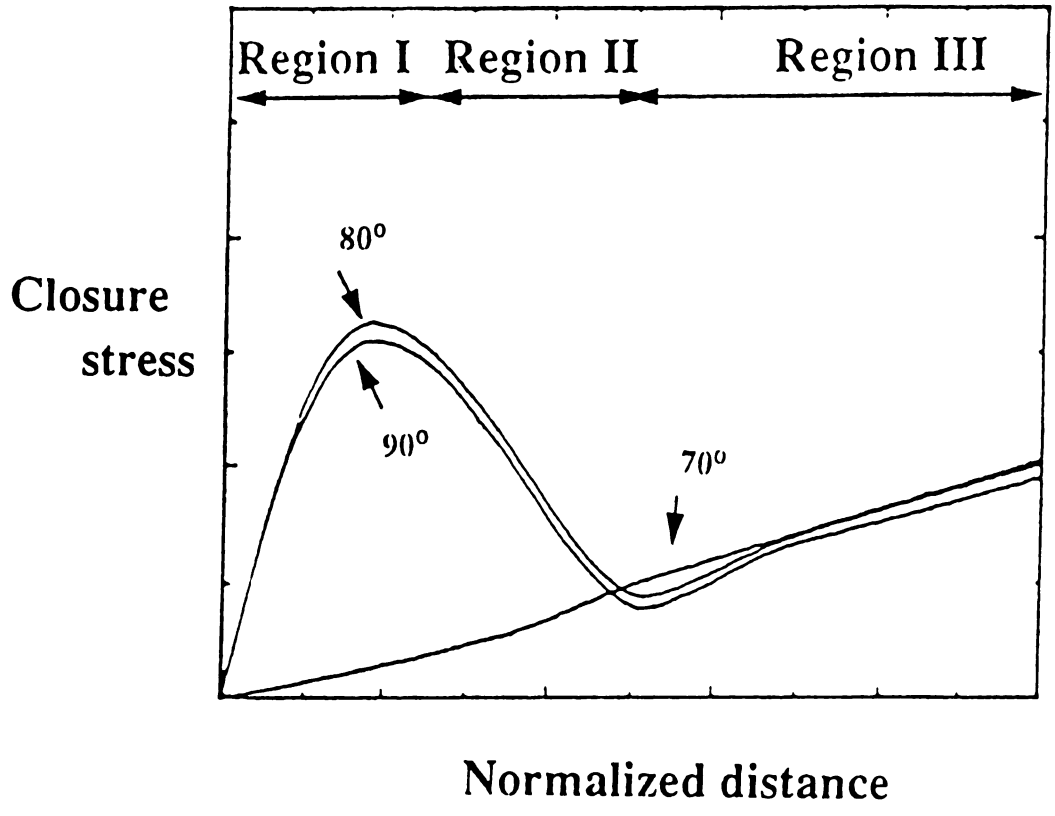

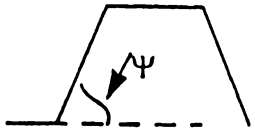

ψ = **Crack deflection angle**

Figure 3.4.3. The crack closure stress behavior with increasing normalized distance where normalized distance is the ratio of the crack separation to half of grain size. The closure stress versus normalized distance curve shown here was generated by an FEM program [33]. The definition of the crack deflection angle ψ is shown the above.

The crack closure stress for grain bridging behavior as a function of crack separation is divided into three regions. In the first region, the stress increases as separation increases to normalized crack ratio of about 0.1 (crack separation/half of grain size) due to interlocking of the grain faces. The second region shows a gradual decrease of crack closure stress with increasing crack separation by virtue of rupture of the interlocked grains. The third region involves a smooth increase of crack closure stress due to relative sliding at contacted grains. Kagawa suggested that crack closure stress versus normalized crack displacement curve indicates that the first region (involving interlocking grains) is a major process in toughening ceramic materials via grain bridging.

Kagawa [33] also calculated that the crack closure stress is a function of grain size using an FEM program. The stress increased as grain size decreased. Larger elastic deformation near grain bridging sites was observed for specimens with lower Young's moduli (190 and 380 GPa) compared to specimens with higher Young's moduli (570 GPa). However, the maximum crack closure stress is not affected by Young's modulus (Table 3.4.4). The friction coefficient affects third region where the crack closure stress increases with increasing crack separation, however, the coefficient of friction is neglected in the first and second region.

Table 3.4.4. The effect of grain size and Young's modulus on crack closure stress for ceramic materials using an FEM program [33].

ψ = 80, E = 570 GPa		ψ = 80, Grain size = 60 μm		
Grain size, (μm)	Maximum closure stress, (MPa)	E, (GPa)	Maximum closure stress, (MPa)	Normalized crack separation at Max. Closure stress
60	17	190	15.7	0.006
80	14.6	380	15.7	0.009
100	12.5	570	15.7	0.019

*ψ = crack deflection angle, E = Young's modulus. The data were not obtained from experiment but were calculated via a FEM program [33].

In summary, Kagawa [33] suggested that grain bridging toughing is affected by grain size, Young's modulus, and the frictional coefficient.

3.4.3.4. The effect and observation of grain bridging by Swanson *et al.* [36]

Swanson *et al.* [36] investigated crack interface grain bridging as a toughening mechanism using alumina having an average grain size of 20 μm. The crack evolution was monitored with in-situ optical microscopy observation of mechanically loaded tapered double cantilever beam (12 mm edge length and 2 mm thickness) specimens. In-situ optical microscopy also followed crack evolution in disks under axial loading. The "active sites" in back of the crack tip were examined to observe the evolution (formation and fissure) of grain bridging. A series of six low magnification (× 100) micrographs showed crack bridging during crack propagation. The crack interface bridging and an

increasing number of grain bridging sites were observed. In the double cantilever experiment, discontinuous crack growth was observed.

To examine strength behavior using a controlled flaw test, Vickers indentation cracks were introduced at the center of a disk specimen (25 mm diameter and 2 mm thickness). Swanson *et al.* observed crack propagation from the initial loading until fracture. The crack growth was distinguished by a stabilized growth without catastrophic growth. The fracture proceeded mainly by an intergranular mode and showed also discontinuous evolution (crack deflection and grain bridging) behind crack tip as the case for the cantilever beam specimens.

Microcracking can be a source of resistance of crack growth near crack tip since the crack can be arrested by microcracks in the frontal zone of cracks. However, there is no evidence of extended frontal microcracking in front of crack tip, therefore, it was unlikely that microcracking affected the frontal zone of the crack. The crack evolution observed by optical microscopy, in both of the above experiments, gave evidences of grain bridging behind the crack tip which provided a mechanism to impede fracture. Observation of the crack evolution showed the crack grew stably and fractured without catastrophic crack growth.

3.4.3.5. The effect and observation of grain bridging by Kishimoto *et al.* [37]

Kishimoto *et al.* [37] observed crack growth behavior for polycrystalline alumina specimens (6 specimens for static loading test and 6 specimens for cyclic loading test)

having a mean grain size ranging from 1.0 μm to 19 μm in order to examine grain size effects on grain bridging.

Compact tension specimens (50 mm × 40 mm ×16 mm) were loaded in an electro-servo-hydraulic testing machine. Crack lengths were measured by an optical microscope. The static load ranged from 63 N to 630 N. Sinusoidal stress (stress ratio is 0.1) was used for cyclic loading, with a loading rate 2.0 N/s.

The stress intensity factor for crack growth was much higher in coarse grain sized specimen (3.5 $MPam^{1/2}$) than in fine grain sized specimen (2.3 $MPam^{1/2}$). The stress intensity factor showed a slight decrease just after cyclic loading because the bridging areas were, Kishimoto *et al.* explained, degraded by cyclic loading. The slope of the load-strain curve was slightly larger in coarse grain sized specimens than in fine grain sized specimens though Young's modulus for both specimens were the same. The difference in load-strain slope and in the stress intensity factor can be explained by grain bridging behind of crack tip. The grain bridging is more effective (as calculated by a finite element method [37]) in coarse grain sized specimens than fine grain size specimens. For a large grain size, the bridging site area through metallurgical microscope increased to about 175 mm^2 as crack length increased to 10 mm (Figure 3.4.4) while the bridging area rarely increased as the crack length increased. The grain size effect found by Kishimoto [37] agrees with the Kagawa's result [35].

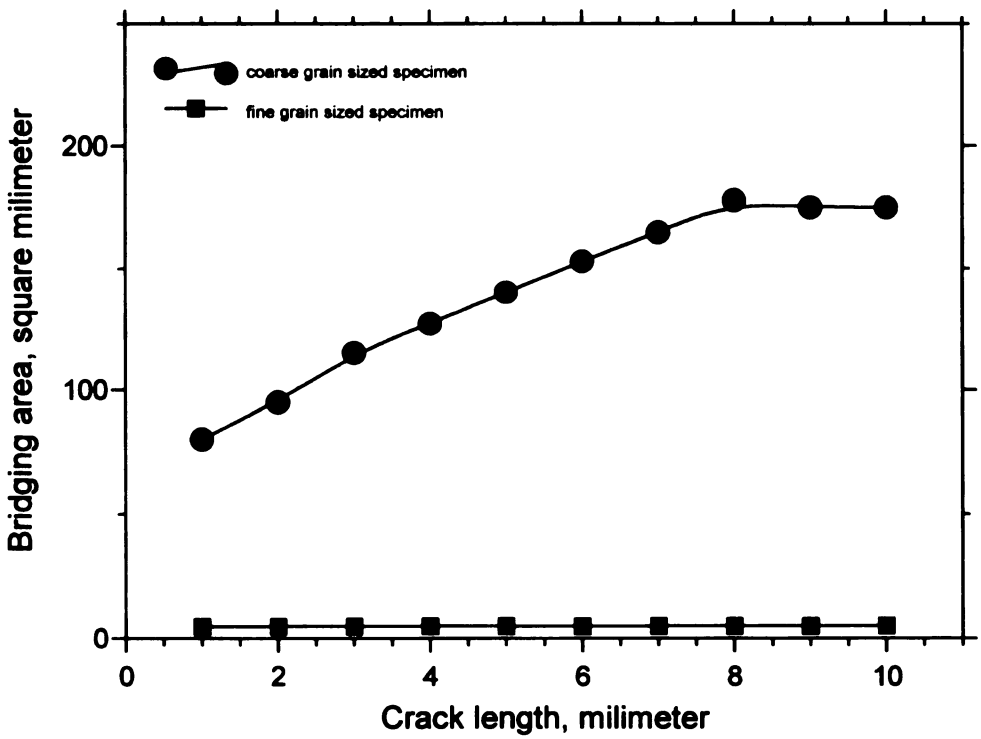

Figure 3.4.4. The change of bridging area for alumina specimen with increasing crack length as calculated by a finite element method by Kishimoto *et al.* [37].

3.4.3.6. The effect and observation of grain bridging by Dauskardt [38,39]

Dauskardt [38,39] examined grain bridging degradation under cyclic fatigue with two coarse grain sized alumina specimens (mean grain sizes of 8 μm and 13 μm). Using a 3 mm thick compact tension specimen, testing was done by ASTM standard fatigue crack growth procedure (ASTM, 1989) modified for ceramics (Figure 3.4.5 [46]). The load ratio (minimum/maximum load) was 0.1 with a frequency of 25 Hz. The crack propagation profile and grain bridging were examined by a scanning electron microscope.

In cyclic and monotonic loading, the grain bridging appeared behind the crack tip (as observed in SEM micrographs). The relation of crack opening displacement to bridging was investigated by measuring crack opening displacement under cyclic loading. The displacement for loading and unloading displayed a hysteresis curve, a schematic of which is shown in Figure 3.4.6.

Elastic grain bridging occurred initially during loading. Frictional bridging was followed after the grain pullout. The frictional sliding resistance decreased thus the stiffness decreased. For unloading, frictional bridging appears following the elastic grain bridging. However, the maximum crack opening displacement measured during the loading-unloading test was about 1.4 μm which is less than about 1/4 of grain size. The degradation of grain bridging under cyclic loading can be explained by repetitive sliding during frictional grain bridging.

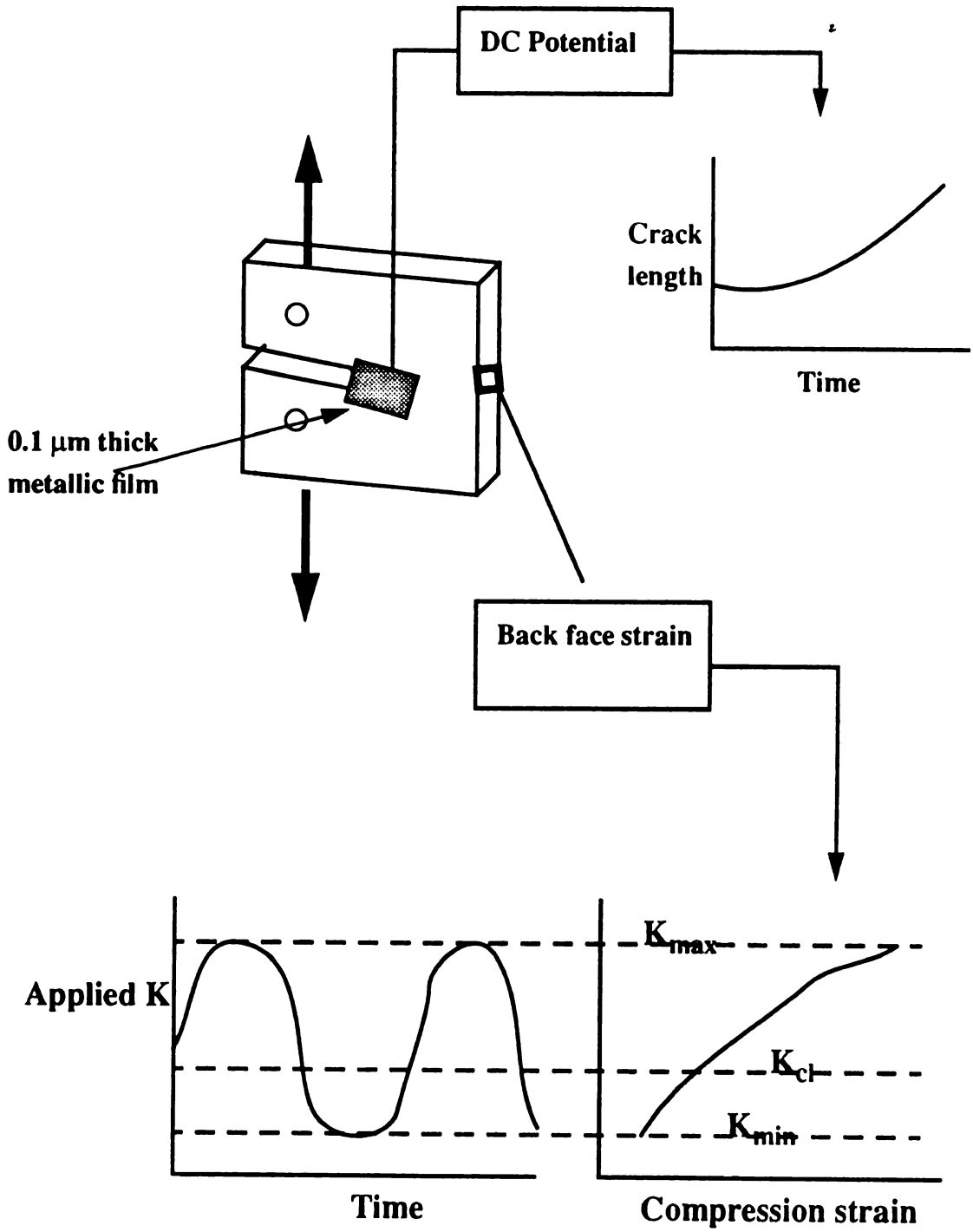

Figure 3.4.5. Experimental technique for observing crack length and stress intensity factor where K_{max} = maximum stress intensity factor, K_{cl} = crack closure stress intensity factor, and K_{min} = minimum intensity factor [48]. The specimens were alumina with grain sizes of 8 and 13 μm [38,39].

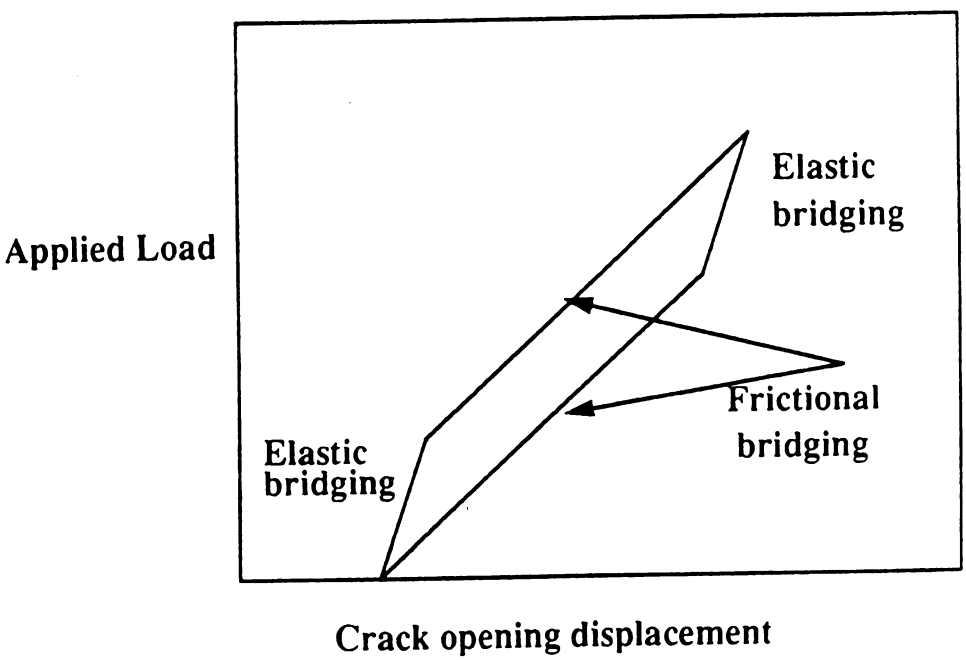

Figure 3.4.6. Hysteresis curve of applied load and crack opening displacement as suggested by Dauskardt [38,39].

3.4.3.7. The effect and observation of grain bridging by Vekinnis *et al.* [44]

Vekinnis *et al.* [42] tested in double torsion 96% alumina specimens which had a $MgO\text{-}CaO\text{-}Al_2O_3$ glass matrix (Coors ADS96R). The specimens were cut into 25 × 55 × 0.64 mm from plates. Seven specimens with an average grain size of 7 μm were loaded in a double-torsion jig mounted in scanning electron microscope (SEM).

The energy release rate increased from 41.7 to 77.1 J/m^2 with increasing crack length. The energy release rate saturated after cracks grew to about 8.8 mm and the saturation value increased with increasing grain size such that the saturation value of energy release rate was 67.5 J/m^2 for a 4.1 μm grain sized specimen and 110 J/m^2 for a 9.3 μm grain sized specimen (Table 3.4.5).

Table 3.4.5. The energy release rate behavior for alumina specimens with different grain size using double torsion testing [44].

Grain size, μm	Initial energy release rate, J/m^2	Saturated energy release, rate J/m^2	Crack length at saturation, mm
4.1	34	67.5	11.2
5.6	33.5	77	10.4
6.24	32	80	10
6.6	33	81.5	8
8.43	40	98.5	8.5
9.32	57	105	7.3
9.75	53	110	7.3

The grain bridging zone length, which may be defined as the crack extension required for the energy release rate to obtain steady state, decreased as grain size increased. For

example, a crack extension of 11.2 mm was required for 4.1 μm grain sized specimen while 7.3 mm was needed for 9.3 μm grain sized specimen. SEM observations (magnification × 2.0 k to 4.0 k) also showed evidence of grain behind crack tip which can exert a crack closure force.

3.4.3.8. The effect and observation of grain bridging by Braun *et al.* [45]

For Al_2O_3-Al_2TiO_5 (20 volume % of Al_2TiO_5) composite disk specimens 30 mm in diameter and 4 mm thick, Braun *et al.* [45] introduced an indentation crack at the center of specimens (5 specimens) using a load range of 20-300 N. Fracture toughness was investigated by observing crack growth. The crack lengths were measured by an optical microscope during the applied loading. Toughness increased with increasing crack length from 1.8 $MPam^{1/2}$ at a crack length of 100 μm to 4.8 $MPam^{1/2}$ at a crack length of 2000 μm. Scanning electron microscope (SEM) observations showed evidence of grain interlocking bridging at crack interface during crack extension.

To observe flaw resistance for Al_2O_3-Al_2TiO_5 specimen, Vickers indentation cracks were introduced on a disk specimen (20 mm diameter and 3 mm thickness) and strength was measured using a three ball point support test. Strength decreased slightly as indentation load increased from 260 MPa (at an indentation loading 2 N) to 200 MPa (at an indentation loading 300 N) (Table 3.4.6). However, the toughness was insensitive to indentation load; the fracture toughness was 2.9 $MPam^{1/2}$ for a 300 N indentation load and 2.7 $MPam^{1/2}$ for 20 N indentation load.

Table 3.4.6. The strength behavior for cracks produced by different indentation loads to observe flaw resistance for Al_2O_3-Al_2TiO_5 composite [45].

Indentation load, N	3	5	10	12	100	200	300
Strength, MPa	260	265	265	235	220	200	218

The observation of crack length as a function of applied load showed an increasing crack resistance by grain interlocking bridging for the Al_2O_3-Al_2TiO_5 composite. SEM micrographs revealed the evidence of grain bridging. In addition, indentation load-strength behavior indicated Al_2O_3-Al_2TiO_5 composite is a highly flaw resistant material.

3.4.3.9. The effect and observation of grain bridging by Steinbrech *et al.* [43]

Steinbrech *et al.* [43] cold isostatically pressed and then sintered alumina power (CT 8000, Alcoa, Frankfrut am Main, FRG) in air at 1700 °C. The mean grain sizes of the alumina were 4 μm to 17 μm. Specimens were machined into single edge notched beam specimens (SENB) of dimension 7 mm × 60 mm × 5 mm and short double cantilever beam specimens (s-DCB) of dimension 24 mm × 12.5 mm ×2 mm. For the s-DCB, the energy release rate increased to about 103 J/m^2 as the cracks extended under load (Figure 3.4.7). The initial energy release rate was less than 20 J/m^2 (Figure 3.4.7). The energy saturates when the crack opening displacement reaches about 1/4 of the grain size. If crack opening displacement was greater than 1/4 of grain size, no further grain bridging occurred and the energy release rate saturated.

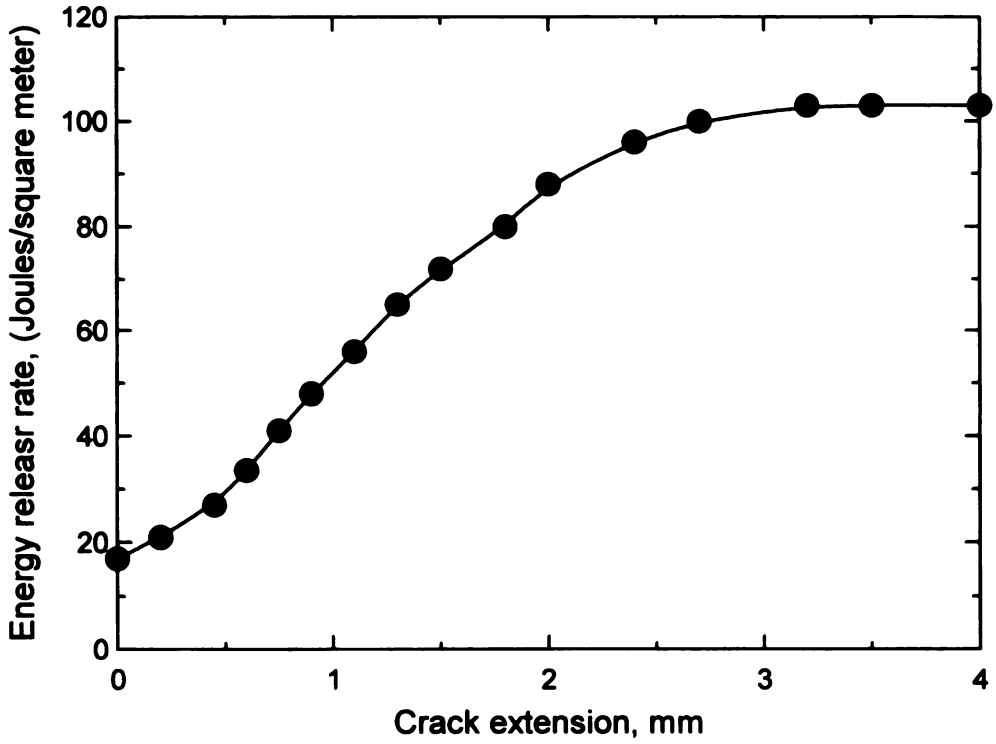

Figure 3.4.7. Energy release rate as crack extension increases for alumina s-DCB alumina specimen [43]. Crack growth was quasi-static from initial notch to fracture.

For SENB specimens, Steinbrech *et al.* observed the crack resistance behavior as a function of crack length (normalized crack length, crack length/width of specimen) at different notch depths (Table 3.4.7). Initial energy release rates were independent of initial notch depth. The slope of energy release rate versus normalized crack length increased as the initial notch depth increased. For the smallest initial notch depth (1.54 mm), the energy release rate saturated but the other SENB specimens did not show a saturation behavior.

Table 3.4.7 implies that energy saturation behavior is related to crack opening displacement. The crack length, when crack opening displacements reached 1/4 of the grain size, increased as initial notch depth increased (Table 3.4.7). Thus the energy release rate saturated for smallest initial crack depth because crack opening displacement reached 1/4 of grain size at about 70 percent of final fracture crack length as explained by the above for s-DCB specimen. However, COD for rest of the SENB specimens reached 1/4 of the grain size at about 88 -100 percent of final crack length thus saturation behavior may not occur.

Thus, Steinbrech *et al.* [43] investigated grain bridging effects in alumina specimens by measuring the energy release rates. The grain bridging effect displayed a critical crack opening displacement at which no further grain bridging occurred.

Table 3.4.7. The energy release rate as a function of normalized crack length (crack length/width of specimen) in SENB alumina specimen which had 16 μm average grain size where width of specimen was 7 mm [43].

Notch depth, mm	Initial normalized crack length	Initial energy release rate, J/m^2	Final normalized crack length	Final energy release rate, J/m^2	Normalized crack length at COD = 4 μm
1.5	0.22	20	0.87	105	0.65
2.8	0.4	20	0.9	105	0.79
4.2	0.6	20	0.9	120	8.7
5.3	0.76	20	0.93	105	9.3

3.4.3.10. The effect and observation of grain bridging by Rodel *et al.* [46]

Rodel *et al.* [46] observed bridged crack interfaces using a scanning electron microscope. Alumina disk-shaped specimens (100 mm in diameter and 4 mm thick disk) were made by hot pressing fine alumina powder (Sumitomo AKP-HP grade) at 1650 °C for 35 hours under 35 MPa. The density was greater than 99.9 % of theoretical density and the mean grain size was 11 μm. Disk specimens were machined to form 1 mm thick compact tension specimens.

Grain bridgings was observed along the crack trace for applied loads of 5 N to 300 N. The measured crack opening displacement (COD) increased with crack extension from 200 nm at a crack extension 190 μm to 1200 nm at crack extension 1700 μm, where crack extension defined as the change of crack length from the initial crack length. The energy release rate indicated the existence of a bridging effect since the crack resistance

increased as the crack extension increased. The energy release rates were from 10 J/m^2 at 0 crack extension and increased to 50 J/m^2 for a 1700 μm crack extension.

3.4.3.11. The effect and observation of grain bridging by Reichl *et al.* [47]

Reichl *et al.* [47] determined crack bridging force using polycrystalline alumina whose mean grain size was 16 μm. To measure the crack bridging force, double cantilever beam specimens (30 mm × 25 mm × 2 mm) were modified by adding a second notch at the rear of specimen (Figure 3.4.8). The loading-crack opening displacement (COD) curve (Figure 3.4.8) shows that at a COD of 65 μm, the load abruptly decreases when the crack tip meets the second rear notch. The load (P_c) corresponding to an abrupt load decrease represents the "load bearing capacity" of wake zone since no obstruction exists at the crack tip. The maximum COD (δ_m) of interlocking zone and the wake zone itself are depicted in Figure 3.4.9. The bridged zone load, P_b, is calculated from

$$P_b = 2P_c\delta / \delta_m \tag{3.4.2}$$

where δ = crack opening displacement in the direction of applied load

δ_m = maximum crack opening displacement for the interlocking zone.

From Figure 3.4.9, bridging stress is

$$S_b = \frac{P_b}{zw} \tag{3.4.3}$$

S_b = bridging stress

z = length of bridging zone

w = width of specimen

Length of bridging zone, z, is related to COD (Figure 3.4.9) such that

$$\frac{1}{z} = \frac{1}{a}\frac{\delta}{\delta_m} \tag{3.4.4}$$

where a = distance between the direction of applied load and the second notch tip.

If equation 3.4.3 is inserted into equation 3.4.2, we can obtain

$$S_t = 2P_c(\frac{\delta}{\delta_m})^2 / wa \ . \tag{3.4.4}$$

For 12 polycrystalline alumina specimens, Reichl *et al.* calculated the bridging stress as 29±3 MPa.

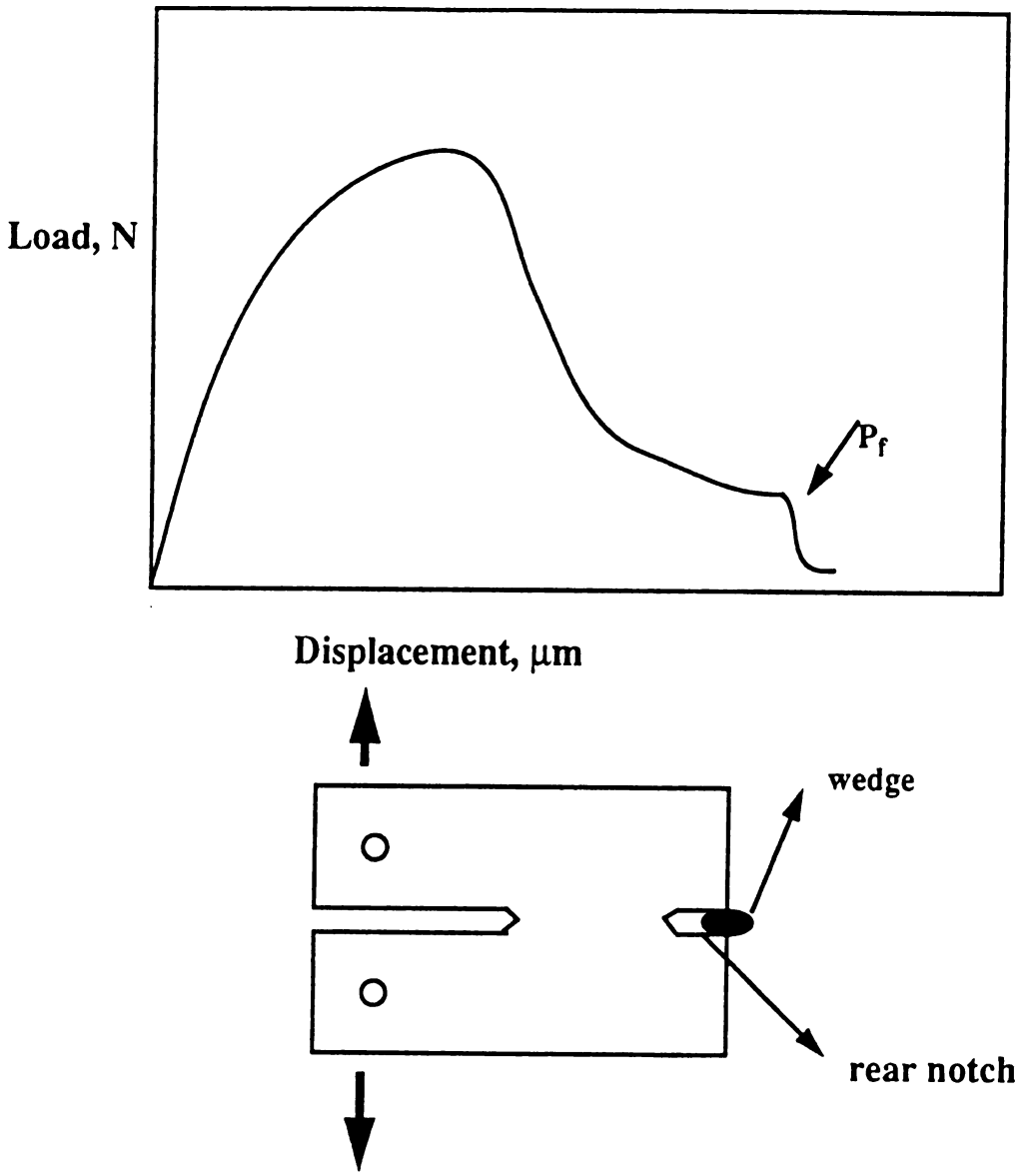

Figure 3.4.8. Load-displacement behavior and the modified double cantilever specimen used by Reichl to study grain bridging in alumina specimens [47].

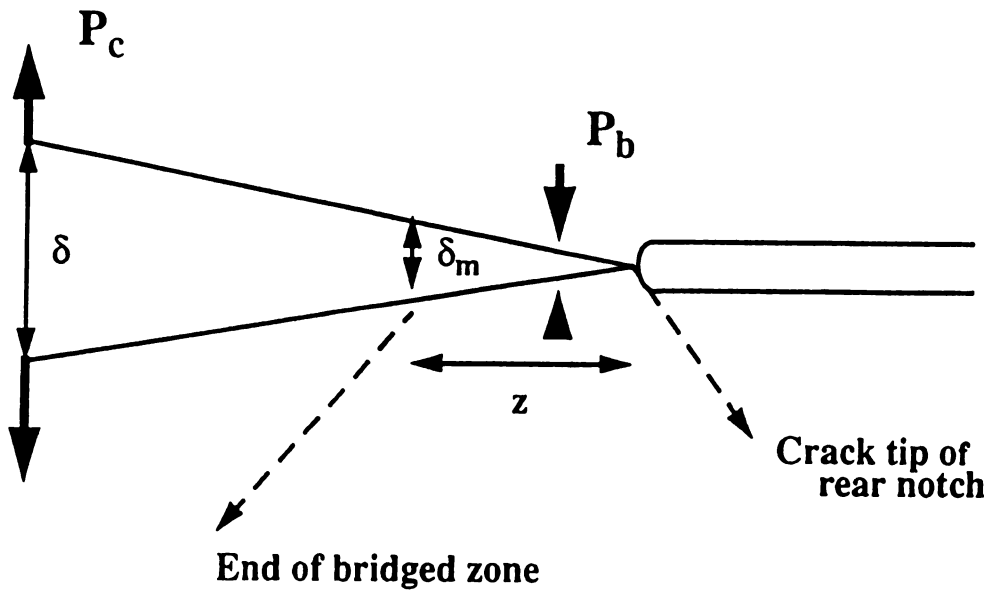

Figure 3.4.9. The assumption of geometry near the crack tip to calculate the average bridging stress by Reichl *et al.* [47].

3.4.5. Crack propagation behavior and grain bridging of the unreinforced polycrystalline alumina included in this study

Using a scanning electron microscope (JEOL, JSM 6400V), crack shape and grain bridging were observed for three polycrystalline alumina specimens that had been quenched into deionized water as a part of this study. Each of the three specimens viewed in the SEM underwent a total of ten thermal shock cycles at a fixed value of ΔT prior to the SEM measurements.

In order to determine whether the nature of the grain bridging changes as the severity of the thermal shock damage changes, the three specimens selected to represent relatively low, moderate, and high values of thermal fatigue damage. For the low thermal fatigue specimen, specimen A4-14 was selected which underwent 10 thermal shocks at a quench -temperature difference of 270 °C. The moderate and highly damaged states were represented by specimens A5-3 and specimen A5-5, respectively. Specimen A5-3 was shocked for ten cycles at $\Delta T = 300$ °C while specimen A5-5 was shocked for 10 cycles at $\Delta T = 320$ °C. The crack length versus cumulative number of thermal shock data for A4-14, A5-3, and A5-5 are included in section 3.3 of this thesis.

The relative positions of the SEM crack observation crack is given schematically in Figure 3.4.10. The crack shape after thermal fatigue is shown in Figure 3.4.11 for (a) specimen A4-14 with a quench temperature difference of 270 °C (b) specimen A5-5 with a quench temperature difference of 320 °C. The severity of thermal fatigue damage larger

at $\Delta T = 320\ ^{o}C$ than at $\Delta T = 270\ ^{o}C$ (Figure 3.4.11) which corresponds to the crack length measurement .

The crack propagation paths for specimen A5-5 (quench temperature difference 320 ^{o}C) were observed at a magnification of × 2500 and an accelerating voltage of 20 kV at positions (a) behind crack tip and (b) near the center of the radial crack (Figure 3.4.12). Both crack propagation paths show that cracks grew in a transgranular mode and there is no evidence of grain bridging sites along the surface trace of the crack. Grain bridging does appear behind the crack tip for the specimen quenched at (a) $\Delta T = 270\ ^{o}C$ and near the crack tip for the specimen quenched at (b) $\Delta T = 300\ ^{o}C$ (Figure 3.4.13).

Grain bridging can be a source of crack growth resistance. However, the grain bridging sites were not observed in other areas of these two specimens. Thus, it appears that the grain bridging rarely affects crack propagation under cyclic thermal shock testing for the alumina specimens included in this study.

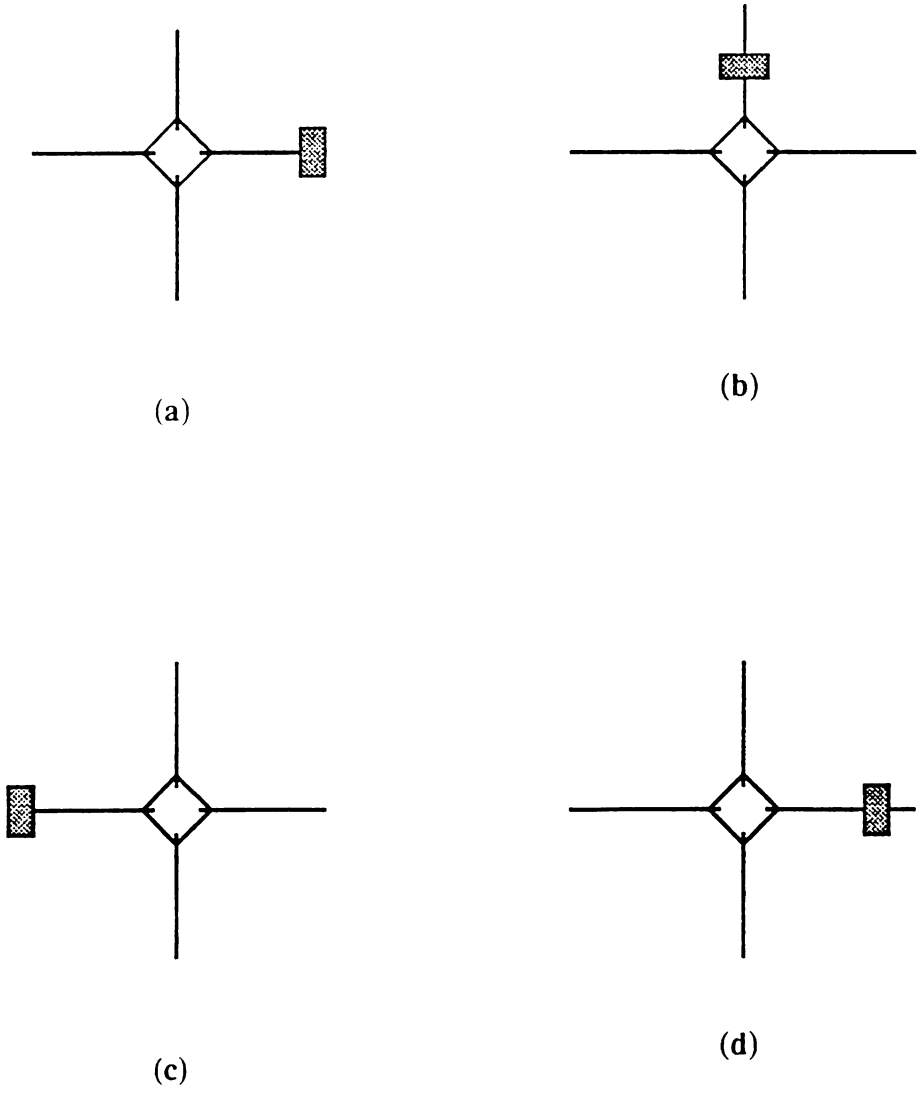

Figure 3.4.10. The position of SEM observation for unreinforced polycrystalline alumina specimen after ten thermal quenching (a) $\Delta T = 320\ ^{\circ}C$ behind the crack tip (b) $\Delta T = 320\ ^{\circ}C$ at the middle of the radial crack (c) $\Delta T = 270\ ^{\circ}C$ around the crack tip (d) $\Delta T = 300\ ^{\circ}C$ behind the crack tip.

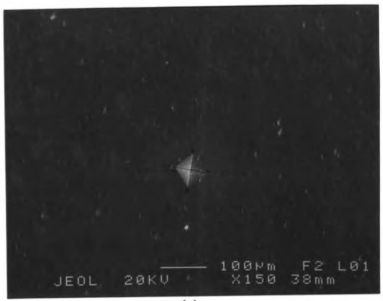

(a)

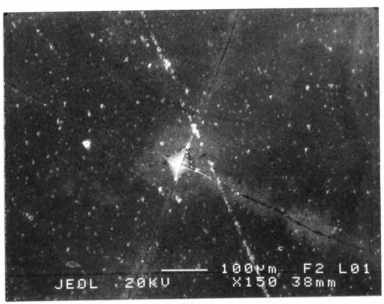

(b)

Figure 3.4.11. Crack propagation shape for polycrystalline alumina specimen after 10 quenched thermal shock at (a) ΔT =270 (b) ΔT = 320.

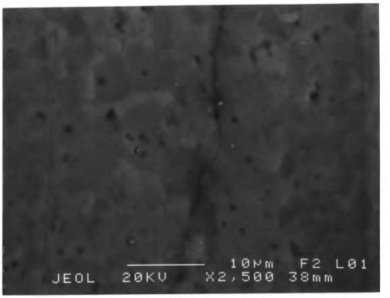

(a)

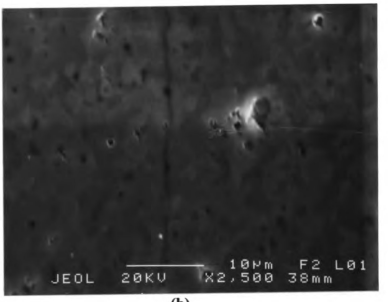

(b)

Figure 3.4.12. The micrograph of crack path for polycrystalline alumina specimen after 10 quenched thermal shock at $\Delta T = 320\ ^{o}C$ (a) behind the crack tip (b) at middle of the radial crack.

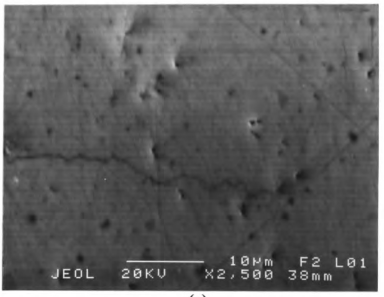

(a)

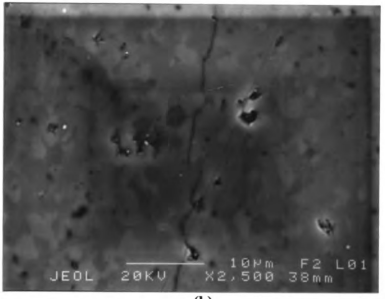

(b)

Figure 3.4.13. The micrograph of bridging site for polycrystalline alumina specimens after 10 quenched thermal shock. (a) $\Delta T = 270\ ^{o}C$ around the crack tip (b) $\Delta T = 300\ ^{o}C$ behind the crack tip.

3.4.6. Grain bridging related to thermal shock for unreinforced alumina

For mechanical loading of ceramics, grain bridging contributes to crack propagation resistance. Vekinnis *et al.* [44] measured the energy release rate for 96 % alumina specimens and showed that the energy release rate increased to about 200 % of the initial energy release rate. The increase in toughness for unreinforced alumina with increasing crack length was explained by grain bridging [44].

To evaluate the grain bridging process, a finite element method was used by Kagawa [33]. The calculated crack closure stress reached 17 MPa for ceramic materials using a FEM program. Grain bridging sites also were observed behind the crack tip in unreinforced alumina specimen via scanning electron microscopy under mechanical loading by Lathabai [34] and Hay *et al.* [35].

Grain bridging can be degraded by repeated loading and unloading. Interfacial friction during cyclic loading degrades the toughness of polycrystalline alumina by fracturing the bridging sites. Kishimoto [37] observed a decrease in fracture toughness, 0.4 $MPam^{1/2}$ immediately after cyclic loading indicating that grain bridging effect decreases under cyclic loading.

Therefore, the grain bridging is an mechanism for energy dissipation during crack growth in unreinforced alumina under mechanical loading.

However, the grain bridging was relatively limited under thermal loading for unreinforced alumina specimen included in this study. Thus the grain bridging may not account for the saturation in the thermal fatigue crack length observation in this study.

One difference between thermal loading performed in this study and mechanical loading done by other researchers is the duration time of loading. Lee [30] calculated time dependent thermal stress. The thermal surface stress increases rapidly to a maximum stress then decreases slowly while the stress-time behavior is symmetrical in mechanical loading (Figure 3.4.14). The time required for maximum stress was calculated as 11 milliseconds for a water quench of alumina [30]. The maximum mechanical loading time is usually much larger than 10 milliseconds; for example 1000 milliseconds [34,37]. However, the loading time for mechanical loading with a frequency of 100 Hz [37] is similar (10 milliseconds) to thermal loading. The other difference related to loading time is that the slope of stress-time curve ($d\sigma/dt$) is much larger in thermal loading than mechanical loading (Figure 3.4.14).

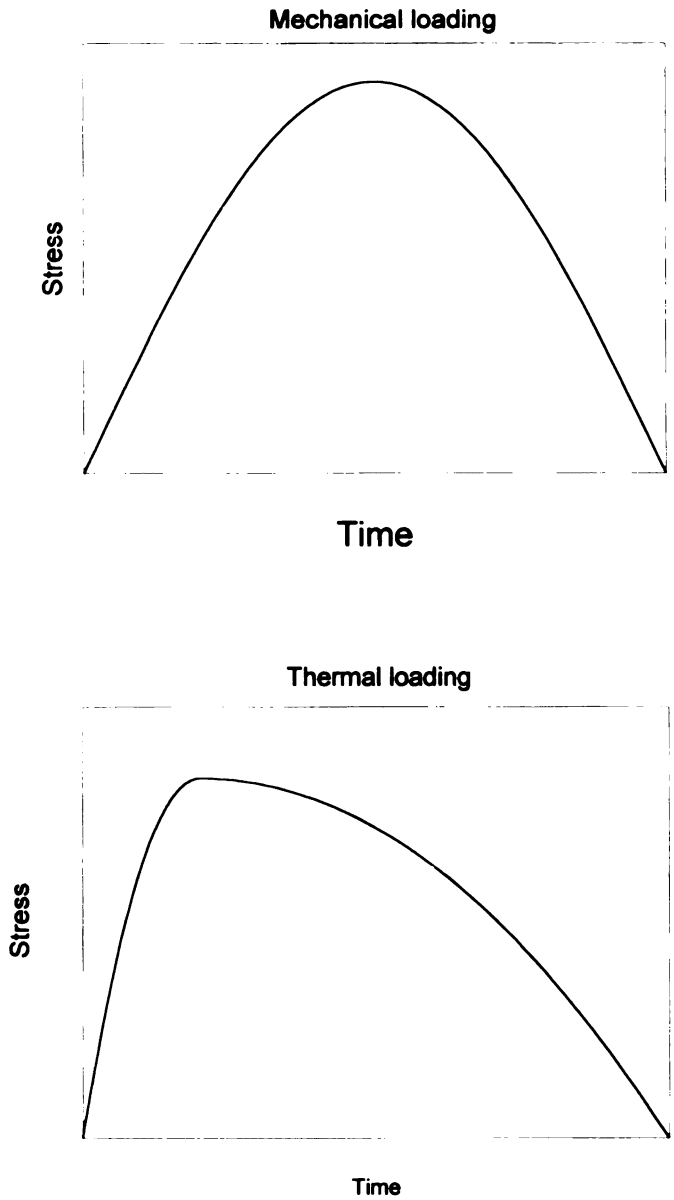

Figure 3.4.14. The schematic diagram of the comparison of stress-time behavior for the mechanical loading and thermal loading [30]

Under thermal shock testing, the thermal fatigue damage of material properties (for example, crack length [32], strength [27], crack number density [25] and elastic modulus [10-12]) saturated as the number of thermal cycles increases. The release of elastic energy is a driving force and the surface fracture energy exerts the retarding force during crack propagation. When the energy is balanced, the crack growth is stopped. At a specific quench temperature difference, the crack grows to a specific value and then crack length saturates; for example a saturated normalized crack length was 1.14 at $\Delta T = 250$ ^{o}C and a saturated normalized crack length was 2.25 at $\Delta T = 320$ ^{o}C in this study. After damage saturation occurs, the fracture surface energy may be a barrier for crack growth.

The spatial distribution through the thickness of the specimen for thermal stress is given in Figure 3.4.15. The stress distribution results from the temperature gradient through the specimen thickness. The surface of specimen is in tension and the stress decreases rapidly from the surface toward the center of specimen (Figure 3.4.15). On the other hand, the stress distribution in mechanical bend loading is linear through the specimen thickness (Figure 3.4.15). The slope ($d\sigma/dy$) is much steeper for thermal loading than for mechanical loading thus the severity of damage on the surface of the specimen is greater in thermal loading than in mechanical loading.

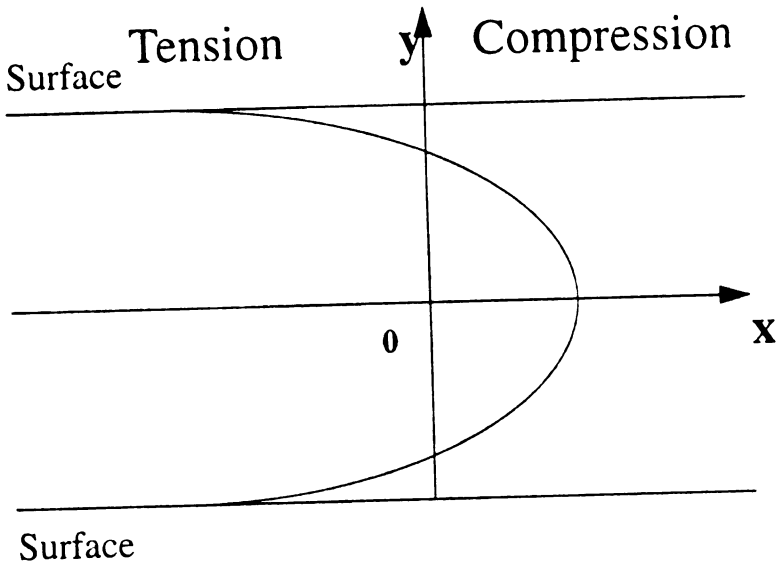

(a) Thermal loading

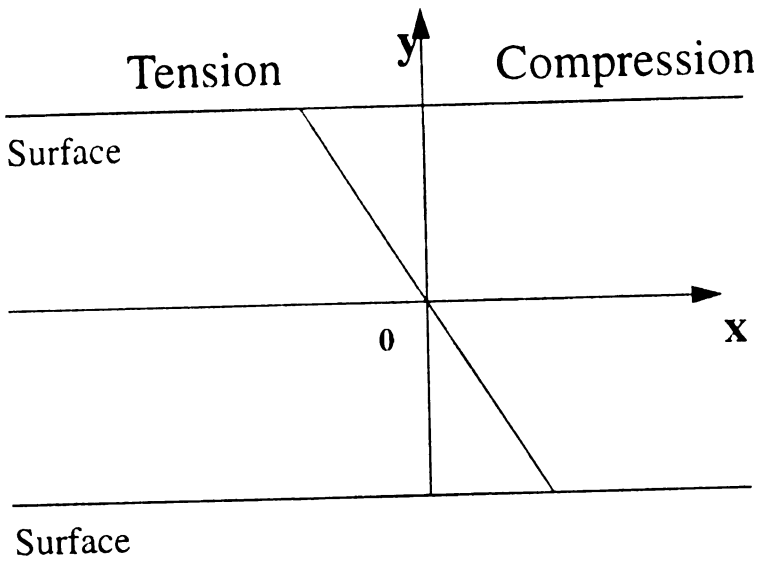

(b) Bend test

Figure 3.4.15. The profile of stress distribution for thermal loading and bend test. The slope ($d\sigma/dy$) is much stiffer in thermal loading than in bend test.

The scatter of rate constant in measuring Vickers indentation cracks, b, is larger than in measuring Young's modulus, α (Table 3.3.3) which can be explained by following relationship [11]

$$E = E_0[1 - f\varepsilon] \tag{3.3.6}$$

where E = Young's modulus

E_0 = Young's modulus of crack free material

ε = crack damage parameter

f = a relative weak function of the material's Poisson's ratio.

The crack damage parameter for a circular crack is defined as [49]

$$\varepsilon = N < c^3 > \tag{3.3.7}$$

where N = number of cracks

<c> = average crack length.

Therefore, Young modulus is proportional to $<c^3>$ and represents an average over the range of crack sizes. Vickers indentation crack measurements represents a single pair of cracks, not an entire distribution of cracks. Thus, using Vickers indentation crack measurements to determine the rate constants, b, for crack growth will result in more scatter than that observed for the rate constant, α, for the Young's modulus measurement data (Table 3.3.3).

4. Summary and Conclusion

4.1. Slow crack growth after initial indentation before commencing thermal shock

A minor amount of slow crack growth was observed for polycrystalline alumina after initial indentation before thermal shock. The relative change in the mean crack length (c_{max}/c_o, see section 3.1) was 1.024 to 1.130. Within 30 minutes, the crack growth saturated.

4.2. Crack growth behavior in room temperature and 80 °C water in the absence of thermal shock

Water can potentially cause crack extension via an environmentally-assistanted slow crack growth process. Slow crack growth behavior was observed in room temperature deionized water and in 80 °C deionized water. For the two polycrystalline alumina specimens tested, however, the crack extensions in the water were not significant since the change of crack length was less than 1 percent in each case. Thus, in this study, the deionized water likely did not significantly affect crack growth during thermal shock test.

4.3. Thermal fatigue behavior unreinforced polycrystalline alumina

Thermal shock damage for unreinforced alumina specimens was investigated by measuring the crack length change. Two groups of polycrystalline alumina specimens were used for thermal fatigue testing. For one set, thermal fatigue tests were done for 10 cumulative quenching cycles with a quench temperature difference range of 250 to 330 °C. For the other set, 20 cumulative thermal shocks were done for polycrystalline

alumina specimens with a quench temperature difference ranging from 250 °C to 305 °C. The cracks grew to 115 percent to 227 percent of initial crack length for the specimens quenched a total of 10 cycles and 115 percent to 230 percent of the initial crack for the specimens quenched a total of 20 cycles.

The crack lengths were fitted via a least-squares procedure(see section 3.3.1 and 3.3.2). The rate constants obtained from the least-squares fit of thermal shock data to equation 3.3.1, were a function of quench temperature difference. The rate constant increased as the quench temperature increased. Lee *et al.*'s [12] and Ash's [32] rate constants behavior showed similar trends. However, the correlation coefficients of this study and Ash's [32] were very poor but the correlation coefficients for Lee *et al.*'s data were much better. The difference in the relative scatter of the data may be related to the fact that for Lee *et al.*'s study, the thermal shock damage assessed by measuring Young's modulus which is sensitive to the ensemble average of crack length. In contrast, for this study and Ash's work, the thermal fatigue damage was assessed in terms of a single system of Vickers indentation cracks.

The severity of thermal fatigue damage is a function of quench temperature difference, as measured by the saturation crack length. The normalized saturation crack lengths (crack length/initial crack length) were linear regressed using a PLOT IT program. The slope was 0.019/°C for 10 quenched specimen and 0.020/°C for 20 quenched specimen. Ash's data [32] showed a good agreement (0.017/°C) with the slopes obtained in this study.

4.4. Grain bridging in the brittle materials

The major toughening mechanism in monophase ceramic material such as alumina is grain bridging [31-45]. Grain bridging is observed behind of crack tip [31-35]. Interlocking of separating interface at the bridging is a source of a crack resistance force. Grain bridging is more effective for coarse grained material than for fine grained materials [33,37]. Crack opening displacement also is related to grain bridging showed that grain bridging may occur when the crack opening displacement is less than 1/3 [35] or 1/4 [43] of grain size of specimen. Evidence of grain bridging is examined through scanning electron microscope observations behind the crack tip [34, 36,37, 41].

In this study, SEM observations of crack growth and grain bridging for three unreinforced polycrystalline alumina specimens which had been subjected to a total of 10 thermal shock cycles for quench temperature differences of 270, 300, and 320 °C. Grain bridging appeared at 1 or 2 sites for specimens quenched at 270 °C and 300 °C. However, grain bridging was not observed in other areas of specimens. Thus, the grain bridging may not account for the crack saturation of crack length under thermal fatigue testing.

5. Appendices

Appendix A. The dimension and label of all specimens

The following tables list the dimension and label of all specimens used in this study. The positions of the Vickers indentations (see Figure 2.3.1) are given under the column labeled "Position." For thermal shock testing, the temperature difference, ΔT, and maximum number of quenching cycles, A_{max} are included. All dimensions were measured by vernier caliper (Mitutoyo).

Table A The dimensions and label for all polycrystalline alumina specimens as measured by vernier caliper.

Label	ΔT, °C	Position	N_{max}	Width, mm	Length, mm	Thickness, mm
A1-11	*	m	*	10.15	9.94	1.02
A1-13	*	m	*	14.06	9.93	0.99
A1-14	*	m	*	10.09	9.96	1.01
A2-8e	*	e	*	10.04	9.95	1.0
A2-8m	*	m	*	10.04	9.95	1.0
A2-9e	*	e	*	10.30	9.96	1.04
A2-9m	*	m	*	10.30	9.96	1.04
B1-3	*	m	*	9.91	9.89	0.94
B1-4	*	m	*	10.36	9.98	0.96
A4-13	250	m	10	10.34	10.02	1.03
A4-14	270	m	10	10.06	10.38	1.01
A4-15	290	m	10	9.99	9.93	1.01
A6-2	295	m	10	9.87	9.95	1.00
A5-3	300	m	10	9.95	9.99	1.01
A5-12	305	m	10	10.07	10.07	0.98
A5-4	310	m	10	10.0	10.45	1.02
A5-11	315	m	10	10.05	10.25	0.99
A5-5	320	m	10	10.05	9.95	0.96
A5-8	325	m	10	10.14	9.97	1.01
A5-7	330	m	10	9.94	10.11	1.03
A6-3	250	m	20	9.95	10.40	1.04
A6-4	270	m	20	13.95	9.95	1.01
B1-5	290	m	20	10.33	9.91	1.01
A5-10	295	m	20	9.95	10.05	0.90
A5-14	300	m	20	9.94	10.0	0.94
A6-1	305	m	20	9.95	9.90	0.92

Appendix B. The result of slow crack growth testing after initial indentation but before commencing thermal shock

Following tables are the crack lengths as time elapsed after initial indention crack. The mean crack lengths were calculated by the average of x-directional and y-directional crack lengths. The relative crack lengths are also given by dividing initial crack length. Table B shows the crack length saturated in 30 minutes.

Table B-1. The crack lengths and elapsed time to examine the slow crack growth after introducing Vickers indentation crack for alumina specimen(specimen A1-11).

Time minutes	x-dir. crack length (μm), A	y- dir. crack length (μm), B	A/ 234.2	B/231.3	mean crack length(μm), C	C/232.8
2	234.2	231.3	1	1	232.8	1
7	243.7	231.6	1.041	1.001	237.7	1.021
10	244.6	232.6	1.044	1.006	238.6	1.025
13	244.8	232.5	1.045	1.005	238.7	1.025
37	244.1	231.9	1.042	1.003	238.0	1.023
64	244.3	232.1	1.043	1.003	238.2	1.023
96	244.8	232.4	1.045	1.005	238.6	1.025
1320	244.3	231.7	1.043	1.002	238.0	1.023
1357	244.5	231.2	1.044	1.000	237.9	1.022
1474	244.5	232.0	1.044	1.003	238.3	1.024

Table B-2. The crack lengths and elapsed time to examine the slow crack growth after introducing Vickers indentation crack for alumina (specimen A1-13).

Time minutes	x-dir. crack length (μm), A	y- dir. crack length (μm), B	A/ 197.0	B/225.0	mean crack length(μm), C	C/211.0
1	197.0	225.0	1	1	211.0	1
3	203.3	228.5	1.032	1.016	215.9	1.023
5	211.5	229.2	1.074	1.019	220.3	1.044
14	209.7	239.2	1.064	1.063	224.5	1.064
21	209.0	241.3	1.061	1.072	225.2	1.067
26	211.5	241.6	1.074	1.074	226.6	1.074
38	213.5	240.7	1.084	1.070	227.1	1.076
68	212.3	241.2	1.078	1.072	226.8	1.075
837	214.0	239.8	1.086	1.066	226.9	1.075
1178	213.7	240.2	1.085	1.068	227.0	1.076
1386	213.5	240.9	1.084	1.071	227.2	1.077

Table B-3. The crack lengths and elapsed time to examine the slow crack growth after introducing Vickers indentation crack for alumina specimen (specimen A1-14).

Time minutes	x-dir. crack length (μm), A	y- dir. crack length (μm), B	A/ 180.1	B/216.1	mean crack length(μm), C	C/198.1
1	180.1	216.1	1	1	198.1	1
4	184.4	222.8	1.024	1.031	203.6	1.028
8	186.8	221.6	1.037	1.025	204.2	1.031
13	202.6	221.8	1.125	1.026	212.2	1.071
20	207.2	220.3	1.150	1.019	213.8	1.079
28	208.7	225.6	1.159	1.044	217.2	1.096
35	222.2	224.3	1.234	1.038	223.3	1.127
50	223.1	225.1	1.238	1.042	224.1	1.131
537	223.3	224.7	1.240	1.040	224.0	1.131
660	223.6	224.5	1.242	1.039	224.1	1.131
1294	222.7	225.1	1.237	1.042	223.9	1.130
1495	223.0	224.8	1.238	1.040	223.9	1.130

Table B-4. The crack lengths and elapsed time to examine the slow crack growth after introducing Vickers indentation crack for alumina specimen (specimen A2-8e), where "e" means the edge of specimen.

Time minutes	x-dir. crack length (μm), A	y- dir. crack length (μm), B	A/ 232.3	B/227.9	mean crack length(μm), C	C/230.1
2	232.3	227.9	1	1	230.1	1
12	235.3	229.9	1.013	1.009	232.6	1.011
22	240.0	231.6	1.033	1.016	235.8	1.025
29	239.9	230.9	1.033	1.013	235.4	1.023
37	242.4	231.2	1.043	1.014	236.8	1.029
84	241.5	231.5	1.040	1.016	236.5	1.028
143	243.2	231.6	1.047	1.016	237.4	1.032
201	243.6	231.4	1.049	1.015	237.5	1.032
359	243.1	230.9	1.046	1.013	237.0	1.030
514	243.3	231.2	1.047	1.015	237.3	1.031
1220	242.7	231.6	1.045	1.016	237.2	1.031
1424	243.4	230.9	1.048	1.013	237.2	1.031

Table B-5. The crack lengths and elapsed time to examine the slow crack growth after introducing Vickers indentation crack for alumina specimen (specimen A2-8m), where "m" means the middle of specimen.

Time minutes	x-dir. crack length (μm), A	y- dir. crack length (μm), B	A/ 206.3	B/228.9	mean crack length(μm), C	C/217.6
1	206.3	228.9	1	1	217.6	1
11	206.5	230.9	1.001	1.009	218.7	1.005
22	207.7	232.1	1.007	1.014	219.9	1.011
27	208.6	232.8	1.011	1.017	220.7	1.014
34	212.2	233.0	1.029	1.018	222.6	1.023
82	217.9	232.7	1.056	1.017	225.3	1.035
141	218.7	232.2	1.060	1.014	225.5	1.036
199	218.6	232.8	1.060	1.017	225.7	1.037
358	218.4	232.4	1.059	1.015	225.4	1.036
513	218.2	232.7	1.058	1.017	225.5	1.036
1328	218.5	232.2	1.060	1.014	225.4	1.036
1482	218.1	232.1	1.057	1.014	225.1	1.034

Table B-6. The crack lengths and elapsed time to examine the slow crack growth after introducing Vickers indentation crack for alumina specimen (specimen A2-9e), where "e" means the edge of specimen.

Time minutes	x-dir. crack length (μm), A	y- dir. crack length (μm), B	A/ 245.7	B/210.1	mean crack length(μm), C	C/227.9
2	245.7	210.1	1	1	227.9	1
9	250.0	218.8	1.018	1.041	234.4	1.029
13	251.2	220.2	1.022	1.048	235.7	1.034
18	259.0	221.2	1.054	1.053	240.1	1.054
23	259.9	220.6	1.058	1.050	240.3	1.054
27	260.5	220.5	1.060	1.050	240.5	1.055
31	259.4	220.2	1.056	1.048	239.8	1.052
43	258.7	221.3	1.053	1.053	240.0	1.053
202	259.6	221.5	1.057	1.054	240.6	1.056
357	260.1	221.7	1.058	1.055	240.9	1.057
1053	259.2	220.9	1.055	1.051	240.1	1.053
1264	259.7	221.2	1.057	1.053	240.5	1.055
1436	259.6	221.5	1.057	1.054	240.6	1.056

Table B-7. The crack lengths and elapsed time to examine the slow crack growth after introducing Vickers indentation crack for alumina specimen (specimen A2-9m), where "m" means the middle of specimen.

Time minutes	x-dir. crack length (μm), A	y- dir. crack length (μm), B	A/ 214.9	B/179.7	mean crack length(μm), C	C/197.3
1	214.9	179.7	1	1	197.3	1.000
8	215.0	180.6	1.000	1.005	197.8	1.003
12	217.4	181.2	1.012	1.008	199.3	1.010
18	219.2	181.5	1.020	1.010	200.4	1.016
22	219.0	184.5	1.019	1.027	201.8	1.023
26	219.4	189.5	1.021	1.055	204.5	1.037
42	218.7	188.2	1.018	1.047	203.5	1.031
202	218.9	189.0	1.019	1.052	204.0	1.034
356	219.2	189.1	1.020	1.052	204.2	1.034
1052	219.5	188.7	1.021	1.050	204.1	1.035
1263	219.1	189.0	1.020	1.052	204.1	1.034
1435	218.8	189.6	1.018	1.055	204.2	1.035

Appendix C. Crack length versus time for Vickers indented specimens immersed in the room temperature deionized water and in 80 °C deionized water. The specimens were not subjected to thermal shock.

Following tables give crack length versus time for an indented and aged specimen immersed in deionized water. Table C-1 shows the crack length with elapsed time in room temperature deionized water. Table C-1 is the crack length with water temperature at each testing. The mean values are the average of the crack lengths in the x-direction length and in the y-direction.

Table C-1. Crack length versus time for Vickers indentation immersed in room temperature deionized water (specimen B1-3).

Time (hours)	x-dir. (μm), A	y-dir. (μm), B	mean (μm), C	A/235.4	B/242.2	C/238.9
0	235.4	242.4	238.9	1	1	1
1	233.6	238.4	236.0	0.992	0.983	0.988
2	234.7	239.6	237.2	0.997	0.988	0.993
3	233.9	238.5	236.2	0.994	0.984	0.989
4	234.2	241.1	236.0	0.995	0.995	0.995
6	233.6	238.4	237.2	0.992	0.983	0.988
17	234.6	240.7	236.7	0.997	0.993	0.995
20	234.2	240.2	236.6	0.995	0.991	0.993
33	233.7	239.6	237.7	0.993	0.988	0.991
45	234.1	241.2	237.7	0.994	0.995	0.995
49	234.2	239.0	237.7	0.995	0.986	0.990
75	233.8	240.9	237.4	0.993	0.994	0.994
92	234.0	240.1	237.1	0.994	0.991	0.992

Table C-2 is the crack length in 80 °C deionized water at each testing. The mean values are the average of the crack lengths in the x-direction and in the y-direction length.

Table C-2. The crack length versus elapsed time in the hot water (~ 80 °C). The specimen held in 80 °C for 2 hours at each times (see section 2.5, specimen B1-4).

Times	Temp. (°C)	x-dir. (μm), A	y-dir. (μm), B	mean (μm), C	A/234.1	B/237.3	C/235.7
0		234.1	237.3	235.7	1	1	1
1	81	231.0	235.5	233.3	0.987	0.992	0.990
2	76	233.4	236.6	235.0	0.997	0.997	0.997
3	84	233.2	235.9	234.6	0.996	0.994	0.995
4	81	233.0	236.4	234.7	0.995	0.996	0.996
5	82	233.5	237.1	235.3	0.997	0.999	0.998
6	79	232.9	236.6	234.8	0.995	0.997	0.996
7	82	233.1	237	235.1	0.996	0.999	0.997
8	83	233	236.7	234.9	0.995	0.997	0.996
9	81	233.4	236.5	235.0	0.997	0.997	0.997

Appendix D. The thermal shock data

Following tables are all data of thermal shock test for a total of 10 thermal cycles and a total of 20 quenched specimen using an optical microscope (see section 2.6.)

Table D-1. The crack length after cyclic thermal shock test which maximum cycling number is 10 (specimen A4-13 $\Delta T = 250\ ^{\circ}C$).

# of Quench	x-direction A(μm)	y-direction B(μm)	A/233.3 ($c_{0,x}$)	A/255.3 ($c_{0,y}$)	(A+B)/2 M(μm)	C/244.3 ($c_{0,M}$)
0	233.3	255.3	1	1	244.3	1
1	238.7	260.6	1.023	1.020	249.6	1.021
2	235.4	277.3	1.009	1.086	256.3	1.049
3	241.9	287.7	1.036	1.126	264.8	1.083
4	244.7	289.6	1.048	1.134	267.1	1.093
5	244.1	292.0	1.046	1.143	268.0	1.097
6	246.1	292.6	1.054	1.146	269.3	1.102
7	246.6	291.9	1.057	1.143	269.2	1.102
8	248.8	293.9	1.066	1.151	271.3	1.110
9	247.8	295.5	1.062	1.157	271.6	1.112
10	247.8	296.9	1.062	1.162	272.3	1.114

Table D-2. The crack length after cyclic thermal shock test which maximum cycling number is 10 (specimen A4-14 $\Delta T = 270\ ^{\circ}C$)

# of Quench	x-direction A(μm)	y-direction B(μm)	A/252.6 ($c_{0,x}$)	A/260.4 ($c_{0,y}$)	(A+B)/2 M(μm)	C/256.5 ($c_{0,M}$)
0	252.6	260.4	1	1	256.5	1
1	263.7	262.1	1.043	1.006	262.9	1.024
2	260.1	261.4	1.029	1.003	260.7	1.016
3	275.1	275.6	1.089	1.058	275.3	1.073
4	273.1	277.6	1.081	1.066	275.3	1.073
5	273.7	288.6	1.083	1.108	281.1	1.096
6	275.9	293.9	1.092	1.128	284.9	1.110
7	278.3	299.8	1.101	1.151	289.0	1.126
8	279.3	299.9	1.105	1.151	289.6	1.129
9	280.4	304.1	1.110	1.167	292.2	1.139
10	279.8	306.4	1.107	1.176	293.1	1.142

Table D-3. The crack length after cyclic thermal shock test which maximum cycling number is 10 (specimen A4-15 $\Delta T = 290\ ^{\circ}C$).

# of Quench	x-direction A(μm)	y-direction B(μm)	A/255.1 ($c_{0,x}$)	A/253.5 ($c_{0,y}$)	(A+B)/2 M(μm)	C/254.3 ($c_{0.M}$)
0	255.1	253.5	1	1	254.3	1
1	257.5	268.8	1.009	1.060	263.1	1.034
2	258.2	266.9	1.012	1.052	262.5	1.032
3	260.5	268.7	1.021	1.059	264.6	1.040
4	264.5	269.4	1.036	1.062	266.9	1.049
5	268.9	273.9	1.054	1.080	271.4	1.067
6	269.3	273.0	1.055	1.076	271.1	1.066
7	278.5	283.0	1.091	1.116	280.7	1.104
8	278.3	283.4	1.090	1.117	280.8	1.104
9	279.9	284.0	1.097	1.120	281.9	1.108
10	282.4	286.9	1.107	1.131	284.6	1.119

Table D-4. The crack length after cyclic thermal shock test which maximum cycling number is 10 (specimen A6-2 $\Delta T = 295\ ^{\circ}C$).

# of Quench	x-direction A(μm)	y-direction B(μm)	A/250.3 ($c_{0,x}$)	A/252.5 ($c_{0,y}$)	(A+B)/2 M(μm)	C/251.4 ($c_{0.M}$)
0	250.3	252.5	1	1	251.4	1
1	363.1	331.3	1.450	1.312	347.2	1.381
2	400.3	342.0	1.599	1.354	371.1	1.476
3	433.9	360.6	1.733	1.428	397.2	1.580
4	437.1	394.0	1.746	1.560	415.5	1.652
5	438.1	477.2	1.750	1.889	457.6	1.820
6	498.7	488.5	1.992	1.934	493.6	1.963
7	516.7	502.2	2.064	1.988	509.4	2.026
8	516.3	505.7	2.062	2.002	511.0	2.032
9	520.4	500.7	2.079	1.982	510.5	2.030
10	524.4	503.1	2.095	1.992	513.7	2.043

Table D-5. The crack length after cyclic thermal shock test which maximum cycling number is 10 (specimen A5-3 $\Delta T = 300\ ^{\circ}C$).

# of Quench	x-direction A(μm)	y-direction B(μm)	A/267.1 ($c_{0,x}$)	A/243.7 ($c_{0,y}$)	(A+B)/2 M(μm)	C/255.4 ($c_{0,M}$)
0	267.1	243.7	1	1	255.4	1
1	294.3	326.2	1.101	1.338	310.2	1.214
2	298.4	327.9	1.117	1.345	313.1	1.226
3	295.0	332.7	1.104	1.365	313.8	1.228
4	300.5	330.2	1.125	1.354	315.3	1.234
5	305.3	332.0	1.143	1.362	318.6	1.247
6	309.4	339.8	1.158	1.394	324.6	1.270
7	308.5	344.6	1.154	1.414	326.5	1.278
8	309.5	344.9	1.158	1.415	327.2	1.281
9	308.1	348.4	1.153	1.429	328.2	1.285
10	308.3	346.6	1.154	1.422	327.4	1.282

Table D-6. The crack length after cyclic thermal shock test which maximum cycling number is 10 (specimen A5-12 $\Delta T = 305\ ^{\circ}C$).

# of Quench	x-direction A(μm)	y-direction B(μm)	A/249.6 ($c_{0,x}$)	A/235 ($c_{0,y}$)	(A+B)/2 M(μm)	C/242.3 ($c_{0,M}$)
0	249.6	235.0	1	1	242.3	1
1	264.0	263.0	1.057	1.119	263.5	1.087
2	296.2	288.9	1.186	1.229	292.5	1.207
3	389.2	355.0	1.559	1.510	372.1	1.535
4	502.0	432.1	2.011	1.838	467.0	1.927
5	544.3	436.6	2.180	1.857	490.4	2.024
6	566.9	449.2	2.271	1.911	508.0	2.096
7	571.1	447.9	2.288	1.905	509.5	2.102
8	584.6	457.2	2.342	1.945	520.9	2.149
9	591.2	481.5	2.368	2.048	536.3	2.213
10	589.1	485.2	2.360	2.064	537.1	2.216

Table D-7. The crack length after cyclic thermal shock test which maximum cycling number is 10 (specimen A5-4 $\Delta T = 310\ ^{\circ}C$).

# of Quench	x-direction A(μm)	y-direction B(μm)	A/242.7 ($c_{0,x}$)	A/260.8 ($c_{0,y}$)	(A+B)/2 M(μm)	C/251.7 ($c_{0.M}$)
0	242.7	260.8	1	1	251.7	1
1	349.6	343.2	1.440	1.315	346.4	1.375
2	364.1	361.0	1.500	1.384	362.5	1.439
3	367.6	363.6	1.514	1.394	365.6	1.451
4	370.0	364.4	1.524	1.397	367.2	1.458
5	374.4	379.1	1.542	1.453	376.7	1.496
6	378.2	389.0	1.558	1.491	383.6	1.523
7	379.6	387.8	1.564	1.486	383.7	1.523
8	377.2	390.9	1.554	1.498	384.0	1.525
9	379.0	391.4	1.561	1.500	385.2	1.529
10	379.0	395.1	1.561	1.514	387.0	1.537

Table D-8. The crack length after cyclic thermal shock test which maximum cycling number is 10 (specimen A5-11 $\Delta T = 315\ ^{\circ}C$).

# of Quench	x-direction A(μm)	y-direction B(μm)	A/246.9. ($c_{0,x}$)	A/241.7 ($c_{0,y}$)	(A+B)/2 M(μm)	C/244.3 ($c_{0.M}$)
0	246.9	241.7	1	1	244.3	1
1	389.8	315.5	1.578	1.305	352.6	1.443
2	519.8	394.4	2.105	1.631	457.1	1.871
3	527.2	457.3	2.135	1.892	492.2	2.014
4	553.0	458.0	2.239	1.894	505.5	2.069
5	581.8	469.5	2.356	1.942	525.6	2.151
6	590.2	464.6	2.390	1.922	527.4	2.158
7	595.6	470.0	2.412	1.944	532.8	2.180
8	597.9	472.0	2.421	1.952	534.9	2.189
9	600.7	471.3	2.432	1.949	536	2.194
10	607.7	469.0	2.461	1.940	538.3	2.203

Table D-9. The crack length after cyclic thermal shock test which maximum cycling number is 10 (specimen A5-5 $\Delta T = 320\ ^{\circ}C$).

# of Quench	x-direction A(μm)	y-direction B(μm)	A/261.9 ($c_{0,x}$)	A/260.3 ($c_{0,y}$)	(A+B)/2 M(μm)	C/261.1 ($c_{0.M}$)
0	261.9	260.3	1	1	261.1	1
1	341.4	309.7	1.303	1.189	325.0	1.246
2	373.9	354.4	1.427	1.361	364.1	1.394
3	475.9	479.8	1.817	1.843	477.8	1.830
4	511.1	520.9	1.951	2.001	516.0	1.976
5	513.1	538.0	1.959	2.066	525.5	2.012
6	525.2	554.3	2.005	2.129	539.7	2.067
7	564.9	580.4	2.156	2.229	572.6	2.193
8	575.1	589.1	2.195	2.263	582.1	2.229
9	580.3	597.8	2.215	2.296	589.0	2.256
10	578.9	596.3	2.210	2.290	587.6	2.250

Table D-10. The crack length after cyclic thermal shock test which maximum cycling number is 10 (specimen A5-8 $\Delta T = 325\ ^{\circ}C$).

# of Quench	x-direction A(μm)	y-direction B(μm)	A/249.3 ($c_{0,x}$)	A/245.4 ($c_{0,y}$)	(A+B)/2 M(μm)	C/247.3 ($c_{0.M}$)
0	249.3	245.4	1	1	247.3	1
1	313.7	359.1	1.258	1.463	336.4	1.359
2	342.3	367.5	1.373	1.497	354.9	1.434
3	355.1	395.1	1.424	1.610	375.1	1.516
4	440.1	461.8	1.765	1.881	450.9	1.822
5	481.3	499.8	1.930	2.036	490.5	1.982
6	487.5	496.7	1.955	2.024	492.1	1.989
7	504.4	504.1	2.023	2.054	504.2	2.038
8	514.5	530.2	2.063	2.160	522.3	2.111
9	517.4	569.8	2.075	2.321	543.6	2.197
10	541.9	580.6	2.173	2.365	561.2	2.268

Table D-11. The crack length after cyclic thermal shock test which maximum cycling number is 3 (specimen A5-7 $\Delta T = 330\ ^{\circ}C$).

# of Quench	x-direction A(μm)	y-direction B(μm)	A/235.9 ($c_{0,x}$)	A/234.4 ($c_{0,y}$)	(A+B)/2 M(μm)	C/235.1 ($c_{0.M}$)
0	235.9	234.4	1	1	235.1	1
1	424.3	326.7	1.798	1.393	375.5	1.597
2	598.2	409.6	2.535	1.747	503.9	2.143
3	609.8	442.6	2.584	1.888	526.2	2.238
4	*	*				

* After fourth thermal shock, the crack grew to the edge of specimen. Thus further crack length measurements would not have been meaningful.

Table D-12. The crack length after cyclic thermal shock test which maximum cycling number is 20 (specimen A6-3 $\Delta T = 250\ ^{\circ}C$).

# of Quench	x-direction A(μm)	y-direction B(μm)	A/235.0 ($c_{0,x}$)	A/226.4 ($c_{0,y}$)	(A+B)/2 M(μm)	C/230.7 ($c_{0,M}$)
0	235.0	226.4	1	1	230.7	1
1	248.6	256.9	1.058	1.136	252.7	1.095
2	255.2	261.7	1.086	1.156	258.4	1.120
3	262.9	266.1	1.118	1.175	264.5	1.146
4	261.4	268.1	1.112	1.184	264.7	1.147
5	260.9	265.2	1.110	1.171	263.0	1.140
6	263.5	267.4	1.121	1.181	265.4	1.150
7	262.4	265.5	1.116	1.172	263.9	1.144
8	260.6	267.5	1.108	1.181	264.0	1.144
9	262.6	264.7	1.117	1.169	263.6	1.142
10	264.1	264.9	1.123	1.170	264.5	1.146
11	260.8	267.7	1.109	1.182	264.2	1.145
12	261.5	264.6	1.112	1.168	263.0	1.140
13	261.0	268.1	1.110	1.184	264.5	1.146
14	262.9	267.5	1.118	1.181	265.2	1.149
15	260.1	267.6	1.106	1.181	263.8	1.143
16	262.3	264.3	1.116	1.167	263.3	1.141
17	260.8	267.9	1.109	1.183	264.3	1.145
18	262.9	267.7	1.118	1.182	265.3	1.149
19	261.2	267.2	1.111	1.180	264.2	1.145
20	262.4	267.9	1.116	1.183	265.1	1.149

Table D-13. The crack length after cyclic thermal shock test which maximum cycling number is 10 (specimen A6-4 $\Delta T = 270\ ^{\circ}C$).

# of Quench	x-direction A(μm)	y-direction B(μm)	A/248.1 ($c_{0,x}$)	A/251.4 ($c_{0,y}$)	(A+B)/2 M(μm)	C/249.7 ($c_{0.M}$)
0	248.1	251.4	1	1	249.7	1
1	282.8	331.8	1.139	1.319	307.3	1.230
2	297.1	347.8	1.197	1.383	322.4	1.291
3	301.9	350.5	1.216	1.394	326.2	1.306
4	301.3	357.6	1.214	1.422	329.4	1.319
5	299.2	359.4	1.205	1.429	329.3	1.318
6	303.2	358.2	1.222	1.424	330.7	1.324
7	302.7	360.2	1.220	1.432	331.4	1.327
8	301.9	362.2	1.216	1.440	332.0	1.329
9	299.4	362.1	1.206	1.440	330.7	1.324
10	302.5	360.2	1.219	1.432	331.3	1.326

After quench 11, the specimen fell into the bottom of water bath then the crack length of y-direction grew to edge of specimen.

Table D-14. The crack length after cyclic thermal shock test which maximum cycling number is 20 (specimen B1-5 $\Delta T = 290\ ^{\circ}C$).

# of Quench	x-direction A(μm)	y-direction B(μm)	A/234.1 ($c_{0,x}$)	A/221.1 ($c_{0,y}$)	(A+B)/2 M(μm)	C/227.6 ($c_{0.M}$)
0	234.1	221.1	1	1	227.6	1
1	408.3	345.9	1.744	1.564	377.1	1.656
2	431.2	386.4	1.841	1.747	408.8	1.796
3	455.4	393.7	1.945	1.780	424.5	1.865
4	482.2	400.4	2.059	1.810	441.3	1.938
5	481.0	402.6	2.054	1.820	441.8	1.941
6	483.4	402.2	2.064	1.819	442.8	1.945
7	482.6	401.3	2.061	1.815	441.9	1.941
8	482.0	403.5	2.058	1.824	442.7	1.945
9	482.5	404.5	2.061	1.829	443.5	1.948
10	481.8	402.0	2.058	1.818	441.9	1.941
11	483.5	403.0	2.065	1.822	443.2	1.947
12	482.6	402.2	2.061	1.819	442.4	1.943
13	484.8	404.2	2.070	1.828	444.5	1.952
14	483.1	404.5	2.063	1.829	443.8	1.949
15	482.5	401.5	2.061	1.815	442.0	1.942
16	482.7	404.7	2.061	1.830	443.7	1.949
17	482.5	403.4	2.061	1.824	442.9	1.946
18	481.9	404.0	2.058	1.827	442.9	1.946
19	483.3	403.7	2.064	1.825	443.5	1.948
20	481.3	403.5	2.055	1.824	442.4	1.943

Table D-15. The crack length after cyclic thermal shock test which maximum cycling number is 20 (specimen A5-10 $\Delta T = 295\ ^{\circ}C$).

# of Quench	x-direction A(μm)	y-direction B(μm)	A/232.6 ($c_{0,x}$)	A/229.1 ($c_{0,y}$)	(A+B)/2 M(μm)	C/230.8 ($c_{0,M}$)
0	232.6	229.1	1	1	230.8	1
1	319.5	317.9	1.373	1.387	318.7	1.380
2	364.9	342.0	1.568	1.492	353.4	1.531
3	400.7	344.4	1.722	1.503	372.5	1.613
4	423.6	389.9	1.821	1.701	406.7	1.762
5	435.6	401.7	1.872	1.753	418.6	1.813
6	433.7	403.0	1.864	1.759	418.3	1.812
7	433.2	403.8	1.862	1.762	418.5	1.812
8	433.5	403.7	1.863	1.762	418.6	1.813
9	433.7	402.8	1.864	1.758	418.2	1.811
10	433.2	403.5	1.862	1.761	418.3	1.812
11	433.3	403.3	1.862	1.760	418.3	1.812
12	433.7	403.2	1.864	1.759	418.4	1.812
13	433.0	403.2	1.861	1.759	418.1	1.811
14	433.6	403.4	1.864	1.760	418.5	1.812
15	430.0	402.6	1.848	1.757	416.3	1.803
16	433.5	403.5	1.863	1.761	418.5	1.812
17	432.7	403.7	1.860	1.762	418.2	1.811
18	433.8	402.8	1.865	1.758	418.3	1.812
19	433.2	403.2	1.862	1.759	418.2	1.811
20	433.6	403.3	1.864	1.760	418.4	1.812

Table D-16. The crack length after cyclic thermal shock test which maximum cycling number is 20 (specimen A5-14 $\Delta T = 300\ ^{\circ}C$).

# of Quench	x-direction A(μm)	y-direction B(μm)	A/241 ($c_{0,x}$)	A/247.3 ($c_{0,y}$)	(A+B)/2 M(μm)	C/244.1 ($c_{0.M}$)
0	241.0	247.3	1	1	244.1	1
1	489.9	332.6	2.032	1.344	411.2	1.684
2	533.0	359.7	2.211	1.454	446.3	1.828
3	556.7	371.0	2.309	1.500	463.8	1.900
4	560.9	376.5	2.327	1.522	468.7	1.920
5	580.6	382.6	2.409	1.547	481.6	1.972
6	590.3	380.6	2.449	1.539	485.4	1.988
7	588.6	382.5	2.442	1.546	485.5	1.989
8	590.6	381.7	2.450	1.543	486.1	1.991
9	590.2	382.9	2.448	1.548	486.5	1.993
10	592.0	481.7	2.456	1.947	536.8	2.199
11	592.8	479.5	2.459	1.938	536.1	2.196
12	592.7	479.2	2.459	1.937	535.9	2.195
13	592.3	480.8	2.457	1.944	536.5	2.198
14	593.1	482.0	2.461	1.949	537.5	2.202
15	593.1	482.8	2.461	1.952	537.9	2.203
16	591.6	481.5	2.454	1.947	536.5	2.198
17	592.4	481.4	2.458	1.946	536.9	2.199
18	593.7	481.9	2.463	1.948	537.8	2.203
19	592.6	482.0	2.458	1.949	537.3	2.201
20	593.2	483.6	2.461	1.955	538.4	2.205

Table D-17. The crack length after cyclic thermal shock test which maximum cycling number is 20 (specimen A6-1 $\Delta T = 305\ ^{\circ}C$).

# of Quench	x-direction A(μm)	y-direction B(μm)	A/238.4 ($c_{0,x}$)	A/236.3 ($c_{0,y}$)	(A+B)/2 M(μm)	C/237.3 ($c_{0.M}$)
0	238.4	236.3	1	1	237.3	1
1	490.4	375.6	2.057	1.589	433.0	1.824
2	497.5	424.9	2.086	1.798	461.2	1.943
3	524.9	446.8	2.201	1.890	485.8	2.046
4	554.5	481.5	2.325	2.037	518.0	2.182
5	556.6	485.7	2.334	2.055	521.1	2.195
6	558.2	492.2	2.341	2.082	525.2	2.212
7	581.3	503.3	2.438	2.129	542.3	2.284
8	580.1	508.0	2.433	2.149	544.0	2.292
9	584.5	514.2	2.451	2.176	549.3	2.314
10	580.8	512.4	2.436	2.168	546.6	2.302
11	579.8	509.8	2.432	2.157	544.8	2.295
12	579.4	512.8	2.430	2.170	546.1	2.300
13	582.4	509.3	2.442	2.155	545.8	2.299
14	582.7	511.8	2.444	2.165	547.2	2.305
15	580.2	511.7	2.433	2.165	545.9	2.300
16	582.4	509.4	2.442	2.155	545.9	2.299
17	583.6	511.3	2.447	2.163	547.4	2.306
18	581.2	511.5	2.437	2.164	546.3	2.301
19	583.6	511.4	2.447	2.164	547.5	2.306
20	582.2	511.3	2.442	2.163	546.7	2.303

The following tables give the thermal fatigue behavior for an unreinforced alumina rectangular bar shaped specimen (9.1 mm × 56.3 mm × 0.96 mm). The crack lengths were measured using an optical microscope through cyclic thermal testing. The relative Vickers indentation cracks are indicated by L1, L2, and L3 (see section 2.7). The crack lengths were measured by L1, L2, L3 order after taking the specimen out of the water.

Table D-18. The crack length of bar-shape specimen under the thermal shock, L1.

number of quench	x-dir. crack length, L1x (μm)	y-dir. crack length, L1y (μm)	L1y / L1x
0	218	232.8	1.07
1	225.3	257.4	1.14
2	236.4	270.7	1.15
3	239.5	276.5	1.15
4	240.2	277.8	1.16
5	240.1	277.6	1.17
6	244.5	278.5	1.14
7	243.6	277.4	1.14

Table D-19. The crack length of bar-shape specimen under the thermal shock, L2.

number of quench	x-dir. crack length, L2x (μm)	y-dir. crack length, L2y (μm)	L2y / L2x
0	234.3	242.7	1.03
1	253.8	298.3	1.18
2	261.3	299.2	1.15
3	261.1	342.2	1.31
4	261.9	343.6	1.31
5	261.8	344.4	1.32
6	259.8	344.3	1.33
7	259.2	343.9	1.33

Table D-20. The crack length of bar-shape specimen under the thermal shock, L3.

number of quench	x-dir. crack length, L3x (μm)	y-dir. crack length, L3y (μm)	L3y / L3x
0	220.1	252.8	1.15
1	238.5	272.7	1.14
2	248	280.4	1.13
3	246.3	288.5	1.17
4	247.5	289.9	1.17
5	246	288.2	1.17
6	246.9	289.6	1.17
7	245.3	288.5	1.18

6. References

1. W.P. Roger and A.F. Emerry, "Contact Thermal Shock Test Ceramics," J. of Mat. Sci. 27, 146-152 (1992).

2. E.H. Lutz and M.V. Swain, "Interaction between Flaw Resistance, R-curve behavior, and Thermal Shock degradation in Ceramics," J. Am. Ceram. Soc. 74 [11] 2859- 68 (1991).

3. K. T. Faber, M.D. Huang, and .A.G. Evans, "Quantitative of Thermal Shock in Ceramics on a Novel Test Technique," J. Amer. Ceram. Soc. 64, 296-301 (1981).

4. T.K. Gupta, "Crack Healing in Thermally shocked MgO," J. Am. Ceram. Soc. 58 [43] (1975).

5. F.F. Lange and T.K. Gupta, "Crack Healing by Heat Treatment," J. Am. Ceram. Soc. Discussion and Notes, 53, 54-55 (1976).

6. T.K. Gupta, "Crack Healing and Strengthening of Thermally Shocked Alumina," J. Am. Ceram. Soc., 259-61(1976).

7. D.P.H. Hasslemann, "Unified Theory of Thermal Shock Fracture Initiation and Crack Propagation in Brittle Ceramics," J. Am. Ceram. Soc., 52, 600-04 (1969).

8. H. Ohira and R.C. Bradt, "Strength Distribution of a Quench-strengthen Aluminasilicate," J. Am. Ceram. Soc., 71 [1], 35-41 (1988).

9. R.C. Bradt, M. Asnizuka, T.E. Easler and H. Ohira, "Statistical Aspects of the Thermal Shock Damage and the Quench Strengthening of Ceramics," Thermal Shock and Thermal Fatigue Behavior of Advanced Ceramics, G. A. Schneider and G. Petzow 447-58, Kluwer Academic Publishers, the Nederlands (1993).

10. W.J. Lee and E.D. Case, "Comparison of Saturation Behavior of Thermal Shock Damage in Variety of Brittle Materials," Mat. Sci. and Eng., A154 1-9 (1992).

11. E.D. Case, Y. Kim, W.J. Lee, "Thermal Shock and Thermal Fatigue Behavior of Advanced Ceramics," Thermal Shock and Thermal Fatigue Behavior of Advanced Ceramics, G. A. Schneider and G. Petzow 393-406, Kluwer Academic Publishers, the Nederlands (1993).

12. W.J. Lee and E.D. Case, "Thermal Fatigue in Polycrystalline Alumina," J. of Mat. Sci., 25, 5053-5054 (1990).

13. Y. Kim, "Cyclic Thermal Shock in Ceramics and Ceramic Composites," Ph D. Dissertation, Michigan State Univ., MI (1991).

14. E.H. Lutz, M.V. Swain, and N. Claussen, "Thermal Shock Behavior of Duplex Ceramics," J. Am. Ceram. Soc. 74[1], 19-24 (1991).

15. J.R. Brockenbrough, L.E. Forsythe and R.L. Rolf, "Reliability of Brittle Materials in Thermal Shock," J. Am. Ceram. Soc., 64, 634-37(1986).

16. J.C. Coppla and R.C. Bradt, "Thermal Shock Damage in SiC," J. Am. Ceram. Soc., 56, 214-218 (1973).

17. W.D. Kingery, H.K.Bowen, and D.R. Uhlmann, "Introduction to Ceramics," 2nd ed. 816-830, John Wiley and Sons, Inc., New York (1976).

18. W.D. Kingery, "Factors Affecting Thermal Stress Resistance of Ceramics Materials," J. Am. Ceram. Soc., 38, 3-15 (1955).

19. J.B. Walsh, "Effect of Cracks in the Compressibility of Rock," J. Geophy. Res., 70 [2], 381-389 (1965).

20. R.A. Sack, "Extension of Griffith's Theory of Rupture to Three Dimensions," Proc. Phys. Sci. 58 a, 729-36 (1946).

21. T. K. Gupta, "Strength degradation and crack propagation in thermally shocked Al_2O_3," J. Am. Ceram. Soc. 55 [5], 249-253(1972).

22. W. P. Rogers, A. F. Emery, R. C. Bradt, and A. L. Kobayashi, "Statistical Study of Fracture of Ceramic materials in the Water Quench Test," J. Am. Ceram. Soc 70[6], 406-12 (1987).

23. M. Ashizuka, T. E. Easler, and R. C. Bradt, "Statistical Study of Thermal shock damage of Borosilicate Glass," J. Am. Ceram. Soc. 66 [8], 542-550 (1983).

24. S. Schon, H. Prielipp, R Janssen, J. Rodel, and N. Claussen, "Effect of Microstructual Scale on Thermal Shock Resistance of Aluminum-Reinforced Alumina," J. Am. Ceram. Soc. 77 [3], 701-704 (1994).

25. J. H. Ainsworth and R. E. Moore, "Fracture Behavior of Thermally Shocked Aluminum Oxide," J. Am. Ceram. Soc. 52 [11], 628-29 (1969).

26. L.T. Herkkovich and M.V. Hyer, "Damage -induced Property Changes in Composite Subjected to Cyclic Loading," Eng. Fract. Mech. 25, 779-791 (1986).

27. J. H. Ainsworth and R. H. Herron, "Thermal Shock Damage Resistance of Refractories," J. Am. Ceram. Soc. Bulletin 53 [7] 628-29 (1974).

28. C. E. Semler and T.H. Hawisher, "Evaluation of the Thermal Shock Resistance of Refractories Using the Ribbon Test Method," J. Am. Ceram. Soc. Bulletin 59 [7], 732-38 (1980).

29. Y. Kim, W. J. Lee, and E. D. Case, "Thermal Fatigue Behavior of Ceramic Matrix composite: A Comparison among Fiber Reinforced Whisker Reinforced, Particulate Reinforced, and Monolithic Ceramics", in Proceedings of the American Society for Composites, 5th Technical Conference, Technomic Publications, Lancaster 871-881 (1990).

30. W. J. Lee, "Thermal Fatigue in Ceramics and Ceramic Matrix Composites", Ph.D. Dissertation, Michigan State University, East Lansing, MI (1991).

31. K. Lee, Personal Communication NSC 820 Class Notes, 1995, Graduate Student, Materials Science and Mechanics, Michigan State University.

32. C. E. Ash, "Cyclic Thermal Shock-Crack Growth in Alumina," Senior Research Project, Michigan State University. (1994).

33. Y. Kagawa, "Quantitative Analysis of Closure Stress-Crack Separation Curve in Grain Bridge Toughening of Polycrystalline Ceramics, Mat. Sci. and Eng., A176 379-383 (1994).

34. S. Lathabai, J. Rodel, and B. R. Lawn, "Cyclic Fatigue from Degradation at Bridging Grains in Alumina," J. Am. Ceram. Soc., 74 [6] 1340-48 (1991).

35. J. C. Hay and K. W. White, "Grain-Bridging Mechanism in Monolithic Alumina and Spinel," J. Am. Ceram. Soc., 76 [7], 1849 -54 (1993).

36. P. L. Swanson, C. J. Fairbanks, B. R. Lawn, Y. W. Mai, and B. J. Hockey, "Crack Interface Grain Boundary in Ceramics: I, Experimental Study on Alumina," J. Am. Ceram. Soc., 70 [4], 279-89 (1987).

37. H. Kishmoto, A. Ueno, and S. Okawara, "Crack Behavior of Polycrystalline Alumina under Static and Cyclic Load," J. Am. Ceram. Soc., 77 [5] 1324-28 (1994).

38. R. H. Dauskardt, "Cyclic Fatigue-Crack Growth in Grain Growth in Grain bridging Ceramics," J. of Eng. Mat. and Tech. 115, 244-251 (1993).

39. R. H. Dauskardt, "A Frictional-Wear Mechanism for Crack Fatigue-Crack growth in Grain bridging Ceramics," Acta Metall. Mater. 41, 2765-2781 (1993).

40. Y. W. Mai and B. R. Lawn, "Crack Interface Grain Boundary as a Fracture Resistance Mechanism in Ceramics: II, Theoretical Fracture Mechanics," J. Am. Ceram. Soc., 70 [4], 289-94 (1987).

41. Y. S. Chou and D. J. Green, "Silicon Carbide platelet/Alumina Composite: III, Toughening Mechanism," J. Am. Ceram. Soc., 76 [8], 1985-92 (1993).

42. B. R. Lawn, "Microstructure, R-curve, and Strength of Monophase Ceramics," Ceram. Eng. Sci. Proc. 11, 591-593 (1990).

43. R. W. Steinbrech, A. Reichl, and W. Achaarwachter, "R-curve Behavior of Long Cracks in Alumina," J Am. Ceram. Soc., 73 [7], 2009-15 (1990).

44. G. Vekinnis, M. F. Ashby, and P. W. R. Beaumont, "R-curve Behavior of Al_2O_3 Ceramics," Acta Metall. Mater. 38 [6], 1151-1162 (1990).

45. L. M. Braun, S. J. Bennison, and B. R. Lawn, "Short Crack T-curves and Damage Tolerance in Alumina-Based Composites," Ceram. Eng. Sci. Proc., 13, 156-163 (1992).

46. J. Rodel, J. F. Kelly, and B. R. Lawn, "In Situ Measurements of Bridged Crack Interaction in the Scanning Electron Microscope," J. Am. Ceram. Soc., 73 [11] 3313-18 (1990).

47. A. Reichl and R. W. Steinbrech, "Determination of Crack-Bridging Forced in Alumina," J. Am. Ceram. Soc., 71 [6] C299-01 (1988).

48. R. H. Dauskrdt, D. B. Marshall, and R. O. Rktchie, "Cyclic Fatigue Crack Propagation in Magnesia-Partially-Sterilized Zirconia Ceramics," J. Am. Ceram. Soc., 73 [4] 893-93 (1990).

49. Personal Communication MSM 960 Class Notes, 1994, Materials Science and Mechanics, Michigan State University.